Modeling of Sheet Metal Fracture via Cohesive Zone Model and Application to Spot Welds

by

Joseph Z. Wu

A dissertation submitted in partial fulfillment
of the requirements for the degree of
Doctor of Philosophy
(Mechanical Engineering)
in The University of Michigan
2008

Doctoral Committee:

Professor Karl Grosh, Chair
Professor Emeritus William F. Hosford Jr.
Professor Shixin Jack Hu
Professor Anthony M. Waas
Majeed H. Bhatti, General Motors Corporation

Acknowledgements

It has been a long and challenging journey for the past seven plus years. Pursuing a Ph.D degree is my dream. However, doing it on a part-time base is neither something I had planned nor something I envy at all. I am just relieved this has come to an end.

This research is first made possible through Salary Tuition Assistance Program from General Motors Corporation. I am hoping that the results from the research are as rewarding to me personally as to General Motors Corporation.

I would like to thank Dr. Majeed Bhatti, senior manager and Global Crash Safety Focus group chairperson from General Motors Corporation, for his willingness to serve on the dissertation committee. I have learned a great deal from him on a daily base as a professional and a researcher.

Thanks are also due to Professor Jack Hu for his time and advice on various subjects during various stages of this research.

Thank you Professor William Hosford. You have taught me hand-by-hand how to write a short and good thesis.

I am truly grateful to the assistance from Steven Emanuel, the research laboratory specialist at Auto Lab, in preparing all the test specimens. Steve, it is not enough to say a million thanks. In addition, all the pain and frustration are often washed away by your lengthy yet humorous speech. I certainly hope that you will remember me as a good listener.

The guidance on the research project from Professor Michael Thouless is instrumental and greatly acknowledged. Without a doubt, I have been benefiting from your knowledge, your brilliant thought process, and your willingness to accommodate my part time at school.

Professor Anthony Waas has been a critical voice in the latter stage of the project and also offered numerous suggestions to improve the dissertation. I am truly thankful that he spent the time going through the writing.

Professor Karl Grosh took over the chairmanship of the committee under extraordinary circumstances and provided the leadership to move forward the whole process. Your expertise in the area of finite element method has certainly put the dissertation on a solid foundation.

Finally I would like to thank my family for their support. My son, James, thank you for praying daily and promising to kick my butt if I do not finish on time. My daughter, Janet, at her three months old, accompanied me from time to time while I was conducting the experiment, which satisfied the lab requirement of not running tests alone. My wife, Ms. Wanshi Wu, has made enormous sacrifice. I am indebted to you for a life time.

Table of Contents

List of Figures

Abstract

Even though the cohesive zone model (CZM) has been widely used to analyze ductile fracture, it is not yet clearly understood how to calibrate the cohesive parameters including the specific work of separation (the work of separation per unit crack area) and the peak stress. A systematic approach is presented to first determine the cohesive values for sheet metal and then apply the calibrated model to various structure problems including the failure of spot welds. Al5754-O was chosen for this study since it is not sensitive to heat treatment so the effect of heat-affected-zone (HAZ) can be ignored. The CZM has been applied to successfully model both mode-I and mode-III fracture for various geometries including Kahn specimens, single-notch specimens, and deep double-notch specimens for mode-I and trouser specimens for mode-III. The mode-I fracture of coach-peel spot-weld nugget and the mixed-mode fracture of nugget pull-out have also been well simulated by the CZM. Using the mode-I average specific work of separation of 13 kJ/m^2 identified in a previous work and the mode-III specific work of separation of 38 kJ/m^2 found in this thesis, the cohesive peak stress has been determined to range from 285 MPa to 600 MPa for mode-I and from 165 MPa to 280 MPa for mode-III, depending on the degree of plastic deformation. The uncertainty of these cohesive values has also been examined. It is concluded that, if the specific work of separation is a material constant, the peak stress changes with the degree of plastic deformation and is therefore geometry-dependent.

Chapter 1

Introduction

General Background

Structural integrity is closely related to automotive safety. For example, in an end-to-end crash, the fuel system integrity is crucial. Full vehicle finite element (FE) models with well over one million elements and ten million degree of freedoms have been used to help vehicle design. However these models do not reasonably simulate crack initiation and growth under impact loading.

Strength of joints including spot welds affects the structural integrity. There are typically more than 4000 spot welds in a vehicle structure. Spot-weld failure is often seen in numbers in a vehicle crash test. Extensive tests are usually conducted to obtain experimental data for design. The welding process parameters, the sheet thickness, and the weld nugget size are all to be included in a test matrix for a given material. A unified failure criterion is not yet well established.

Due to these limitations, it is very difficult to predict metal tearing and weld failure prior to vehicle crash tests. It is well known that it costs millions of dollars to build the prototype vehicles during vehicle development process. Lack of better knowledge of how the vehicles will perform in crash tests often leads to additional iterations of designing, building and testing. FE models are viewed as a viable tool to reduce the cost and to shorten the development cycle. Therefore, this research intends to explore methods to better understand and simulate fracture of sheet metal and apply them to predict the spot-weld failure under quasi-static and dynamic loading in automotive design.

Cohesive Zone Model and Applications

Griffith first proposed a physical mechanism of fracture resistance involving surface energy [1]. A quantity controlling the behavior of the crack, *G*, defined as the energy release rate, is given

$$G = -\frac{1}{t}\frac{d\pi}{da} \tag{1}$$

where $d\pi$ is an amount of decreasing potential energy when extending a small amount of crack length *da* with a thickness of *t*. Thus, G characterizes the energy per unit crack area required to extend the crack and it was thought that all of the potential energy released is used in the creation of the new free surface on the crack faces. This is the basic theory of linear-elastic fracture mechanics (LEFM) and it is true when there is no plastic deformation. For metals, however, it was recognized that the plastic dissipation accompanying fracture makes a significant contribution to fracture resistance. If the plastic zone around the crack tip is small, it was shown that LEFM is still applicable [2].

Rice [3] later proposed an equivalent path independent integral, J, to account for work per unit area when crack initiates and propagates,

$$J = \int_{\Gamma}\left(Wdy - \mathbf{T}\cdot\frac{\partial \mathbf{u}}{\partial x}ds\right), \qquad W = \int_0^{\varepsilon}\sigma_{ij}d\varepsilon_{ij} \tag{2}$$

where Γ is a path surrounding the notch tip (Figure 1.1), from the lower crack surface to the upper crack surface, *W* is the strain-energy density. **T** is the traction vector defined according to the outward normal **n** along Γ, $T_i = \sigma_{ij}\, n_j$, **u** is the displacement vector, and *ds* is an element of arc length along Γ. It was demonstrated that the J-integral is not limited to LEFM and may be extended to two-dimensional small-scale yielding deformation field for elastic-plastic material.

Like J-integral, which does not rely on the underlying micro-mechanics of fracture, crack tip opening angle or crack tip opening displacement (CTOA/CTOD) involves macroscopic quantitative measurements. Among the micro-mechanically based fracture models, the dilatant Gurson plasticity model is based on ductile rupture by void

nucleation and growth [4]. Another approach is the concept of cohesive zone model (CZM), which was first proposed by Barrenblatt [5] and Dugdale [6] as an alternative to analyze fracture process. A broad survey of the literature and more in-depth discussion of the aforementioned fracture models are presented in the introduction of Chapter 2.

The CZM has been widely used in a number of materials including polymers [7], metallic materials [8], ceramic materials [9], bi-material systems [10], and composites [11-12]. Two basic CZM formulations have been proposed. One formulation was widely explored by Needleman to study interfacial de-cohesion [13-14]. The mechanical response of the interface is characterized in terms of both an interfacial strength σ_{max} and a work of separation per unit area W. Therefore, a characteristic length δ is introduced. The relation between normal traction, T_n (force per unit area), and normal separation along the interface, u_n, is specified to have an exponential form,

$$T_n = \frac{27}{4}\sigma_{\max}\left(\frac{u_n}{\delta}\right)\left[1-2\left(\frac{u_n}{\delta}\right)+\left(\frac{u_n}{\delta}\right)^2\right] \tag{3}$$

which emulates atomistic bonding (Figure 1.2).

The other is an idealized trapezoidal traction-separation law by Tvergaard and Hutchinson [15-17], which was prescribed on a crack plane ahead of crack tip, and used for a systematic study of crack growth resistance in elastic-plastic solids (Figure 1.3). A critical crack opening displacement δ_c was introduced as a characteristic length. The complete list of parameters characterizing the fracture process and the deformation of the solids are:

Fracture process	Γ_0, $\hat{\sigma}$, δ_1/δ_c, δ_2/δ_c
Deformation of solids	σ_y, n, E and ν

where Γ_0 is the specific work of separation (defined as the work of separation per unit crack area), $\hat{\sigma}$ is the peak stress or the maximum true stress at separation, δ_1 and δ_2 define the shape of the trapezoidal traction-separation law illustrated in Figure 1.3. Material properties of the solids include Young's modulus E, Poisson's ratio ν, the yield strength σ_y, and the strain hardening component n. It is worth noting that both

formulations have appeared earlier in the study of the effect of strain-softening cohesive material on crack stability by Ungsuwarungsri [18]. In this work the trapezoidal traction-separation law is used because of its simplicity featured by two control parameters: the specific work of separation and the peak stress. The Chapter 2 introduction reviews the variability of the CZM parameters as well as the different procedures that have been proposed to determine the values of the two control parameters.

The CZM has also been used in modeling dynamic crack growth in solid materials. In some research, the CZM has been assumed rate-independent and the surrounding continuum material considered rate-dependent to simulate dynamic crack growth [19-20]. In others, the rate-dependency has been included in the CZM [21-23].

There exists some ambiguity about the exact definition of fracture toughness. To account for the plastic deformation in a sheet metal fracture, fracture toughness Γ in this work is defined as the energy dissipated per unit crack area,

$$\Gamma = \frac{1}{t}\frac{dE}{da} = \Gamma_0 + \Gamma_p \tag{4}$$

where dE is the amount of energy dissipated extending a small amount of crack length da with a thickness of t. The fracture toughness Γ consists of two components: the specific work of separation Γ_0, which is identified with the actual work of fracture per unit crack area and therefore assumed a material constant; the plastic energy per unit area Γ_p, which is dependent on the state of plastic deformation. It has been observed that the fracture toughness increases with the increase of thickness at plane-stress state for high-strength maraging steel [24] and Al6082-O thin plates [25]. This linear relationship has also been confirmed analytically [26-27]. More detailed discussion is presented in Chapter 3.

Spot Weld Modeling

Most math models of spot welds are considered empirical, whether force based or stress based. One example of a force based failure criterion is [28]:

$$\left(\frac{f_s}{F_s}\right)^{\alpha}+\left(\frac{m_b}{M_b}\right)^{\gamma}+\left(\frac{f_n}{F_n}\right)^{\mu}+\left(\frac{m_t}{M_t}\right)^{\beta}=1 \tag{5}$$

where s, b, n, and t represent the four independent failure modes: tensile shear, peel bending, normal pull, and in-plane torsion, respectively. The denominators F_s, M_b, F_n, and M_t represent the failure strengths of the four independent failure modes, respectively, and the numerators f_s, m_b, f_n, and m_t are the corresponding applied loads. The symbols α, β, μ, and γ are adjustable exponents that define the failure surface between the independent modes. Further, Lin, *et al.* [29-30] investigated the physical failure mechanism of spot welds and developed a force-based failure criterion to characterize the dynamic failure loads. In addition, one example of a stress based failure criterion is given as [31]:

$$\left(\frac{S_s}{S_{su}}\right)^{n}+\left(\frac{S_t}{S_{tu}}\right)^{m}=1 \tag{6}$$

where S_s and S_t are the applied shear and tensile stresses, respectively. S_{su} and S_{tu} are the shear and the tensile ultimate strengths, respectively. The shape fitting exponents n and m are determined through experiments.

Zuniga and Sheppard [32] performed failure tests of spot weld on high strength steel and found that the failure mechanism for lap-shear sample is localized necking in the base metal and near the boundary of heat affected zone (HAZ) and the base metal. The plastic strain near the necking zone was then used as the failure criterion to interpret the strength of spot weld. Recently stress formulas for a multi-axial spot weld specimen were proposed to convert global forces into the notch stress, the stress away from the notch, and the stress intensity factor at the spot weld [33]. The formulas are linear solutions and bound to elastic and small deformation.

An emerging method applies the CZM to study the ductile failure of adhesive joints and spot welds [34-38]. The new approach involves two parameter failure criteria: one strength parameter and one energy parameter. In earlier works, only one single failure parameter (the plastic strain, the peak stress or the peak force) was adopted. The latest

application of CZM is to predict the entire load-deformation relationship of Al5754-O spot-welded joints, beyond the onset of initial yield and all the way to final failure [38].

Research Objective

Even though the CZM has been widely used in ductile fracture, it is not yet clearly understood how to calibrate CZM properties through fracture tests. The author wishes to develop a systematic approach to identify CZM parameters for a given sheet metal and apply them to various structure problems including spot welds. Al5754-O is chosen because it is not sensitive to heat treatment so the effect of the HAZ can be ignored. Mode-I and mode-III fracture (Figure 1.4) will be considered in this study since they are more often seen in a vehicle crash test. The intended work involves:

Conducting tensile tests to get material properties including the stress-strain curve;

Conducting common fracture tests to identify CZM parameters under static loading for mode-I and mode-III fracture respectively;

Conducting fracture analysis on other materials to study the applicability of the methods developed through Al5754-O;

Applying identified CZM parameters to simulate the strength of spot welds of Al5754-O under static loading.

It is demonstrated in this work that, if the specific work of separation is a material constant, the peak stress changes with the degree of plastic deformation and is therefore geometry-dependent.

The dissertation is organized as follows. In chapter 2, a thorough discussion of the state-of-the-art fracture models including the CZM is presented. After the material properties

for Al5754-O are obtained through experiments, the CZM is applied to model mode-I fracture of Al5754-O using various geometries and the focus is on whether the cohesive properties are geometry-independent. Chapter 3 continues the mode-I study with the emphasis on the thickness effect. Both Al5754-O and Al6082-O thin plates are used. Mode-I fracture of Al5754-O spot-weld nugget is also simulated by applying the calibrated CZM parameters. Chapter 4 applies the CZM to model mode-III fracture of Al5754-O sheet and to simulate mix-mode fracture of Al5754-O spot-weld nugget pull-out. Finally, the findings are summarized and future work is discussed in chapter 5.

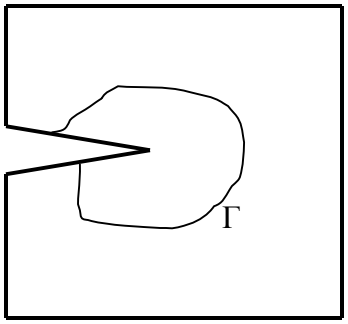

Figure 1.1 The J-integral path Γ surrounding the notch tip.

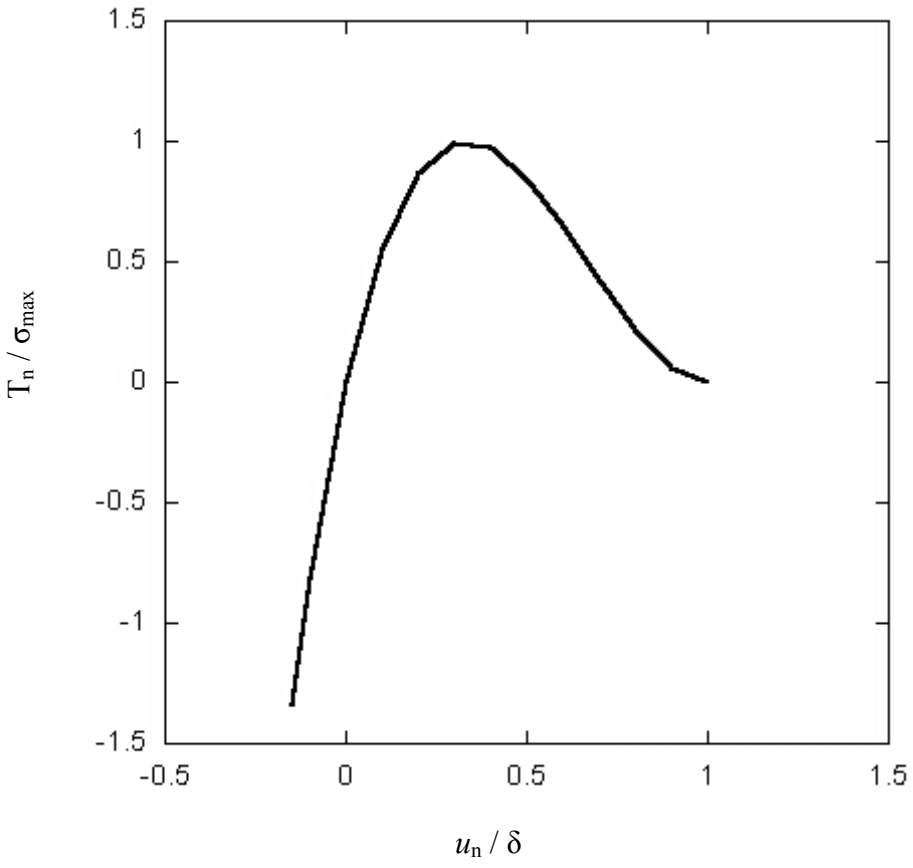

Figure 1.2 Mode-I normal traction as a function of normal opening of cohesive zone.

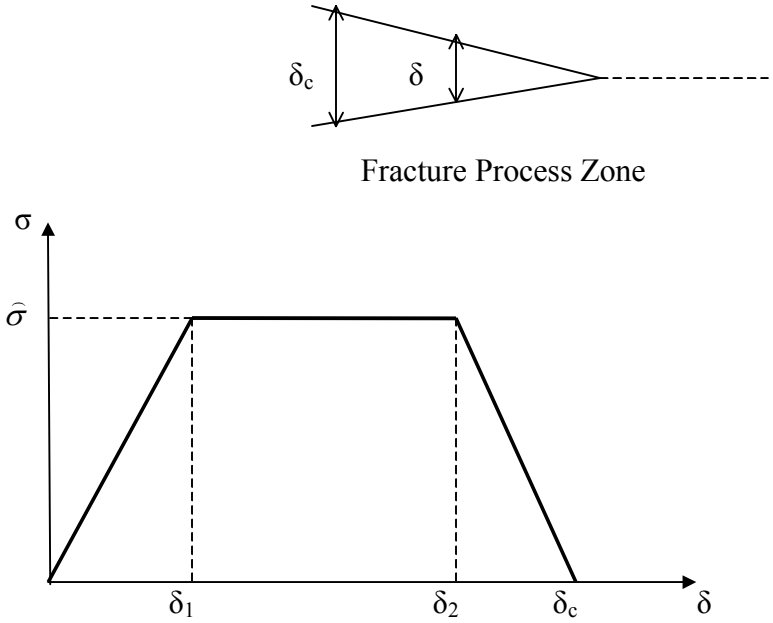

Figure 1.3 Traction-separation law for fracture process.
The peak stress $\hat{\sigma}$ is also the maximum true stress at separation.
The specific work of separation, Γ_0, is the area under the curve.
The plastic deformation in the neighboring area is captured
by the plastic energy per unit area Γ_p.

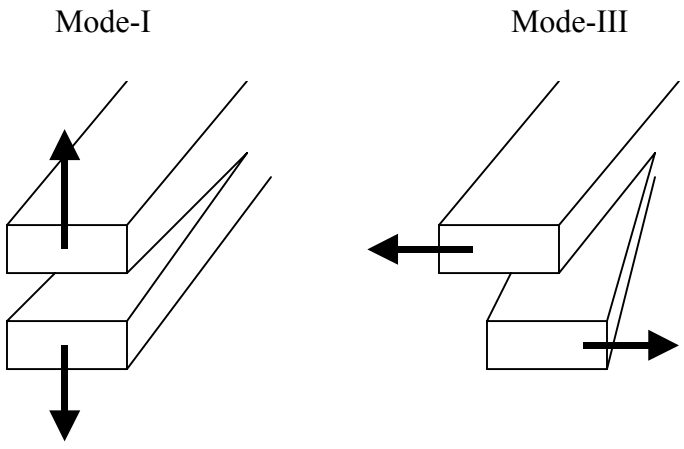

Figure 1.4 Illustrations of mode-I and mode-III fracture

References

1. A. A. Griffith, "The phenomenon of rupture and flow in solids", *Phil. Trans. R. Soc.*, **221**, 163-198 (1920).

2. G. R. Irwin, p. 557-591 in *Fracture mechanics. Structural Mechanics*, Pergamon, Elmsford, NY (1960).

3. J. R. Rice, "A Path Independent Integral and the Approximate Analysis of Strain Concentration by Notches and Cracks", *Journal of Applied Mechanics*, *Transactions of the ASME*, 379-386 (June 1968).

4. A. L. Gurson, "Continuum theory of ductile rupture by void nucleation and growth, Part I—Yield criteria and flow rules for porous ductile media", *Journal of Engineering Material Technology*, **99**, 2–15 (1977).

5. G. I. Barenblatt, "Equilibrium cracks formed during brittle fracture", *Journal of Applied Mathematics and Mechanics*, **23**, 1273-1282 (1959).

6. D. S. Dugdale, "Yielding of steel sheets containing slits", *Journal of the Mechanics and Physics of Solids*, **8**, 100–104 (1960).

7. P. Rahulkumar, A. Jagota, S. J. Bennison, and S. Saigal, "Cohesive element modeling of viscoelastic fracture: application to peel testing of polymers", *International Journal of Solids and Structures*, **37**, 1873–1897 (2000).

8. T. Siegmund and W. Brocks, "A numerical study on the correlation between the work of separation and the dissipation rate in ductile fracture", *Engineering Fracture Mechanics*, **67**, 139–154 (2000).

9. G. T. Camacho and M. Ortiz, "Computational modeling of impact damage in brittle materials", *International Journal of Solids and Structures*, **33**, 2899–2938 (1996).

10. C. G. Aronsson and J. Backlund, "Tensile fracture of laminates with cracks", *Journal of Composite Materials*, **20**, 287–307 (1986).

11. H. D. Espinosa, S. Dwivedi, and H. C. Lu, "Modeling impact induced delamination of woven fiber reinforced composites with contact/cohesive laws", *Computer Methods in Applied Mechanics and Engineering*, **183**, 259–290 (2000).

12. S. J. Song and A. M. Waas, "Energy-based mechanical model for mixed mode failure of laminated composites", *American Institute of Aeronautics and Astronautics Journal*, **33**, 739-745 (1995).

13. A. Needleman, "A Continuum Model for Void Nucleation by Inclusion Debonding", *Journal of Applied Mechanics*, *Transactions of the ASME*, **54**, 525-531 (1987).

14. A. Needleman, "An Analysis of Tensile Decohesion along an Interface", *Journal of the Mechanics and Physics of Solids*, **38**, 289-324 (1990).

15. V. Tvergaard and J. W. Hutchinson, "The relation between crack growth resistance and fracture process parameters in elastic-plastic solids", *Journal of the Mechanics and Physics of Solids*, **40**, 1277-1397 (1992).

16. V. Tvergaard and J. W. Hutchinson, "Effect of T-stress on mode I crack growth resistance in a ductile solid", *International Journal of Solids and Structures*, **31**, 823-833 (1994).

17. V. Tvergaard and J. W. Hutchinson, "Effect of strain-dependent cohesive model on predictions of crack growth resistance", *International Journal of Solids and Structures*, **33**, 3297-3308 (1996).

18. T. Ungsuwarungsri, *The Effect of Strain-Softening Cohesive Material on Crack Stability*, Ph.D Thesis, California Institute of Technology, 1986.

19. X. P. Xu and A. Needleman, "Numerical simulations of fast crack growth in brittle solids", *Journal of Mechanics and Physics of Solids*, **42**, 1397-1434 (1994).

20. T. Siegmund and A. Needleman, "A numerical study of dynamic crack growth in elastic-viscoplastic solids", *International Journal of Solids and Structures*, **34**, 769-787 (1997).

21. F. Costanzo and J. R. Walton, "A study of dynamic crack growth in elastic materials using a cohesive zone model", *International Journal of Engineering Science*, **35**, 1085-1114 (1997).

22. F. Costanzo and J. R. Walton, "Numerical simulation of a dynamically propagating crack with a nonlinear cohesive zone", *International Journal of Fracture*, **91**, 373-389 (1998).

23. D. V. Kubair, P. H. Geubelle, and Y. Y. Huang, "Analysis of a rate-dependent cohesive model for dynamic crack propagation", Engineering Fracture Mechanics, Vol. 70, pp. 685-704, 2003

24. J. M. Barsom S.T. Rolfe, *Fracture and Fatigue Control in Structures: Applications of Fracture Mechanics*, Third Edition, Butterworth-Heinemann, Woburn, MA (1999).

25. T. Pardoen, Y. Marchal, F. Delannay, "Thickness dependence of cracking resistance in thin aluminum plates", *Journal of the Mechanics and Physics of Solids*, **47**, 2093-2123 (1999).

26. B. Cotterell, J. K. Reddel, "The essential work of plane stress ductile fracture", *International Journal of Fracture*, **13**, 267-277 (1977).

27. W. F. Hosford and A. G. Atkins, "On Fracture Toughness in Tearing of Sheet Metal", *Journal of Material Shaping Technology*, **8**, 107-110 (1990).
28. P. Wung, "A Force-based Failure Criterion for Spot Weld Design," *Experimental Mechanics*, **41**, 107-113 (2001).

29. S. H. Lin, J. Pan, S. Wu, T. Tyan, and P. Wung, "Spot Weld Failure Loads under Combined Mode Loading Conditions," SAE 2001-01-0428 (2001).

30. S. H. Lin, J. Pan, T. Tyan, S. Wu, and P. Prasad, "Modeling and Testing of Spot Welds under Dynamic Impact Loading Conditions," SAE 2002-01-0149 (2002).

31. Y. Lee, T. Wehner, M. Lu, T. Morrissett, and E. Pakalnins, "Ultimate Strength of Resistance Spot Welds Subjected to Combined Tension and Shear," *Journal of Testing and Evaluation*, **26**, 213-219 (1998).

32. S. Zuniga and S. D. Sheppard, "Resistance Spot Weld Failure Loads and Modes in Overload Conditions," *Fatigue and Fracture Mechanics: 27th Volume, ASTM STP1296*, R.S. Piascik, J.C. Newman, and N.E. Dowling, Eds., American Society for Testing and Materials, 469-489 (1997).

33. S. Zhang, "Approximate Stress Formulas for a Multiaxial Spot Weld Specimen," Welding Research Supplement, *Welding Journal*, **8**, 201-203 (2001).

34. Q. D. Yang, M. D. Thouless, and S. M. Ward, "Numerical Simulation of Adhesively Bonded Beams Failing with Extensive Plastic Deformation," *Journal of the Mechanics and Physics of Solids*, **47**, 1337-1353 (1999).

35. Q. D. Yang, M. D. Thouless, and S. M. Ward, "Analysis of the Symmetrical 90°–Peel Test with Extensive Plastic Deformation," *Journal of Adhesion*, **72**, 115-132 (2000).

36. Q. D. Yang, M. D. Thouless and S. M. Ward, "Elastic-Plastic Mode-II Fracture of Adhesive Joints," *International Journal of Solids and Structures*, **38**, 3251-3262 (2001).

37. Q. D. Yang and M. D. Thouless, "Mixed-Mode Fracture Analysis of Plastically Deforming Adhesive Joints," *International Journal of Fracture*, **110**, 175-187 (2001).

38. M. N. Cavalli, *Cohesive Zone Modeling of Structural Joint Failure*, Ph.D. Thesis, University of Michigan, 2003.

Chapter 2

Mode-I Fracture of Al5754-O Sheet: Geometrical Effect

Introduction

Sheet metal failure prediction has been under study for vehicle crashworthiness [1]. The prediction of sheet metal fracture limits and forming limits depends on metal properties and process parameters. Cockroft and Latham [2] observed and proposed the criterion of the critical tensile stress in a fracture region,

$$\int_0^{\bar{\varepsilon}_f} \sigma_{max} d\bar{\varepsilon} = C_1 \tag{1}$$

where $\bar{\varepsilon}_f$ is the equivalent strain at which the fracture occurs, σ_{max} is the maximum normal stress, $\bar{\varepsilon}$ is the equivalent strain, and C_1 is a material constant. On the other hand, Clift et al. [3] found that the total plastic work was the successful criterion for the prediction of the fracture site,

$$\int_0^{\bar{\varepsilon}_f} \bar{\sigma} d\bar{\varepsilon} = C_2 \tag{2}$$

where $\bar{\sigma}$ is the equivalent stress and C_2 is a material constant. These criteria have been used in FE models [4-6]. However, these approaches were not intended to model the actual fracture process, but merely to indicate the onset of failure.

This chapter aims to investigate the methods that are currently used to model crack initiation and propagation in sheet metal. The discussion is limited to the ductile fracture that is often preceded by large-scale plastic deformation. There are three phases in ductile fracture: void nucleation, void growth and void coalescence. Voids nucleate from either material impurities such as second-phase particles or from interfacial debonding. Voids

grow while the material undergoes large plastic deformation. Finally neighboring voids interact and coalesce together to form a crack. Ahead of the crack front, more voids nucleate, grow and coalescence [7]. When different methods are compared, the criteria of comparison includes: whether a method is applicable to large-scale yielding, whether the control parameters of the method are independent of geometry, the number of control parameters, and finally whether the method comprehends the physics of crack initiation and growth.

Conventional LEFM methods are not applicable in the presence of large-scale plastic deformation. In applying LEFM to metals, Irwin [8] recognized that the plastic dissipation accompanying fracture makes a significant contribution to the fracture resistance. A path-independent J-integral was first proposed by Rice [9] to account for the work per unit area when a crack initiates and propagates. In Rice's paper, it is demonstrated that the J-integral is not limited to LEFM and may be extended to a 2-D and small-scale yielding deformation field for an elastic-plastic material. When large-scale yielding is present, the J-integral may still be applicable, however, losing its original physical meaning. J-integral has also been applied to a 3-D analysis of a 3-point bend specimen [10]. Research in fracture resistance of thin aluminum sheets has shown that the critical J-integral increases with thickness [11] and the J-integral values do not remain constant with a stable crack growth [12]. Practically, the critical J-integral value has to be obtained for a specific geometry. In addition, the global J-integral does not explicitly characterize local stress and strain fields around the crack tip.

Like J-integral, which does not rely on the underlying micro-mechanics of fracture, crack tip opening angle or crack tip opening displacement (CTOA/CTOD) involves macroscopic quantitative measurements. It is advantageous to use one single control parameter, CTOA or CTOD, to predict fracture. Research has indicated that CTOA and CTOD are well suited for modeling stable crack growth and instability during the fracture process [13-23]. In particular, it has been applied frequently to sheet metal fracture, both computationally and experimentally [13, 15-19, 21-22]. More recently, the CTOA criterion has been implemented into a 3-D FE framework to study the effects of

constraint and crack tunneling [15, 19-22]. Nonetheless, experimental data by a number of researchers have demonstrated that, for a given thickness, the CTOA approximates a constant after an initial drop [13, 16, 18-19, 22]. These results also show a significant scatter for thin metal sheets. In addition, a critical CTOA is dependent on specimen geometry as well as material thickness [15, 23].

Among the micro-mechanically based fracture models, the dilatant plasticity model, first proposed by Gurson [24], is based on ductile rupture by void nucleation and growth. Tvergaard and Needelman [25-26] employed Gurson's model (thus called GTN model) to analyze the cup-cone fracture mode of rounded tensile bars and the ductile rupture of notched bars. Based on Gurson's theorem, a computational cell model for mode-I fracture has been developed to predict the crack growth accompanied by large-scale yielding for steel [27-28]. GTN model has also seen success in predicting the crack growth of sheet metals [13, 29]. Since the model is founded on the material's constitutive relationship, the control parameters of the model apply to all geometries and thicknesses of same material. Nonetheless, a standard method is not yet available to uniquely determine the control parameters for GTN model, and it remains a challenge in engineering practice to identify a relatively large amount of control parameters through a combination of experiments and numerical simulation.

To address ductile fracture in a convenient way within the FE framework, a cohesive zone model (CZM) has been widely used to analyze the fracture process, as an alternative to above methods. The concept of CZM was first proposed by Barrenblatt [30] and Dugdale [31]. Among many, two CZM formulations are mostly applied. One is an exponential form by Needleman [32-33], which emulates atomistic bonding in interfacial de-cohesion. The other is an idealized trapezoidal traction-separation law by Tvergaard and Hutchinson [34-36], which was prescribed on a crack plane ahead of crack tip, and used for a systematic study of crack growth resistance in elastic-plastic solids. In this work, the idealized trapezoidal traction-separation law is chosen to represent the CZM due to its simplicity featured by two control parameters: the specific work of separation and the peak stress (Figure 1.3).

CZM has been used in modeling crack growth of aluminum sheets [37-39]. Different procedures have been proposed to determine the two control parameters for CZM. The specific work of separation is generally identified with the J-integral; however the conclusions about the peak stress are different. Roy and Dodds developed a 3-D interface-cohesive FE model to analyze the ductile crack extension in thin aluminum panels [37]. In their work, the peak stress and the specific work of separation were calibrated on the basis of experimental results from compact-tension specimens. Li and Siegmund [38] applied CZM to predict the crack growth of center-cracked aluminum panel and multi-site damaged specimens, and identified the values of CZM parameters from the results of global measurements and micromechanical damage models, without employing a fitting procedure. What is common in both works is that, the specific work of separation was identified with the values of J-integral at crack initiation and converted from the stress intensity factor (K_{IC}), assuming small-scale yielding, and the cohesive peak stress was concluded to be two times of the tensile yield stress [37-38].

On the other hand, efforts were made to establish a standard procedure to calibrate the cohesive parameters [39]. The specific work of separation equals the value of J-integral at the onset of stable crack extension, determined from fracture mechanics tests. The peak stress for normal fracture was calibrated through the tensile tests conducted on the notched round bars. Following this procedure, the cohesive peak stress was determined to be five times of the tensile yield stress for aluminum 2024-FC of 3 mm thickness, and a 3-D CZM gave good predictions for the Compact-Tension specimen [39].

It is not clear whether the two control parameters of CZM including the cohesive peak stress and the specific work of separation are material properties. Siegmund and Brocks [40] argued in a 2-D plane strain setting that the values of the CZM parameters do not remain constant throughout a crack growth analysis and their change is not known a priori. Further CZM modeling of the micro-ductile crack growth in thick specimens by Chen et al. [41] demonstrated that, if the cohesive zone parameters are kept constant along the thickness, it is not possible to fit the computed crack extension to the experimental results. It needs to be investigated whether CZM is still applicable to ductile

fracture accompanied by large-scale yielding in thin sheet metal, where the deformation field is 3-D in nature [42].

The benefits of applying CZM to ductile fracture are twofold: the concept of CZM underlines the fracture process and it is convenient to implement the CZM with two control parameters into a FE code. Nonetheless, in the presence of large-scale yielding, it is not known whether the cohesive parameters are dependent on specimen geometry. This question will be addressed through a two-step process [43]: calibration and application. This chapter will study mode-I fracture of 2 mm Al5754-O sheet using various geometries. The first part is to determine the material properties of Al5754-O using tensile tests. Fracture tests will be conducted to calibrate the cohesive values used in 3-D FE models. The calibrated CZM will then be used to predict the ductile crack growth in single-notch geometry, in comparison to experimental data. In addition, the CZM will be compared to FE models using plastic strain as the failure criteria. Finally, the limitations of the 3-D CZM will be discussed.

Determination of Mechanical Properties

Young's modulus of 69 GPa and Poisson's ratio of 0.33 were used in this work for Al5754-O because it is the closest to Al5657-O in the 5000 series of aluminum alloy [44]. To obtain additional mechanical properties including the stress-strain curve, five type-I dogbone specimens [45] (Figure 2.1) were prepared from 2 mm thick Al5754-O sheet. The specimens had a gross length of 165 mm, a gross width of 19 mm, a gage length of 50 mm (the initial length for calculating the engineering strain) and a gage section width of 13 mm. The initial area for calculating the engineering stress is therefore 13 x 2 = 26 mm. The specimens were cut along the rolling direction and tested on a screw-driven tensile test machine with a test speed of 5 mm/min. The loads were monitored through a load cell and the displacement measured by an extensometer. Figure 2.2 shows the engineering stress-strain curves. Test results show very good consistency and repeatability, with one test deviating slightly from the rest, likely due to a first-time setup. Two specimens failed at an engineering strain of 20% as they fractured

prematurely outside the gage section. The other three specimens necked inside the gage section at an engineering strain of 22%. The yield strength was determined to have a value of approximately 100 MPa and the tensile strength was 234 MPa. The true stress at the onset of necking was then computed to be 285 MPa assuming incompressibility. The post-yield true stress versus true strain curve can also be formulated as the following:

$$\sigma = 393\varepsilon^{0.2} \text{ MPa} \tag{3}$$

To check whether the material may be considered isotropic, some additional experiments were conducted. First, two more dogbone specimens were cut from the lateral direction, perpendicular to the rolling direction. Subsequent tensile tests generated stress-strain curves similar to what are shown in Figure 2.2. Secondly, the R-value, defined as the ratio of specimen width change to thickness change during a uni-axial tensile test, was applied to measure the degree of homogeneity. Based on experimental measurements, R_0, the R-value along the longitudinal direction, is similar to R_{90}, the R-value along the lateral direction, and both were measured at 0.7. As a result, σ_z, the yield strength along the thickness direction, was computed from σ_x, the yield strength along the longitudinal direction, with the Hosford's equation [46]:

$$\sigma_Z = \sigma_X \left[R_{90}(1+R_0)/(R_0+R_{90})\right]^{\frac{1}{8}} \tag{4}$$

$$\sigma_Z = 100\left[0.7(1+0.7)/(0.7+0.7)\right]^{\frac{1}{8}} = 100(0.98) = 98 \text{ MPa} \tag{5}$$

Therefore isotropy was assumed.

A continuum FE model (Figure 2.1) was developed in ABAQUS to simulate the dogbone experiment. The FE model reproduced the stress-strain relationship prior to final fracture, which validates the material property data used in FE models.

3-D CZM Model

The traction-separation law shown in Figure 1.3 includes a list of parameters to model the fracture process zone: Γ_0, the specific work of separation (i.e., the work of separation per unit area), $\hat{\sigma}$, the peak stress, and δ_1 and δ_2, the shape parameters [34]. A critical crack

opening displacement δ_c is introduced as a characteristic length. The CZM parameters are generally categorized as the primary parameters (or control parameters) including Γ_0 and $\hat{\sigma}$, and the secondary shape parameters including δ_1 and δ_2. Once the shape is fixed, the critical separation δ_c is no longer an independent parameter, but a derivative of the specific work of separation and the peak stress. Nonetheless, there exists a difference of opinions on the importance of shape parameters [47]. In this work, the importance of choosing shape parameters is not studied. Based on previous studies by Yang [48] and Cavalli [49], a 3-D cohesive-zone element (Figure 2.3) was defined in ABQUS to represent the traction-separation law and the cohesive-zone elements were specified on the crack plane ahead of the crack tip. The cohesive elements with zero initial thickness are embedded in between continuum elements in this work. Therefore, the cohesive elements act only as interfacial surface elements that deform according to the traction-separation law and consume the work of separation. The plastic deformation energy will be dissipated through the continuum elements. For example, in mode-I fracture, the top nodes (numbered 5-8) of the element are paired with the bottom nodes (numbered 1-4) to allow only normal separation. When the separation between a node pair reaches the critical separation δ_c, the traction is set to zero. This type of cohesive zone implementation is similar to the discrete cohesive zone approach advanced by Xie and Waas [50] and the references contained therein.

The mesh size of cohesive-zone elements dictates the convergence of numerical calculation. According to Tvergaard and Huchingson [34], if the ratio of element size to critical separation, (Δ_0 / δ_c), is chosen as 10 or smaller, the mesh size is adequate. For example, if a cohesive element has a specific work of separation at 13.5 kJ/m^2 (half of 27 kJ/m^2 due to symmetry) and a peak stress of 690 MPa, with δ_1 / δ_c = 0.001 and δ_2 / δ_c = 0.5, the critical separation δ_c is computed as

$$\Gamma_0 = \hat{\sigma}\left(0.5 + 0.5\frac{(\delta_2 - \delta_1)}{\delta_c}\right)\delta_c = 0.75\hat{\sigma}\delta_c \tag{6}$$

$$\delta_c = \frac{4}{3}\left(\frac{\Gamma_0}{\hat{\sigma}}\right) = \frac{4(13.5)}{3(690)} = 0.026 \text{ mm} \tag{7}$$

Therefore, a mesh size of 0.25 mm is sufficient for the cohesive element. This coincides with the conclusion of Roy and Dodd [38]. With a specific work of separation valued at 5 kJ/m^2 (half of 10 kJ/m^2 due to symmetry) and a peak stress of 500 MPa, δc is expressed as

$$\delta_c = \frac{4}{3}\left(\frac{\Gamma_0}{\hat{\sigma}}\right) = \frac{4(5)}{3(500)} = 0.013 \text{ mm} \tag{8}$$

Therefore, a mesh size of 0.1 mm is adequate.

Two geometries were used in this study: Kahn specimens [50] and single-notch specimens (Figures 2.4-2.5) with same thickness of 2 mm. Since both geometries and their boundary conditions feature both in-plane and out-of-plane symmetries, only one quarter (top half with half thickness) of the geometry was meshed. FE models of the two geometries are shown in Figures 2.6-2.7. The mesh size of cohesive-zone elements is 0.1 mm for all geometries, while the mesh becomes gradually coarser in areas away from the path of crack propagation.

Determination of Cohesive Parameters

Kahn specimens (Figure 2.4) were first tested to determine the CZM control parameters. The test setup is shown in Figure 2.8 and the tests were conducted in a screw-driven tensile test machine with a crosshead speed of 0.4 mm/min. The load was monitored through a machine-equipped load cell. It was not possible to mount an extensometer to the Kahn specimen and the measured crosshead displacements were not accurate. Instead, pictures were taken through a 2-Mega pixel digital camera to measure displacements. The gage length of crack tip opening was marked as 10 mm (Figure 2.8). Experimental data including loads and Notch Tip Opening Displacement (NTOD) from three tests are given in Figure 2.9. To analyze crack initiation and propagation, the surface crack extension was measured from the digital pictures and cross-plotted against NTOD (Figure 2.10). Substantial necking was also observed in experiments. The fractured surface doest not have a constant thickness through the crack plane. Instead, the thickness of the fractured surface is larger toward the notch and tapers off to a constant thickness of 0.6 mm (Figure

2.11). The region away from the notch is considered stress free and remains at 2 mm. The fracture profile in thickness direction exhibits pure mode-I fracture (Figure 2.13), similar to what was discovered by Pardoen et al. [52]. The significant necking as well as the mode-I fracture profile justifies the necessity of a 3-D FE model.

The specific work of separation has been identified to have a value of 13 ± 3 kJ/m^2 in a previous study of mode-I nugget fracture of Al5754-O spot welds [49]. Since Al5754-O is not sensitive to heat treatment, the effect of heat effect zone (HAZ) may be ignored.

The peak stress was then determined by a fitting procedure. To get a good fit with experimentally measured thickness of 0.6 mm after necking, the peak stress was determined to be 600 MPa (Figures 2.11-2.14). Because the resolution of the thickness measurement is 0.03 mm, the calibrated peak stress of 600 MPa is identified to have an uncertainty of ± 15 MPa, or less than 3%. A mesh size of 0.2 mm for cohesive-zone elements was also used in initial study. The results from the two different mesh sizes showed that the convergence has reached.

As a confirmation, there is a good agreement between the model and the experiment on the load-NTOD curves (Figure 2.15). On one hand, there is some amount of data scattering on experiments before and after the peak load. Cross examining the load-NTOD curves (Figure 2.9) and the NTOD-crack extension curves (Figure 2.10) reveals that crack initiation starts prior to reaching the peak load. Since no material variation exists (specimens were cut from the same bulk sheet along the same orientation) and no fatigue pre-crack was introduced to the Kahn specimens, the source of the data scattering is mainly credited to the geometrical variation around the notch and the uncertainty of crack initiations within different specimens. On the other hand, once the crack propagation reaches stable stage, the data scattering becomes very insignificant. Because no contribution from the CZM is expected before crack initiation, the discrepancy between the model and the experiment before crack initiation is caused by the deficiency of the continuum model. To show the effect of model uncertainty, the pairs of 10kJ/m^2

with 585MPa and 16kJ/m^2 with 615MPa were applied in the CZM. The model predictions varied only after the peak load, up to approximately ± 3% (Figure 2.16).

To further confirm that the values of the control parameters are adequately calibrated, the rate of crack propagation predicted by the model is comparable to experimental data (Figure 2.17). Nonetheless, the difficult to precisely measure the crack extension in experiment has caused some data scattering. In this study, the author relied on the light contrast between the specimen and the background to judge the location of crack front, therefore human error was easily introduced and it showed on Figure 2.10. In comparison, the identified uncertainty of the cohesive values has negligible effect on the predicted rate of crack propagation (Figures 2.17-18).

There has been some ambiguity about the size of the cohesive zone (Figure 2.19). If a cohesive zone includes a larger material zone, the cohesive-zone toughness will be higher since more material absorbs more energy, while the peak stress will be lower because the boundary of the cohesive zone is farther away from the necking zone. If the initial width is 0.2 mm, the cohesive zone has a volume of 0.2 mm x 2 mm x 20 mm and a row of 0.2 mm continuum material is added to the cohesive zone. Practically, it will be a challenge to define the right size of cohesive zone given the complexity of local deformation. To avoid any ambiguity, the initial width of the cohesive zone is set to zero, which means the specific work of separation for the cohesive zone equals to the actual work of fracture per unit area.

In summary, the mode-I specific work of separation has been previously determined to be 13 ± 3 kJ/m^2 [49] for aluminum Al5754-O and later the peak stress was calibrated to be 600 ± 15 MPa based on experimental data from Kahn specimens. The calibrated peak stress is about six times of the material's yield stress. To avoid any ambiguity, the initial width of the cohesive zone is set to zero and the zero-width cohesive zone elements are embedded between continuum elements as inter-facial surface elements.

Single-notch Specimen

Single-notch specimen is now used to check whether the calibrated cohesive values are geometry-dependent. As illustrated in Figures 2.4-2.5 and 2.6-2.7, a single-notch specimen is a different geometry from a Kahn specimen. Furthermore, a Kahn specimen is pulled through a pin (Figures 2.4 and 2.8), which allows rotation and leads to a more gradual crack propagation, while a single-notch specimen is stretched by fixture clamping (Figures 2.5 and 2.20), which prohibits rotation and promotes a more rapid crack growth. The gauge length for the single-notch specimen was also marked as 10 mm (Figure 2.20). To show the difference between the two specimens from experimental results, the rate of crack propagation in the Kahn specimen was compared to that in the single-notch specimen (Figure 2.21). The crack grows steadily in the Kahn specimen and extends a length of 10 mm over a NTOD of 5 mm, while in the single-notch specimen the crack growth accelerates with the increase of NTOD and the crack develops a length of 14 mm over a NTOD of less than 3 mm.

The FE model, with the pair of 13 kJ/m^2 and 600 MPa, simulated the thickness of fractured surface: larger toward the notch and tapering off to a constant thickness of 0.6 mm, versus an initial thickness of 2 mm, which agrees with experimental measurements. The load-NTOD curve predicted by the model also correlates well with the tests up to a NTOD of 3 mm (Figure 2.22). In addition, the simulated rate of crack growth compares well with experimental measurements up to a NTOD of 3 mm (Figure 2.23). For NTOD over 3 mm, the model over-predicted the load and under-predicted the rate of crack growth. On one hand, there was probably some unstable crack propagation in experiments due to both the release of the energy stored in test fixtures and the loading rate of 0.4 mm/minute. On the other hand, the model is only suited for a static loading and a perfect fixture rigidity is assumed. To examine how the uncertainty of cohesive values affects the model predictions, the pairs of $10kJ/m^2$ with 585MPa and $16kJ/m^2$ with 615MPa were also applied in the CZM and the model uncertainty was shown to be up to ± 4% (Figures 2.22b and 2.23b). Therefore, it is concluded that the cohesive values calibrated from Kahn specimen are applicable to single-notch geometry.

Fracture Criteria of Equivalent Plastic Strain

The equivalent plastic strain (EPS) has been related to the fracture in sheet metal forming in the past. Due to its simplicity, it has also been used in commercial FEA codes such as LS-DYNA to simulate crack initiation and growth: once the plastic strain in an element reaches an EPS limit, the element will be excluded from the structure stiffness [53]. In this study, the 3-D user-defined cohesive element in ABAQUS was modified and allowed to fail once its neighboring continuum element deforms to the specified EPS limit of 20% (equivalent to the maximum uniform elongation of 22%). Using this method the fracture propagation was simulated for both Kahn and single-notch specimens. It is shown that these models with the EPS limit of 20% significantly underestimate the load-carrying capacity (Figures 2.24-2.25) compared to the CZM. It is a challenge to find the right EPS limit.

Conclusions

To understand the mode-I fracture of sheet Al5754-O, a 3-D cohesive model was implemented into the commercial FE code ABAQUS. After the stress-strain curve was obtained through tensile tests, mode-I fracture geometries including Khan specimen and single-notch specimen, both made from 2 mm Al5754-O sheet, were used to study the geometrical dependence of the cohesive parameters. The specific work of separation has been identified to be 13 ± 3 kJ/m^2 in a previous work [48] and the peak stress was determined to be 600 ± 15 MPa based on experimental data. The identified cohesive values were then found to be applicable to the single-notch geometry within the limits of the models. The single-notch geometry is shown to be dissimilar from the Kahn geometry and the applied boundary conditions are also different. However, both Kahn specimens and single-notch specimens underwent large-scale plastic deformation and the necking ratio, defined as the ratio of final to initial thickness, is 0.3 for both geometries. The peak stress or the maximum true stress at separation is about six times of the yield stress for the necking ratio of 0.3. It needs further investigation whether the calibrated cohesive

values are still applicable if the degree of plastic deformation varies. The thickness effect on the cohesive parameters will also be examined in next chapter.

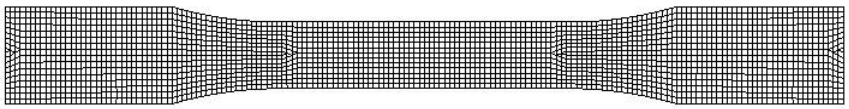

Figure 2.1 Mesh of ASTM-638 Dogbone Specimen [44]. Specimen thickness is 2 mm.

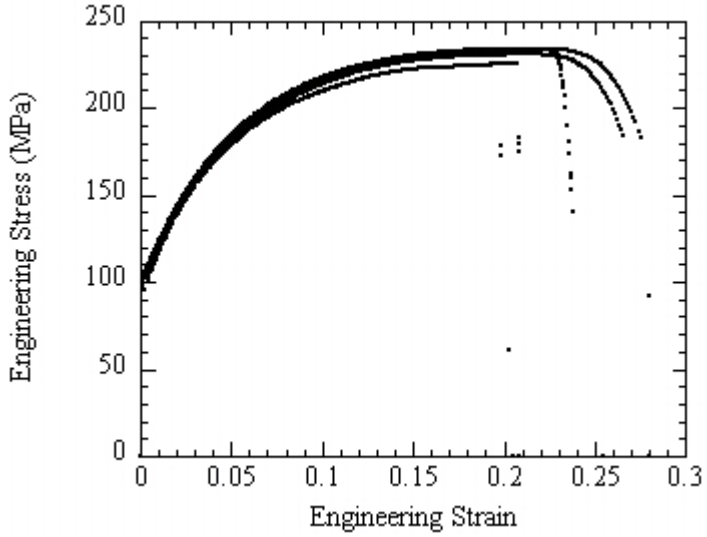

Figure 2.2 Experimental stress-strain curves of Al5754-O.

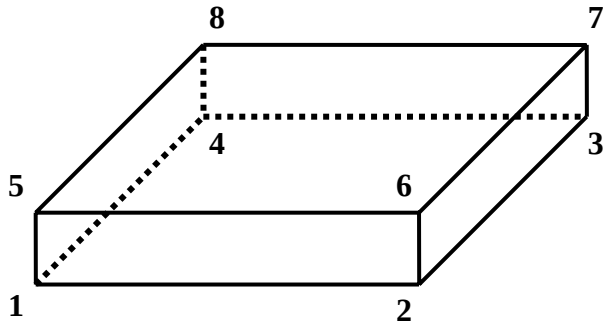

Figure 2.3 3-D 8-node bilinear cohesive-zone user element.

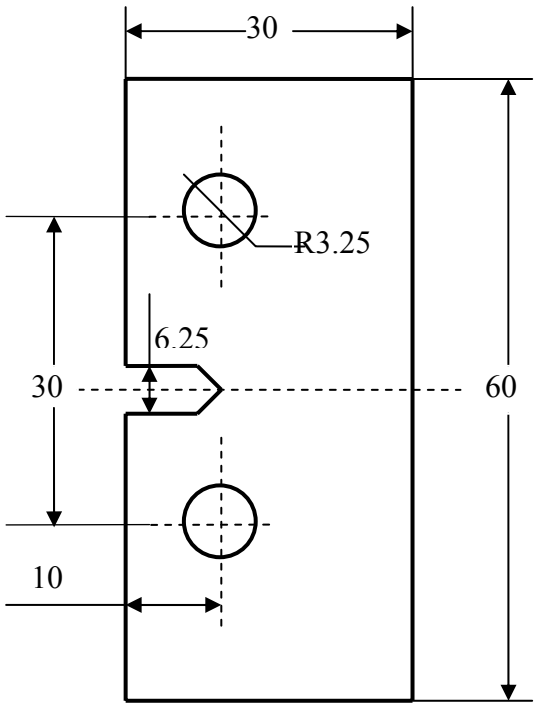

Figure 2.4 Kahn specimen with thickness of 2 mm. All units are in mm.

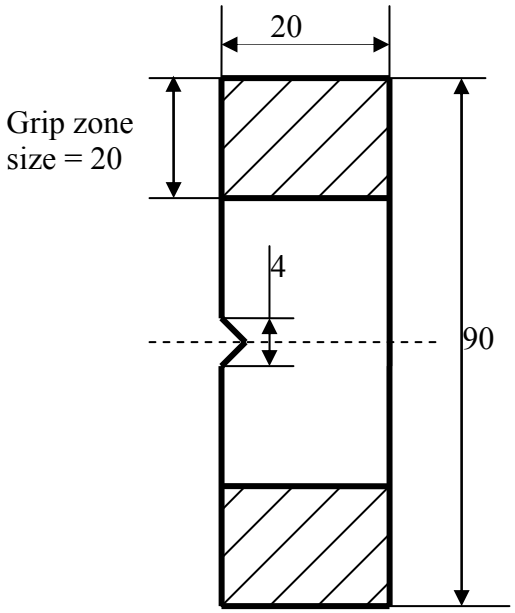

Figure 2.5 Single-notch specimen with thickness of 2 mm. All units are in mm.

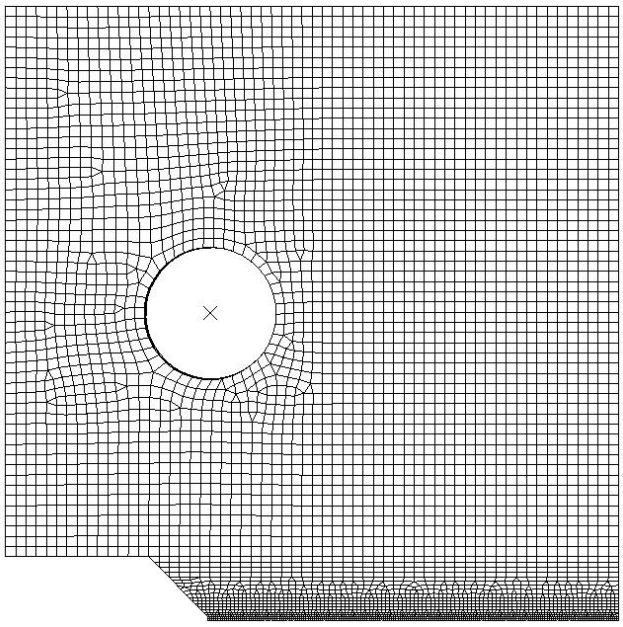

Figure 2.6 Kahn model with cohesive-zone elements of 0.1 mm. Pin-loading was applied at the loading point to allow rotation.

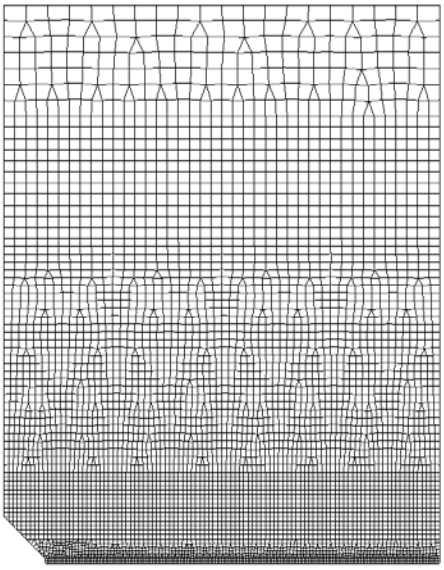

Figure 2.7 Single-notch model with cohesive-zone elements of 0.1 mm. Top edge was clamped to limit rotation.

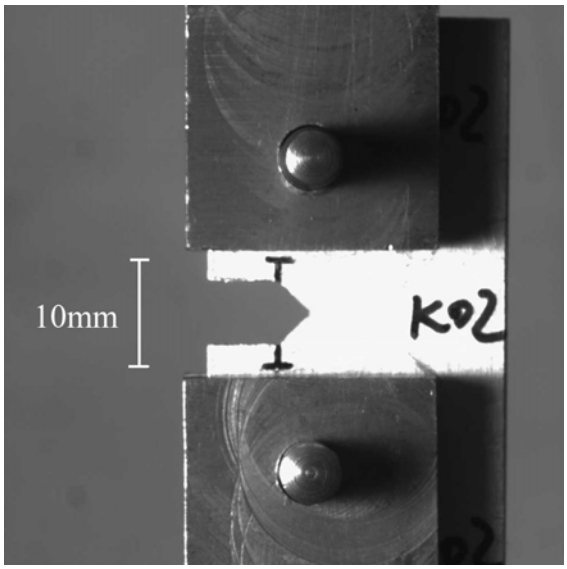

Figure 2.8 Kahn specimen test setup. The 10 mm gage mark was used to measure Notch Tip Opening Displacement (NTOD).

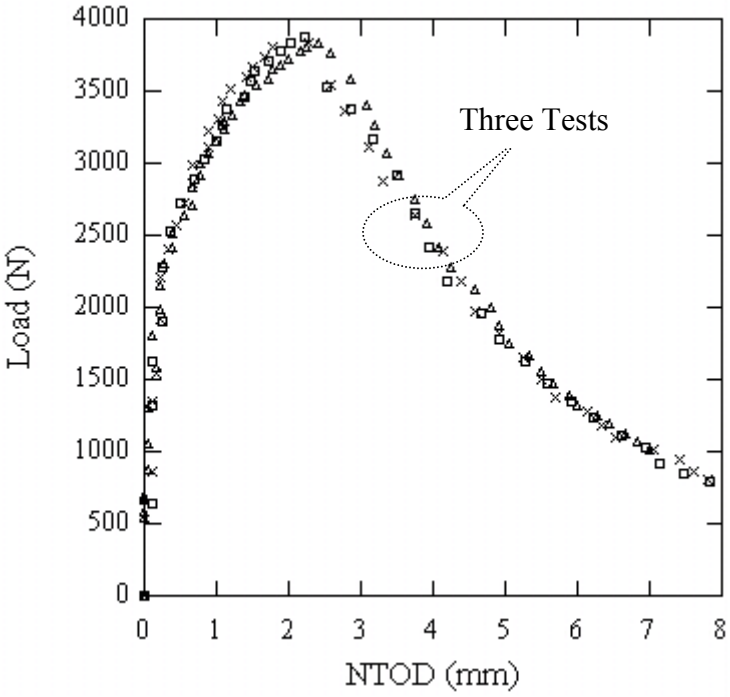

Figure 2.9 Experimental load-NTOD curves for three Kahn specimens.

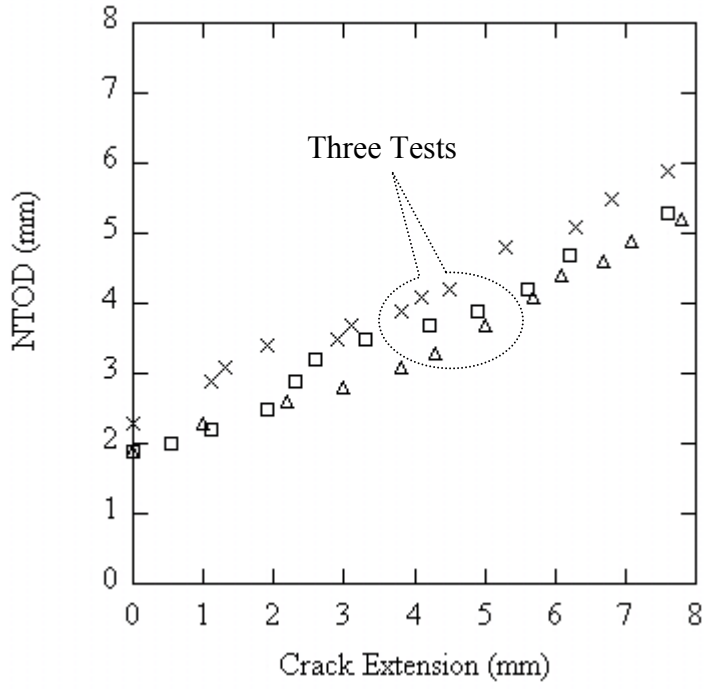

Figure 2.10 Experimental NTOD-surface crack extension for three Kahn specimens.

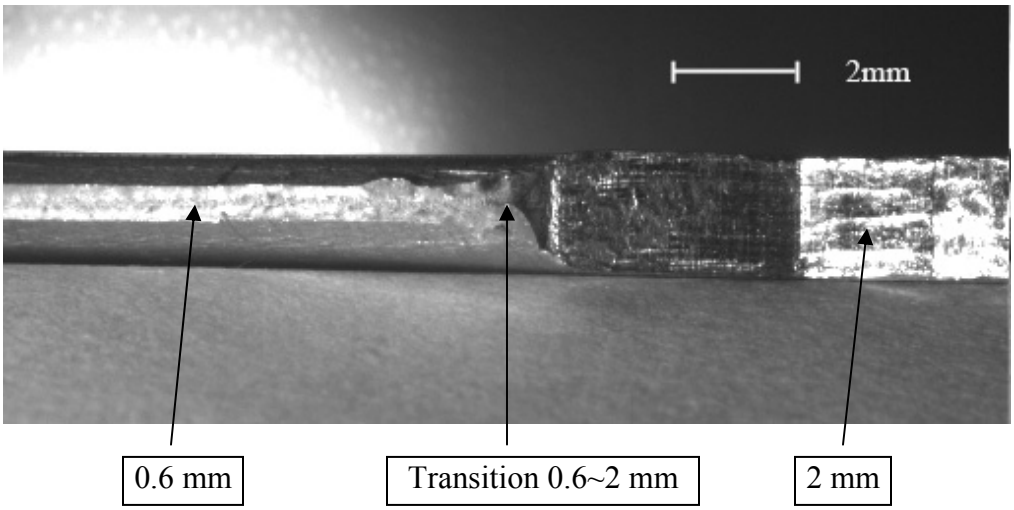

Figure 2.11 Experimental necking profile for Kahn-specimen.

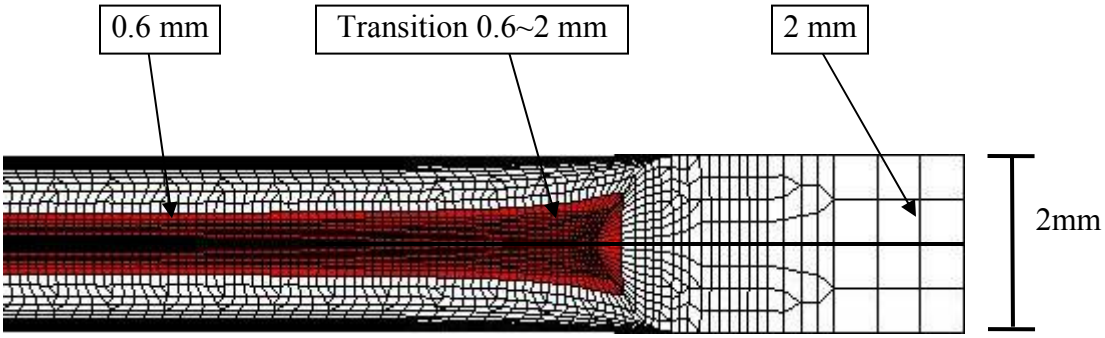

Figure 2.12 Simulated necking profile for Kahn-specimen.
Picture mirrored to aid visualization.

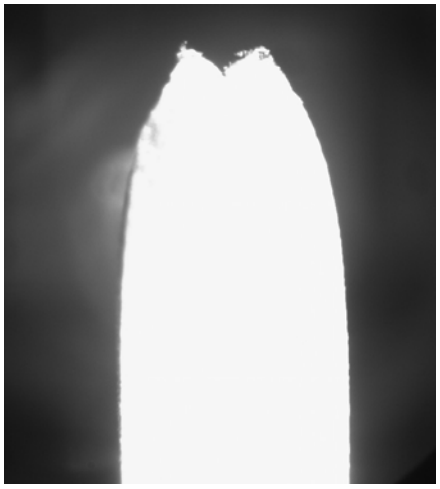

2 mm

Figure 2.13 Experimental fracture profile for Kahn specimen. Section cut through the thickness direction.

2 mm

Figure 2.14 Simulated fracture profile for Kahn specimen. Section cut through the thickness direction. Picture mirrored to aid visualization.

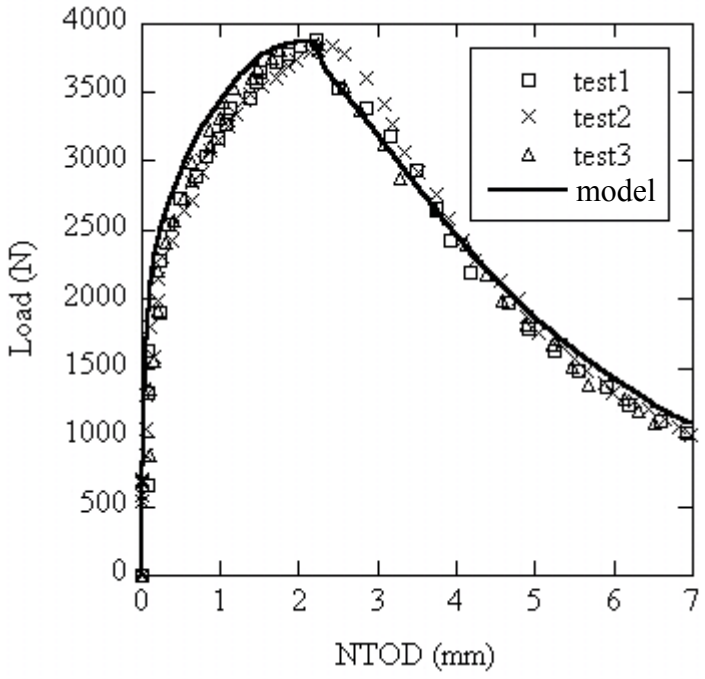

Figure 2.15 Load-NTOD curves for Kahn specimen: test versus model.

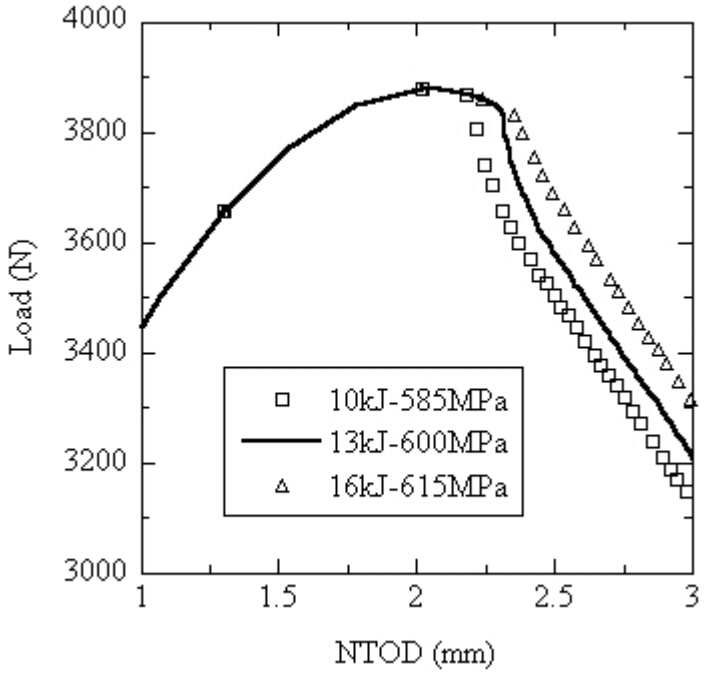

Figure 2.16 Load-NTOD curves for Kahn specimen of 2 mm predicted by CZM with different cohesive values of 10kJ/m^2 with 585 MPa, 13kJ/m^2 with 600 MPa and 16kJ/m^2 with 615 MPa. The model uncertainty does not have any effect before crack initiation and the predicted load after crack initiation varies up to ± 3%.

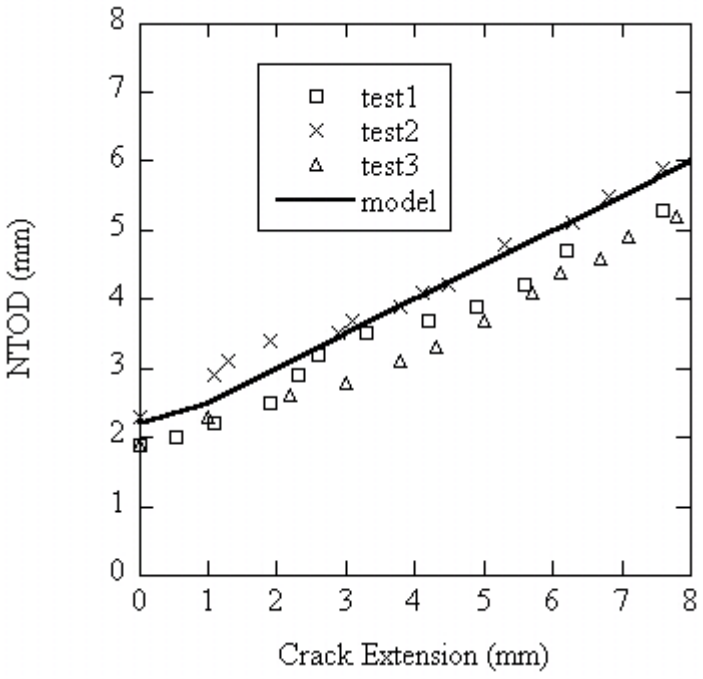

Figure 2.17 NTOD-surface crack extension for Kahn specimen: test vs. model.

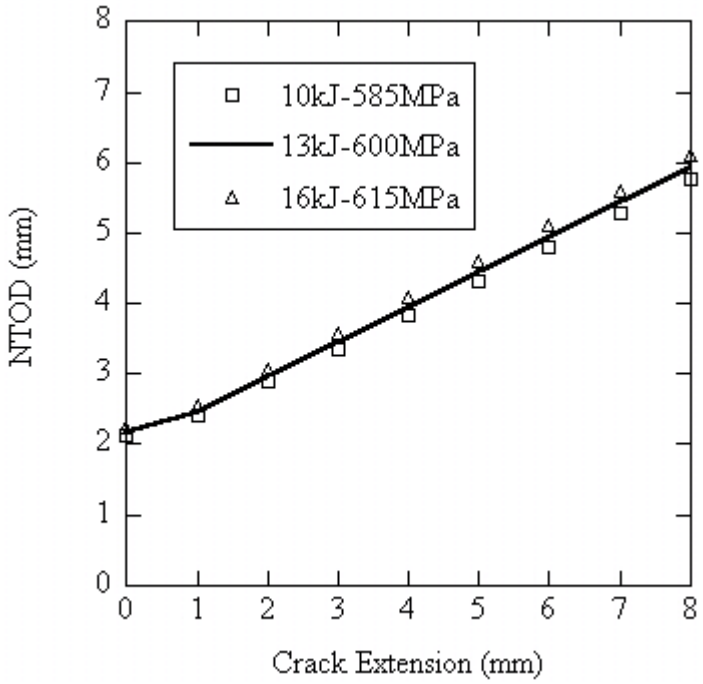

Figure 2.18 NTOD - surface crack extension for Kahn specimen of 2 mm predicted by CZM with different cohesive values of 10kJ/m^2 with 585 MPa, 13kJ/m^2 with 600 MPa and 16kJ/m^2 with 615 MPa. The model uncertainty is insignificant.

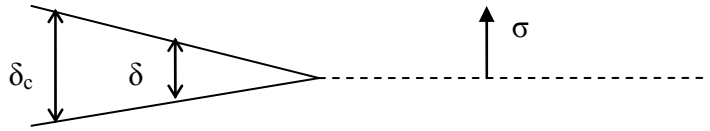

Fracture Process Zone Encompassing Zero Initial Width

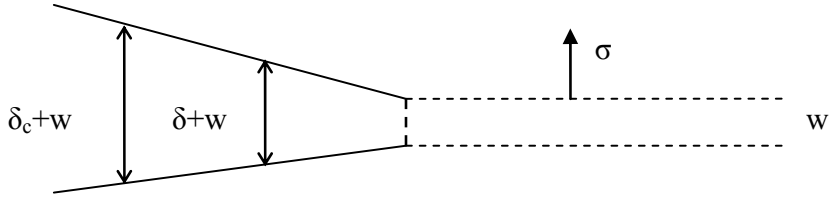

Fracture Process Zone Encompassing Finite Initial Width w

Figure 2.19 Two different scales of cohesive zone.

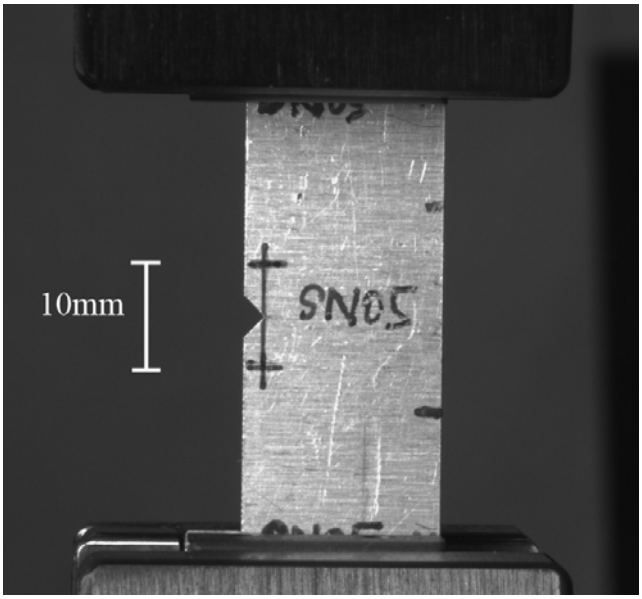

Figure 2.20 Single-notch specimen test setup.

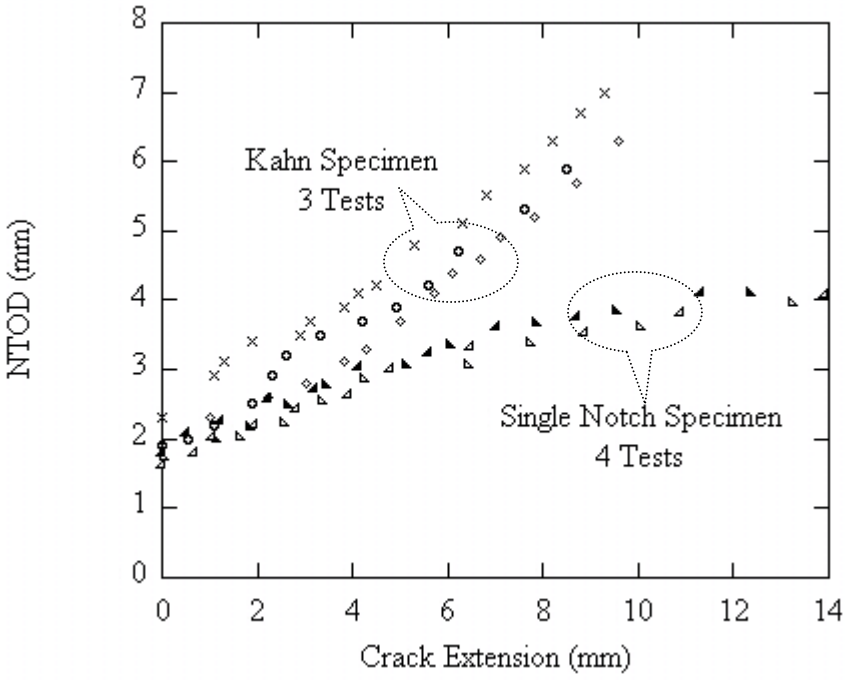

Figure 2.21 Experimental NTOD-surface crack extension for Kahn and single-notch specimens. All specimens are 2 mm thick.

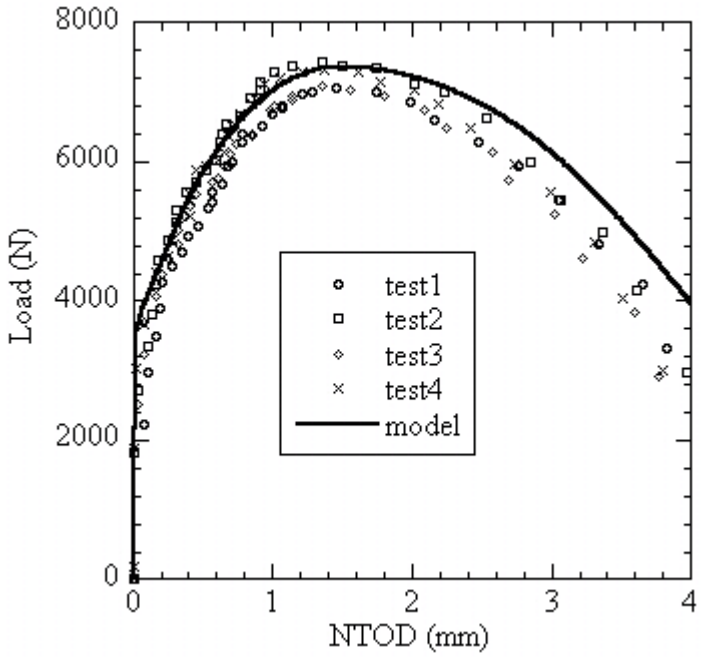

Figure 2.22 Load-NTOD for single-notch specimen: model versus tests.

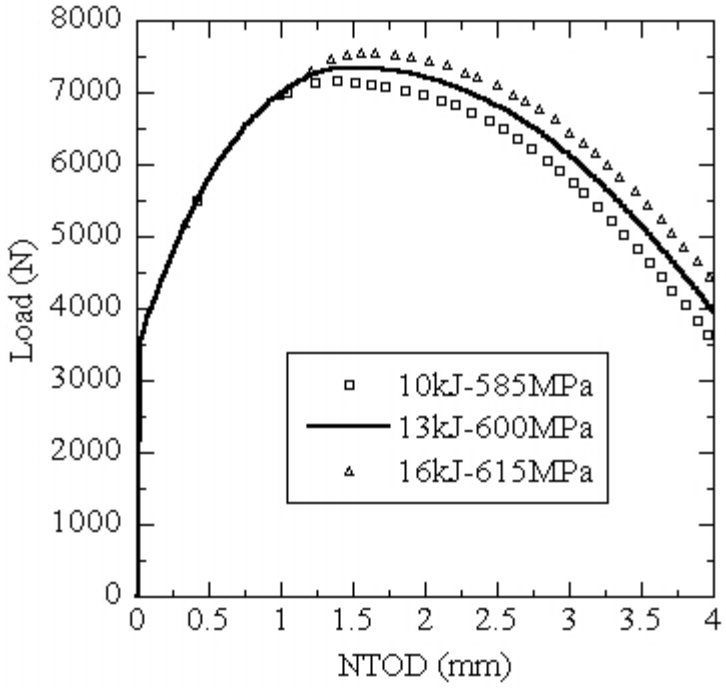

Figure 2.22b Load-NTOD curves for single-notch specimen of 2 mm predicted by CZM with different cohesive values of 10kJ/m^2 with 585 MPa, 13kJ/m^2 with 600 MPa and 16kJ/m^2 with 615 MPa. The predicted load varies up to ± 4%.

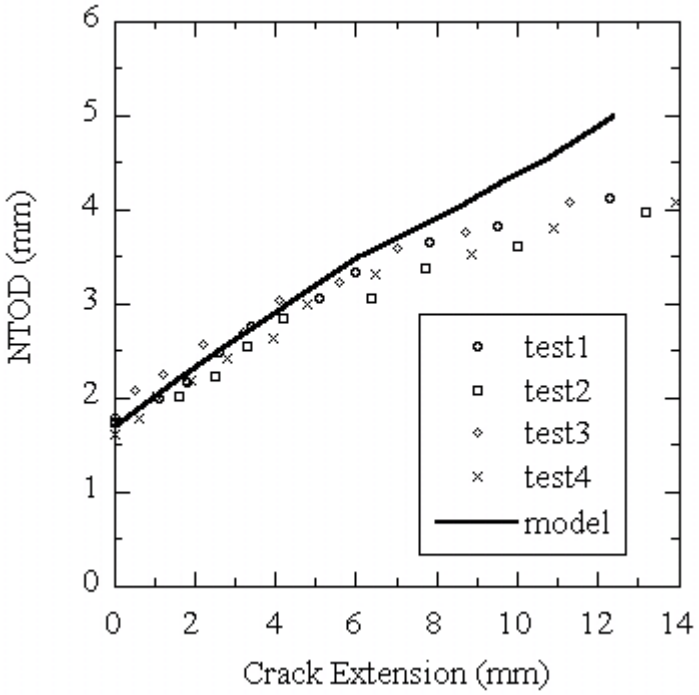

Figure 2.23 NTOD-crack extension for single-notch specimen: model versus tests.

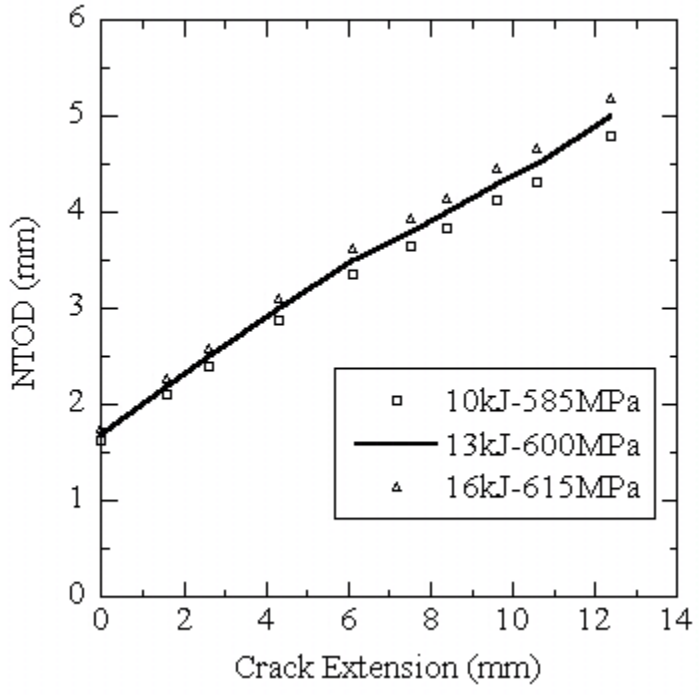

Figure 2.23b NTOD-crack extension for single-notch specimen of 2 mm predicted by CZM with different cohesive values of 10kJ/m^2 with 585 MPa, 13kJ/m^2 with 600 MPa and 16kJ/m^2 with 615 MPa. The model prediction varies up to ± 4%.

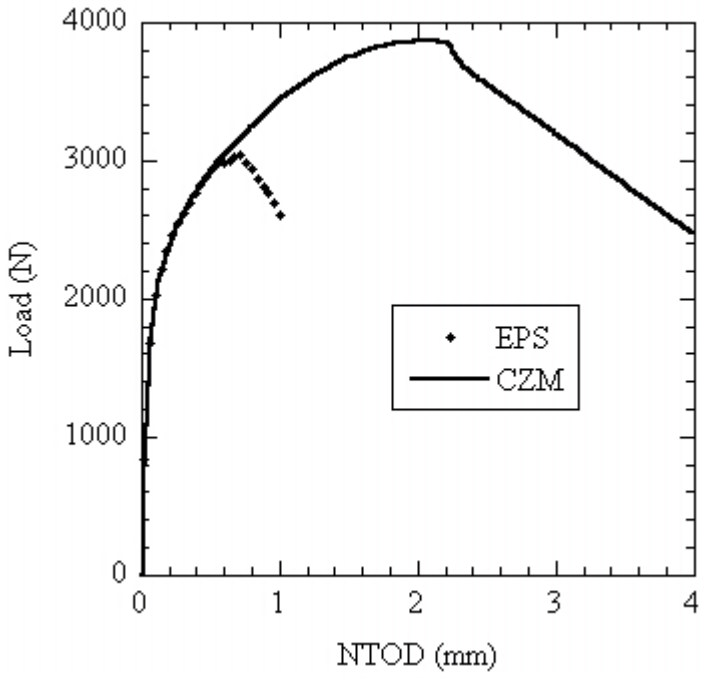

Figure 2.24 Load-NTOD for Kahn specimen of 2 mm predicted by CZM and EPS. The cohesive zone model (CZM) has a specific work of separation of 13 kJ/m^2 and a peak stress of 600 MPa. The model with failure criterion of equivalent plastic strain (EPS) has a limit of 20%.

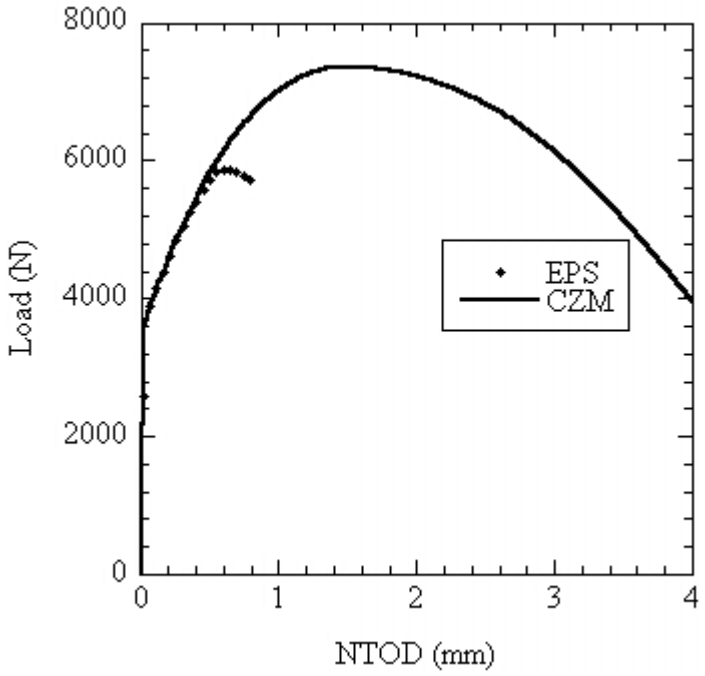

Figure 2.25 Load-NTOD for single-notch specimen of 2 mm predicted by CZM and EPS. The cohesive zone model (CZM) has a specific work of separation of 13 kJ/m^2 and a peak stress of 600 MPa. The model with failure criterion of equivalent plastic strain (EPS) has a limit of 20%.

References

1. A. K. Pickett, T. Pyttel, F. Payen, F. Lauro, N. Petrinic, H. Werner, J. Christlein, "Failure prediction for advanced crashworthiness of transportation vehicles," *International Journal of Impact Engineering*, **30,** 853–872 (2004).

2. M. G. Cockcroft, D. J. Latham, "Ductility and workability of metals," *Journal of the Institute of Metals*, **96**, 33-39 (1968).

3. S. E. Clift, P. Hartley, C. E. N. Sturgess, G. W. Rowe, **"**Fracture prediction in plastic deformation processes," *International Journal of Mechanical Sciences*, **32**, 1-17 (1990).

4. T. Dsoki, E. Doege, P. Groche, "Prediction of cracks in sheet-metal forming with FEM-simulations", SAE-917089, 1991.

5. T. Ogawa, T. Hamaguchi, "Development of stamping simulation through all processes", SAE-1999-08-0274, 1999.

6. J. P. Domblesky, L. Zhao, "Assessment of a finite element model for plate shearing", *Journal of Engineering Manufacture*, **216**, 519-529 (2002).

7. J. C. Anderson, K. D. Leaver, R. D. Rawlings and J. M. Alexander, p. 223-225 in *Materials Science*, Fourth Edition, Chapman & Hall (1990).

8. G. R. Irwin, p. 557-591 in *Fracture mechanics. Structural Mechanics*, Pergamon, Elmsford, NY (1960).

9. J. R. Rice, "A Path Independent Integral and the Approximate Analysis of Strain Concentration by Notches and Cracks", *Journal of Applied Mechanics*, *Transactions of the ASME*, 379-386 (June 1968).

10. R. H. Dodds Jr., W. C. Carpenter, W. A. Sorem, "Numerical evaluation of a 3-D J-integral and comparison with experimental results for a 3-point bend specimen", *Engineering Fracture Mechanics*, **29**, 275-285 (1988).

11. T. Pardoen, Y. Marchal, F. Delannay, "Thickness dependence of cracking resistance in thin aluminum plates", *Journal of the Mechanics and Physics of Solids*, **47**, 2093-2123 (1999).

12. G. B. May, A. S. Kobayashi, "Plane stress stable crack growth and J-integral/HRR field", *International Journal of Solids and Structures*, **32**, 857-881 (1995).

13. W. Brocks, P. Negre, I. Scheider, M. Schodel, D. Steglich, U. Zerbst, "Structural Integrity Assessment by Models of Ductile Crack Extension in Sheet Metal", *Steel Research International*, **74**, 504-513 (2003).

14. J. C. Newman Jr., M. A. James, U. Zerbst, “review of the CTOA/CTOD fracture criterion”, *Engineering Fracture Mechanics*, **70**, 371–385 (2003).

15. M. A. James, J. C. Newman Jr., “Three-dimensional analyses of crack-tip-opening angles and d5-resistance curves for 2024-T351 aluminum alloy”, *ASTM Special Technical Publication*, **1406**, 279–297 (2002).

16. J. C. Newman Jr., B. R. Seshadri, D. S. Dawicke, “Residual strength analyses of stiffened and unstiffened panels—Part I: laboratory specimens”, *Engineering Fracture Mechanic,* **70**, 493–507 (2003).

17. J. C. Newman Jr., B. R. Seshadri, D. S. Dawicke, “Residual strength analyses of stiffened and unstiffened panels—Part II: wide panels”, *Engineering Fracture Mechanic,* **70**, 509–524 (2003).

18. D. S. Dawicke, M. A. Sutton MA, “CTOA and crack-tunneling measurements in thin sheet 2024-T3 aluminum alloy”, *Experimental Mechanics*, **34**, 357–368 (1994).

19. D. S. Dawicke, J. C. Newman Jr., C. A. Bigelow, “Three-dimensional CTOA and constraint effects during stable tearing in a thin-sheet material”, *ASTM Special Technical Publication*, **1256**, 223–242 (1995).

20. D. S. Dawicke, J. C. Newman Jr., “Residual strength predictions for multiple-site damage using a three-dimensional finite-element analysis and a CTOA criterion”, *ASTM Special Technical Publication*, **1332**, 815–829 (1999).

21. A. S. Gullerud, R. H. DODDS JR. Jr., R. W. Hampton, D. S. Dawicke, “Three-dimensional modeling of ductile crack growth in thin sheet metals: computational aspects and validation”, *Engineering Fracture Mechanic,* **63**, 347–374 (1999).

22. S. Mahmoud, K. Lease, “Two-dimensional and three-dimensional finite element analysis of critical crack-tip-opening angle in 2024-T351 aluminum alloy at four thickness”, *Engineering Fracture Mechanic,* **71**, 1379-1391 (2004).

23. S. Mahmoud, K.Lease, “The effect of specimen thickness on the experimental characterization of critical crack tip opening angle in 2024-T351 aluminum alloy”, *Engineering Fracture Mechanic,* **70**, 443–456 (2003).

24. A. L. Gurson, “Continuum theory of ductile rupture by void nucleation and growth, Part I—Yield criteria and flow rules for porous ductile media”, *Journal of Engineering Material Technology*, **99**, 2–15 (1977).

25. A. Needleman, V. Tvergaard, “An analysis of ductile rupture in notched bars”, *Journal of Mechanics and Physics of Solids,* **32**, 461–490 (1984).

26. V. Tvergaard, A. Needleman, "Analysis of the cup-cone fracture in a round tensile bar", *Acta Metallurgica*, **32**, 157–169 (1984).

27. L. Xia, C. F. Shih, "Ductile crack growth – I. A numerical study using computational cells with microstructually-based length scales", *Journal of the Mechanics and Physics of Solids*, **43**, 233-259 (1995).

28. L. Xia, C. F. Shih, J. W. Hutchinson, "A computational approach to ductile crack growth under large scale yielding conditions", *Journal of the Mechanics and Physics of Solids*, **43**, 389-413 (1995).

29. O. Chabanet, D. Steglich, J. Besson, V. Heitmann, D. Hellmann, W. Brocks, "Predicting crack growth resistance of aluminum sheets", *Computational Materials Science*, **26**, 1-12 (2003).

30. G. I. Barenblatt, "Equilibrium cracks formed during brittle fracture", *Journal of Applied Mathematics and Mechanics*, **23**, 1273-1282 (1959).

31. D. S. Dugdale, "Yielding of steel sheets containing slits", *Journal of the Mechanics and Physics of Solids*, **8**, 100–104 (1960).

32. A. Needleman, "A Continuum Model for Void Nucleation by Inclusion Debonding", *Journal of Applied Mechanics*, *Transactions of the ASME*, **54**, 525-531 (1987).

33. A. Needleman, "An Analysis of Tensile Decohesion along an Interface", *Journal of the Mechanics and Physics of Solids*, **38**, 289-324 (1990).

34. V. Tvergaard, J. W. Hutchinson, "The relation between crack growth resistance and fracture process parameters in elastic-plastic solids", *Journal of the Mechanics and Physics of Solids*, **40**, 1277-1397 (1992).

35. V. Tvergaard, J. W. Hutchinson, "Effect of T-stress on mode I crack growth resistance in a ductile solid", *International Journal of Solids and Structures*, **31**, 823-833 (1994).

36. V. Tvergaard, J. W. Hutchinson, "Effect of strain-dependent cohesive model on predictions of crack growth resistance", *International Journal of Solids and Structures*, **33**, 3297-3308 (1996).

37. Y. Arun Roy, R. H. Dodds Jr., "Simulation of ductile crack growth in thin aluminum panels using 3-D surface cohesive elements", *International Journal of Fracture*, **110**, 21–45 (2001).

38. W. Li, T. Siegmund, "An analysis of crack growth in thin-sheet metal via a cohesive zone model", *Engineering Fracture Mechanics*, **69**, 2073-2093 (2002).

39. A. Cornec, I. Scheider, Ingo, K. Schwalbe, "On the practical application of the cohesive model", *Engineering Fracture Mechanics*, **70**, 1963-1987 (2003).

40. T. Siegmund, W. Brocks, "Prediction of the work of separation and implications to modeling", *International Journal of Fracture*, **99**, 97-116 (1999).

41. C. R. Chen, O. Kolednik, I. Scheider, T. Siegmund, A. Tatschl, F. D. Fischer, "On the determination of the cohesive zone parameters for the modeling of micro-ductile crack growth in thick specimens", *International Journal of Fracture*, **120**, 517-536 (2003).

42. C. L. Hom, R. M. McMeeking, "Large crack tip opening in thin elastic–plastic sheets", *International Journal of Fracture*, **45**, 103–122 (1990).

43. J. W. Hutchinson, A. G. Evans, "Mechanics of materials: top-down approaches to fracture", *Acta Metallurgica*, **48** 125-135 (2000).

44. http://www.matweb.com/, Metal; Nonferrous Metal; Aluminum Alloy; 5000 Series Aluminum Alloy, Aluminum 5657-O, *Mechanical Properties*.

45. ASTM D638 - 03, Standard Test Method for Tensile Properties of Plastics, Jan. 2004.

46. W. F. Hosford, "The Anisotropy of Aluminum and Aluminum Alloys", *Journal of the Minerals, Metals and Materials Society*, volume **58**, number 5, 70-74 (2006).

47. H. Li, N. Chandra, "Analysis of crack growth and crack-tip plasticity in ductile materials using cohesive zone models", *International Journal of Plasticity*, **19**, 849–882 (2003).

48. Q. Yang, *Fracture analyses of plastically-deforming adhesive joints*, Ph.D. Thesis, University of Michigan, Ann Arbor (2000).

49. M. N. Cavalli, *Cohesive Zone Modeling of Structural Joint Failure*, Ph.D. Thesis, University of Michigan, Ann Arbor (2003).

50. D. Xie, A. M. Waas, "Discrete cohesive zone model for mixed-mode fracture using finite element analysis", *Engineering Fracture Mechanics*, **73**, 1783-1796 (2006).

51. N. Kahn, E. Imbembo, "Method of evaluating transition from shear to cleavage failure in ship plate and its correlation with large-scale plate tests", *Welding Journal*, **27**, 169–182 (1948).

52. T. Pardoen, F. Hachez, B. Marchioni, P.H. Blyth, A.G. Atkins, "Mode I fracture of sheet metal", *Journal of the Mechanics and Physics of Solids*, **52,** 423 – 452 (2004).

53. LSTC, *LS-DYNA keyword user's manual*, version 970, April 2003.

Chapter 3

Mode-I Fracture of Aluminum Sheets: Thickness Effect

Introduction

Fracture toughness, as defined at the beginning of this work, depends on the degree of plastic deformation. At larger thickness, fracture toughness typically decreases with increase of thickness due to reduction of plastic deformation and reaches a constant for a plain-strain condition. However, at smaller thickness for a plane-stress more investigation is needed. If flat fracture is a surface phenomenon and shear mode is dominant, the critical energy release rate, G_{crit}, was proposed to be linearly dependent on specimen thickness t at small thickness where a plane-stress state is developed [1]

$$G_{crit}^{shear} = ct \tag{1}$$

where c is a material constant. Similarly it is shown that, if the specimens are very thin and the fracture is 100 percent slant fracture, the critical energy release rate may be written as [2]

$$G_{crit}^{shear} = 2\sigma_y t \tag{2}$$

where σ_y is the yield stress and t the thickness of thin sheet. Test data for Al7075 – T6 reflects this trend and equation 2 is valid for small-scale plastic deformation. If the fracture is preceded with necking and thinning of the sheet, it is not clear whether the crack tip actually advances by mode-I or mode-II fracture. Recently, it has been observed that the mode-I fracture toughness increases with the increase of thickness at plane-stress state for high-strength maraging steel [3].

The concept of essential work of fracture has also been developed to measure the total work of mode-I fracture in the presence of large-scale plastic deformation [4]: the work required to fracture a double-edge notched tension (DENT) specimen is partitioned into the essential work performed in the end region and the non-essential work in the screening plastic region. The specific essential work of fracture (the essential work in the end region per unit area of crack extension), w_e, proportional to $\sigma_u t$, is a linear function of specimen thickness t, where σ_u is the ultimate tensile strength. This linear relationship has been confirmed in a mode-I study of Al6082-O thin plates [5].

The crack tip opening displacement (CTOD) was shown, both analytically and experimentally, to be linearly dependent on the sheet thickness in edge-slotted silicon steel coupons [6] for mode-I fracture. Now consider a general relationship [3] between the critical J-integral, J_c, and the critical CTOD, δ_c,

$$J_c = 1.7\sigma_{flow}\delta_c \tag{3}$$

where E is Young's modulus and σ_{flow} is the average of yield strength and tensile strength. Given CTOD's linear dependence on the thickness, the fracture toughness characterized by J_c scales with thickness. For example, it is shown that the specific essential work of fracture, the critical J-integral, and the critical CTOD are proportional to the thickness of thin DENT specimens for mode-I fracture of Al6082-O [5].

This chapter examines the effects of sheet thickness on cohesive-zone parameters. First proposed by Barrenblatt [7] and Dugdale [8], the CZM has been recently embedded in FE codes to model crack initiation and propagation. It has been shown in chapter 2 that the identified values of cohesive parameters apply to different geometries under large-scale plastic deformation. It remains to be seen whether the CZM parameters including the peak stress and the specific work of separation are thickness-dependent. The effect of thickness will be first examined for Al5754-O using Kahn specimens of 1 mm, 1.6 mm and 2 mm. The calibrated cohesive values will also be applied to simulate the plane-strain condition as well as the mode-I fracture of Al5754-O spot-weld nugget. Then the fracture in a deep double-notch specimen will be examined. In addition, the CZM will be used to model mode-I fracture of Al6082-O using DENT specimens of 1mm, 2mm and 3 mm.

Finally, the role of plastic deformation on fracture toughness will be discussed and the thickness effect on the cohesive parameters will be concluded.

Thickness Effect for Al5754-O

Mechanical properties for Al5754-O have been identified in chapter 2 to have a yield strength of 100 MPa and a true tensile strength of 285 MPa. And the true stress-strain relationship is represented by the power law:

$$\sigma = 393\varepsilon^{0.2} \text{ MPa} \tag{4}$$

Kahn specimens of 1mm were prepared by machining 4mm wide groove in the 2mm plate and 0.5mm thick material was cut off on each side (Figure 3.1). The benefits of machining only a groove, as opposed to the whole specimen, are twofold: firstly, it reduces the chance of buckling; secondly, it avoids excessive machining. Similarly, Kahn specimens of 1.6 mm were prepared and 0.2mm thick material was cut on each side. From both experimental observation and numerical calculation, the plastic deformation outside the 4 mm groove was found to be minor. Therefore, expanding the 4 mm groove will not add substantial benefits. To verify that the machining process does not alter the mechanical properties of prepared specimens due to heat or strain hardening, surface hardness was measured for machined Kahn specimens. Through a Vickers indenter, with test parameters of 30 seconds duration and 1 kg force, the hardness of 2 mm specimen was measured as 64.5 HV and the hardness of 1 mm specimen 65.0 HV. It is then concluded that the mechanical property is not affected by the machining process.

Kahn specimens of 1 mm and 1.6 mm were tested same as 2 mm Kahn specimens (Figure 3.2). Experimental load-NTOD curves for three different Kahn specimens were plotted together and the peak loads of 3880 N, 3130 N, and 2000 N were measured for Kahn specimens of 2 mm, 1.6 mm and 1 mm, respectively (Figure 3.3). Normalized by 3880, these peak loads arrive at ratios of 1, 0.81, and 0.52, respectively, and correlate very well with thickness ratios. This also confirms that the load carrying capacity of thinner

specimens is not altered significantly by the reinforcement of 2 mm bulk material and choosing 4 mm groove is adequate.

The specific work of separation of 13 ± 3 kJ/m^2 and the peak stress of 600 ± 15 MPa were used in the FE models and model predictions compare well with experimental data in both load-CTOD and CTOD-crack extension curves (Figures 3.4–3.7). The effect of cohesive parameter variation is shown in Figures 3.4a-3.7a. The final necked thicknesses were measured from experiments and arrived at a constant ratio of 0.3 after normalized by initial thicknesses. The predicted ratios of 0.30, 0.29, and 0.28, for Kahn specimens of 2 mm, 1.6 mm and 1 mm, respectively, are in good agreement with experiments. The comparison of necking profiles between experiments and model simulation are shown in Figures 3.8 and 3.9. The fracture toughness at stable crack growth was also calculated from the models to be 363 kJ/m^2, 276 kJ/m^2, and 180 kJ/m^2 for Kahn specimens of 2 mm, 1.6 mm, and 1.0 mm, respectively. As a result, the computed toughness scales with the specimen thickness (Figure 3.10). High values of fracture toughness, compared to the specific work of separation at 13 ± 3 kJ/m^2, are contributed largely by large-scale plastic deformation.

It has been shown that the calibrated cohesive parameters apply to different thicknesses of same geometries where a large-scale plastic deformation is present. However, all these specimens have relatively small thickness and the range of stress-triaxility is also small. One question arises: can the application be extended to very thick specimen or plane-strain condition where through-thickness deformation is limited? To begin with, a FE calculation with the CZM was conducted on the Kahn specimen to simulate the plane-strain condition for Al5754-O. All nodes in the FE model were constrained to have zero out-of-plane displacement. The pair of 13 kJ/m^2 and 600 MPa was first applied in the model and there was no crack growth at all. Given the true stress of 285 MPa at the onset of necking in the tensile test, it is argued that the cohesive peak stress is lower-bounded by 285 MPa. Then a pair of 13 kJ/m^2 and 285 MPa was applied to the model of Kahn specimen under plane-strain constraint and stable crack growth was achieved in the presence of small-scale plastic deformation. With little contribution from plastic

deformation, the fracture toughness was computed to be 13 kJ/m^2, which is then identified as specific work of separation.

The specific work of separation of 13 kJ/m^2 and the peak stress of 285 MPa were also applied to simulate the mode-I fracture of spot-weld nugget [9]. This is considered possible because the geometrical constraint limits the necking of the weld nugget and Al5754-O is non-heat treatable so the effect of heat affect zone can be ignored. Take the example of coach-peel spot-weld (Figure 3.11). The nugget size is only 5 mm, compared to an out-of-plane width of 25 mm. Therefore, the deformation through the width of the coach-peel specimen is limited and the nugget necking is difficult to develop. The FE model with coupled 2-D and 3-D mesh was prepared to reduce the size of model while maintaining a 0.1 mm mesh size of cohesive zone elements (Figure 3.12). The intersection between the base material and the nugget was treated as a notch, not a crack [10], illustrated in Figure 3.13. Due to symmetry, only one eighth of the specimen was modeled. The predicted load-displacement curve correlates well with the experimental results (Figure 3.14). The parameter uncertainty has been investigated in a previous work [9]. The deformed geometry prior to final unstable fracture is shown in Figure 3.15 and a small portion of the nugget has not fractured yet. The model prediction with coupled 2-D and 3-D mesh compared well to previous study using a 3-D model [9].

The cohesive peak stress is shown to be 285 MPa for geometries where the necking is limited. However, for thin specimens under large-scale plastic deformation (for example, the Kahn specimens of 2.0 mm, 1.6 mm and 1.0 mm all have same necking ratio of 0.3), the peak stress is calibrated to be 600 MPa. Therefore deep double-notch geometry was introduced to further examine the value of the peak stress (Figures 3.16-3.17). Given the sheet thickness of 2 mm, both notches were machined to be 8mm deep and 2 mm wide (Figure 3.16). The loads were monitored through the load cell and the displacement was measured by an extensometer. The length of fractured surface was measured from experiment to be 3.0 mm (initial length is 4 mm) and the thickness after final fracture was measured to be 1.4 mm near the notch and 1.2 mm at the center of two notches (Figure 3.18). It was found that the FE model with the pair of 13 kJ/m^2 and 450 MPa (four and

half times of the yield stress) gave a good simulation of the necking (Figures 3.18-3.19). There existed some mix-mode fracture in the experiment. In contrast, a mode-I fracture was enforced in the model and there was no slant fracture. The load-displacement curves from experiments were also well modeled and the effect of model uncertainty, ± 3 kJ/m^2 and ± 15 MPa, is also shown in Figures 3.20 and 3.20a. The total work of fracture was calculated from the load-displacement curves to be 2800 N.mm so the fracture toughness was computed to be 2800 / 8 = 350 (kJ/m^2). Again, it is a big number compared to the specific work of separation valued at 13 kJ/m^2.

In summary, the cohesive peak stress was shown to depend on the degree of plastic deformation characterized by the necking ratio: 600 MPa for the necking ratio of 0.3, 450 MPa for the necking ratio of 0.6, and 285 MPa for limited necking. Even though the specific work of separation is assumed a material constant, the fracture toughness scales with thickness at small thickness and plane-stress.

Thickness Effect for Al6082-O

Experimental results on mode-I fracture of Al6082-O thin plates of 1-6 mm are available in publications [5, 11-12]. Material properties include Young's modulus of 70 GPa, Poisson's ratio of 0.34, and the yield strength of 50 MPa. Necking starts at a strain of 17% and the true stress at the onset of necking is 130 MPa. The flow rule is given [5]:

$$\sigma = 202\varepsilon^{0.247} \text{ MPa} \tag{5}$$

The geometry used is the DENT specimen (Figure 3.21). Three different dimensions, 20 mm long between the notches and 1-3 mm thick, were used in this study and labeled as T1, T2, and T3. Only half of the specimen was meshed due to symmetry and a 2-D shell mesh was coupled with 3-D solid mesh (Figure 3.22). There are three operations to prepare the notch of the DENT specimen [13]: machining, saw cut and razor blade cut. The opening width of the initial long notch, obtained by regular machining, was made about 2 mm. Then, a 0.3 mm saw was used to extend the notch by about 1.5-2 mm. Finally the razor blade cut a relatively sharp pre-crack, about 0.05 mm wide over a length of about 1 mm. These geometrical features were comprehended in the models.

The CZM was applied for the first time to simulate the fracture behavior of DENT specimens of Al6082-O. The specific work of separation has been measured at 30 kJ/m^2 in a previous work [11].

To fit the necking ratio of 0.4 measured from experiments, the peak stress was calibrated to be 250 MPa, which is five times of the yield stress (Figure 3.23). The fracture surface is mainly planar as shown in Figure 3.23. There is very little shear slip and the fracture is mostly a mode-I. The fracture profile simulated by the model in a pure mode-I fracture is in agreement with experiment. The model was able to simulate the necking at different thicknesses and the necking ratios were predicted to be 0.40, 0.41 and 0.42 for specimens T1, T2 and T3, respectively (Figure 3.24). Good correlation is also shown in the comparison of stress-displacement curves between the model and the experiment (Figure 3.25). To examine the sensitivity of the cohesive values, the pairs of 24 kJ/m^2 with 240 MPa and 36 kJ/m^2 with 260 MPa were also applied to simulate the stress-displacement curve for a T2 specimen (Figure 3.25a). In addition, based on the stress-displacement curves, the fracture toughness was calculated. The model results compare well with experimental data for specimens T1, T2, and T3 (Figure 3.26). For both the model and the experiment, it is shown that the fracture toughness scales with the specimen thickness.

In summary, the CZM is applicable to Al6082-O DENT specimens and the calibrated cohesive parameters are again shown to be transferable for different thicknesses of same geometry if the degree of plastic deformation is similar. The CZM also seems to confirm that the fracture toughness increases linearly with the increase of thickness.

Effect of Plastic Deformation

Cotterell and Reddel [4] partitioned the contribution of plastic deformation in DENT specimen into two components:

$$\mathrm{w}_f = ltw_e + l^2 tw_p \tag{6}$$

where $\mathbf{w}_f$ is the total work of fracture, w_e is the specific essential work of fracture in the end region and w_p is the volumetric non-essential work in a circular region characterized by the distance l between notches and the specimen thickness t (Figure 3.27). The assumptions include plane-stress and the distance l lower-bounded by $5t$. Hosford and Atkins [14] later analyzed the plastic zone work during necking and related w_e linearly to the thickness t.

To graphically capture the plastic work before and during necking, the plastic region is expanded here to include a square region represented by a volume of $t^2 l$ (Figure 3.28). Therefore the contribution of plastic deformation to the total work of fracture $\mathbf{w}_f$ is expressed as:

$$\mathbf{w}_f = ltw_s + t^2 lw_{pt} + l^2 tw_{pl} \tag{7}$$

where w_s (i.e., Γ_0) is the specific work of separation or the actual work of fracture per unit area, w_{pl} is the volumetric plastic work characterized by the circular region, and w_{pt} is the volumetric plastic work characterized by the square region excluding the overlapping volume with the circular region. When the notch distance l equals the thickness t, the circular region is $\pi l^3/4$ while the square region is l^3, thus results in the net added plastic zone volume as $(4-\pi)\, l^3/4$ (Figure 3.29). Clearly, when l is far larger than thickness t, the circular region includes the square region.

If l is small compared to t, nonetheless, the significance of the square region is twofold. Firstly, plotting $(\mathbf{w}_f / lt)$ (i.e., Γ) versus the notch distance l and extrapolating the plot to a crack length of zero (i.e., $l = 0$) will result in a positive intercept dependent of thickness t because

$$\left(\mathbf{w}_f / lt\right) = (w_s + tw_{pt}) + lw_{pl} \tag{8}$$

This has been shown in experimental results [5]. Secondly, during a steady crack growth, crack length Δa may be thought as l. Since the necking zone is proportional to the square of thickness t, any characterization of fracture toughness that includes the contribution of the necking will scale with the thickness t, as shown in Figures 3.10 and 3.26. Although the specific work of separation is shown to be very small compared to the fracture toughness that includes the necking, it becomes significant if the necking is absent, i.e., in

a plain-strain. It is also shown from equation 8 that first extrapolating the notch distance l to zero and then the thickness t to zero gives the specific work of separation, which is thickness-independent. The extrapolation process has been used to derive the specific work of separation [11]. This justifies that one of the cohesive control parameter, the specific work of separation, may be assumed a material constant.

Conclusions

The CZM has been applied to model mode-I crack growth of Al5754-O Kahn specimens and Al6082-O DENT specimens. It is concluded that, at small thickness under large plastic deformation, the cohesive parameters including the specific work of separation and the peak stress have good transferability if the degree of plastic deformation is similar. Experimentally, analytically, and by the CZM, the fracture toughness is shown to scale with material thickness due to the necking. Even though the specific work of separation is assumed a material constant, the cohesive peak stress depends on the degree of plastic deformation characterized by the necking ratio. For Al5754-O, the peak stress is 600 MPa (six times of the yield stress) for a necking ratio of 0.3, 450 MPa (four and half times of the yield stress) for a necking ratio of 0.6, and 285 MPa (close to three times of the yield stress) for geometries where the necking is limited (i.e., the mode-I fracture of Al5754-O spot-weld nugget). For Al6082-O, the peak stress is 250 MPa (five times of the yield stress) for a necking ratio of 0.4.

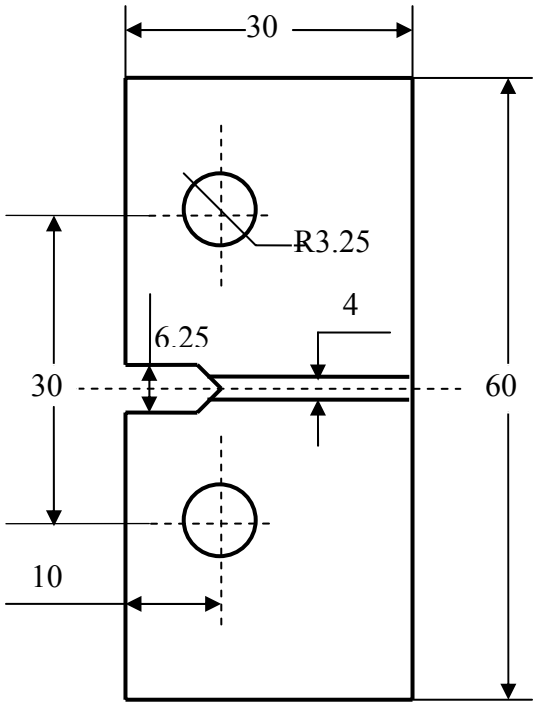

Figure 3.1 Kahn specimen of mixed thickness.
All units are in mm. There is a 4 mm wide groove.

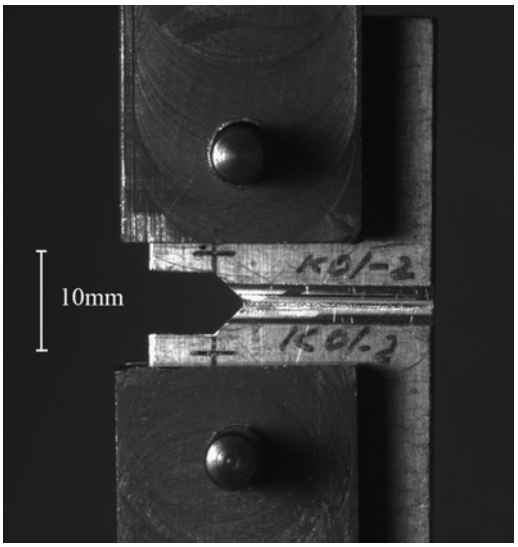

Figure 3.2 Test setup: Kahn specimen of mixed thickness. The 10 mm gage mark was used to measure Notch Tip Opening Displacement (NTOD).

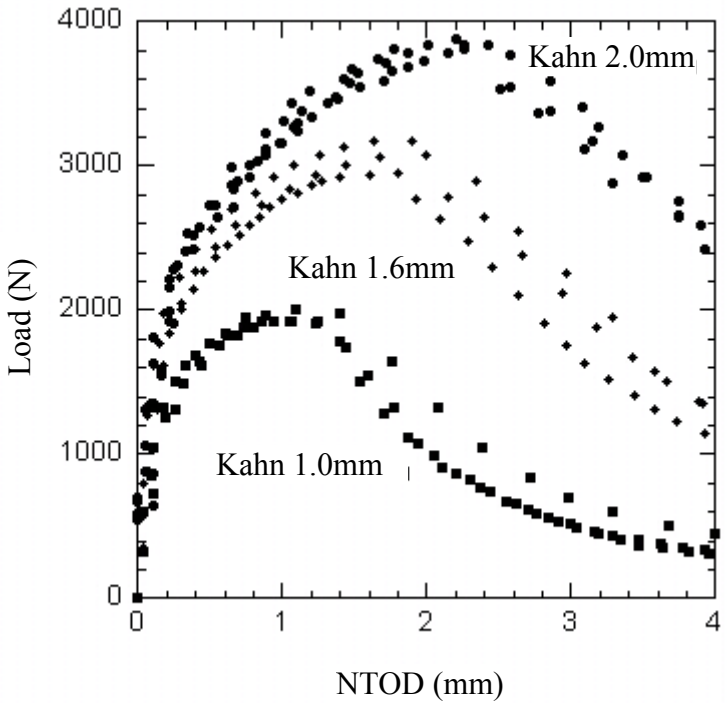

Figure 3.3 Experimental Load-NTOD for Kahn specimens of three thicknesses.

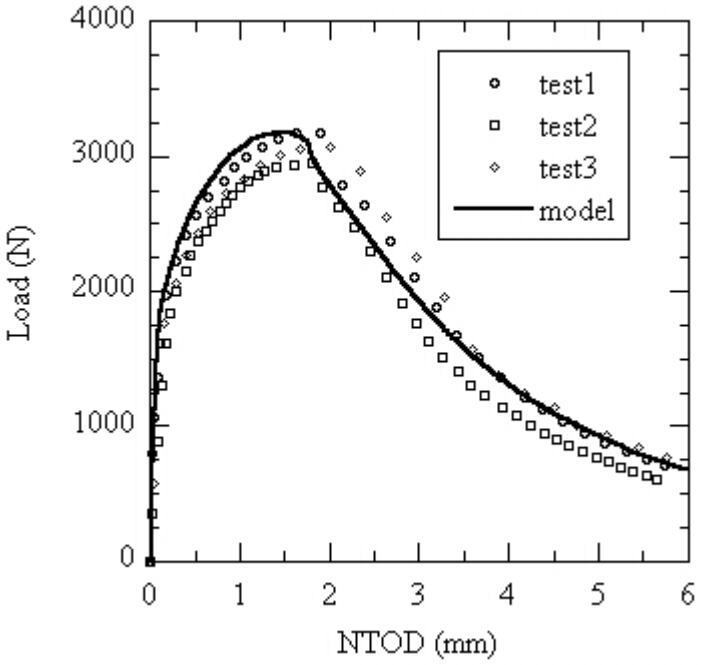

Figure 3.4 Load-NTOD for 1.6 mm Kahn specimen: test versus model.

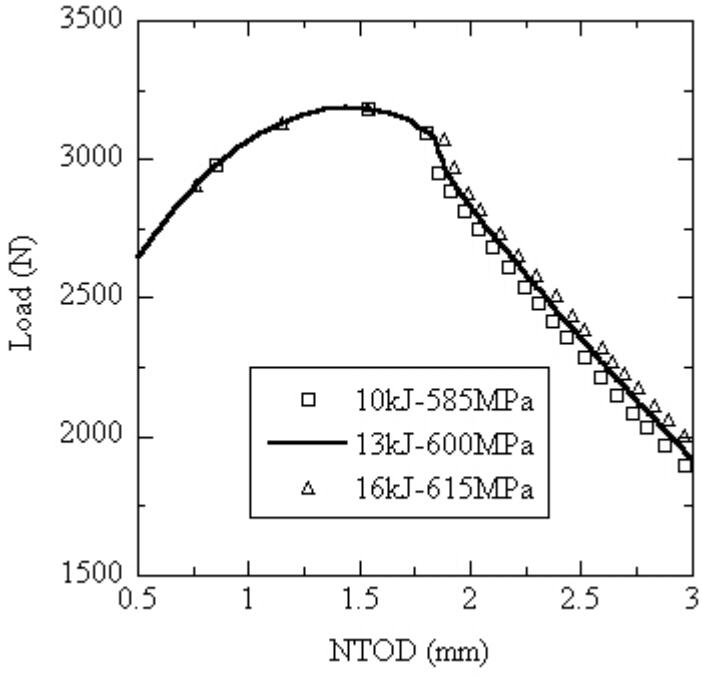

Figure 3.4a Load-NTOD curves for Kahn specimen of 1.6 mm predicted by CZM with different cohesive values of 10kJ/m^2 with 585 MPa, 13kJ/m^2 with 600 MPa and 16kJ/m^2 with 615 MPa. The model uncertainty does not have any effect before crack initiation and the predicted load after crack initiation varies up to ± 3%.

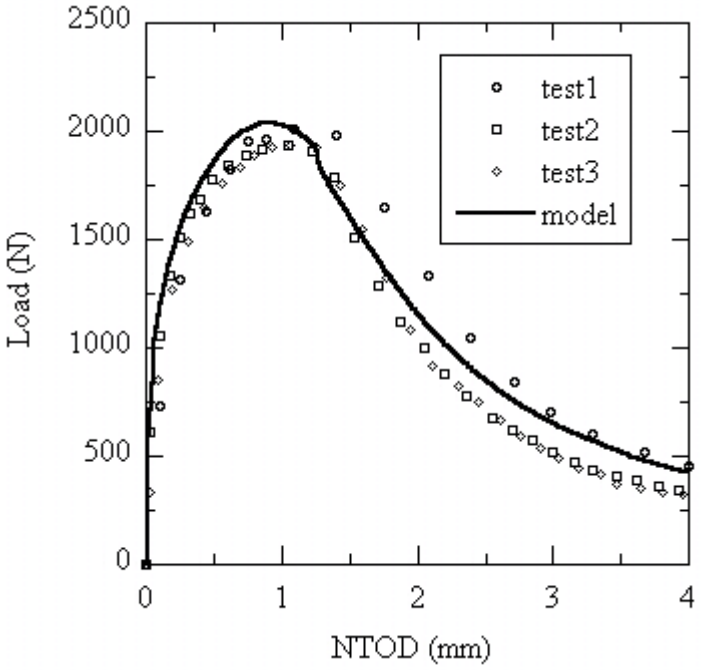

Figure 3.5 Load-NTOD for 1.0 mm Kahn specimen: test versus model.

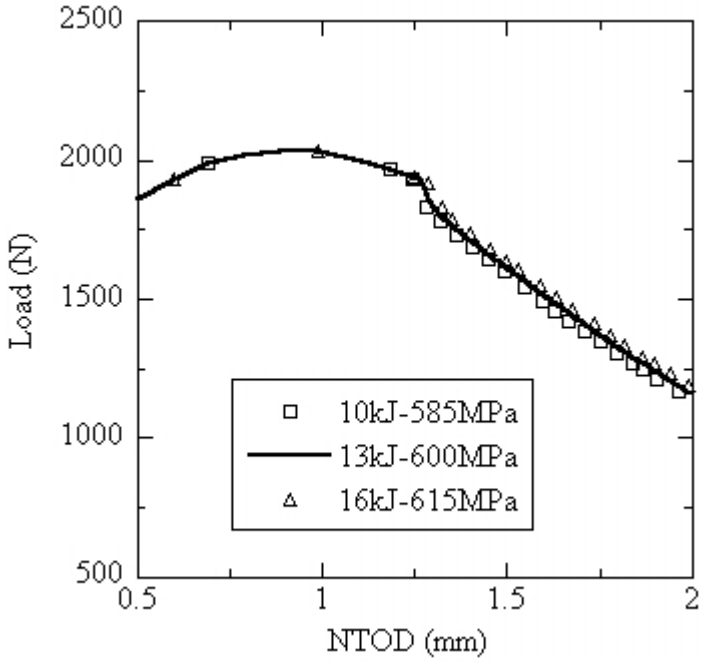

Figure 3.5a Load-NTOD curves for Kahn specimen of 1.0 mm predicted by CZM with different cohesive values of 10 kJ/m^2 with 585 MPa, 13 kJ/m^2 with 600 MPa and 16 kJ/m^2 with 615 MPa. The model uncertainty does not have any effect before crack initiation and the predicted load after crack initiation varies up to ± 3%.

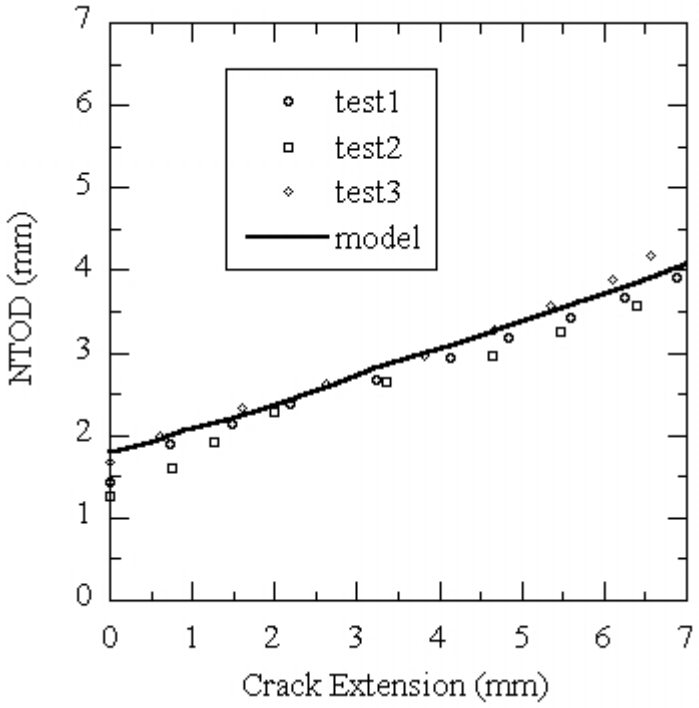

Figure 3.6 NTOD-crack extension for 1.6 mm Kahn specimen: test versus model.

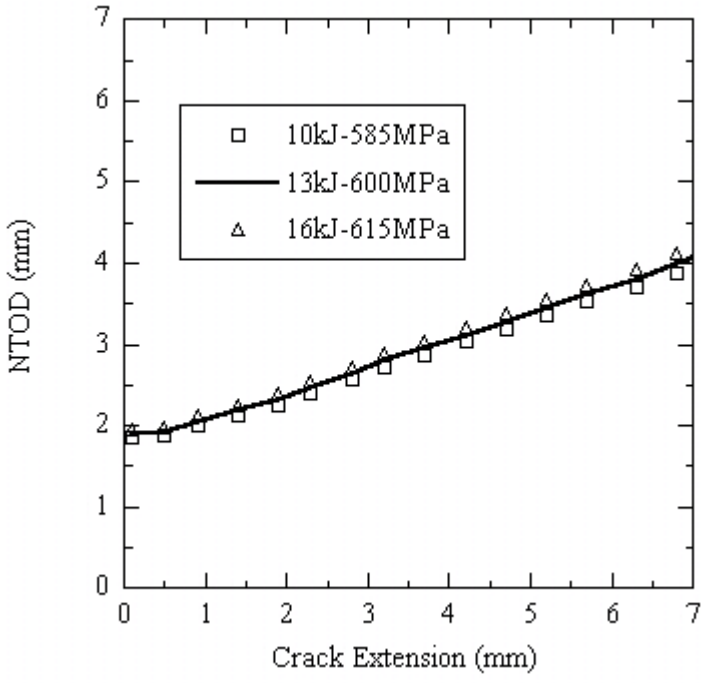

Figure 3.6a NTOD - surface crack extension for Kahn specimen of 1.6 mm predicted by CZM with different cohesive values of 10kJ/m^2 with 585 MPa, 13kJ/m^2 with 600 MPa and 16kJ/m^2 with 615 MPa. The model uncertainty is insignificant.

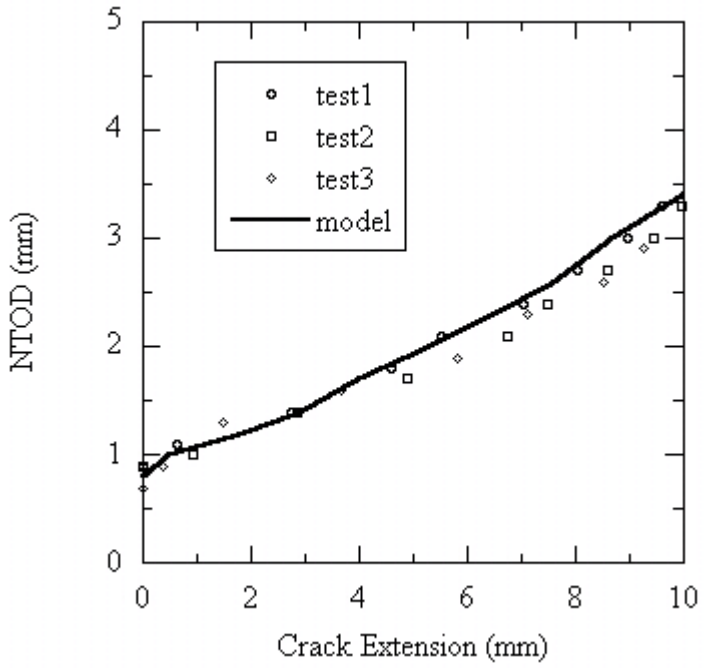

Figure 3.7 NTOD-crack extension for 1.0 mm Kahn specimen: test versus model.

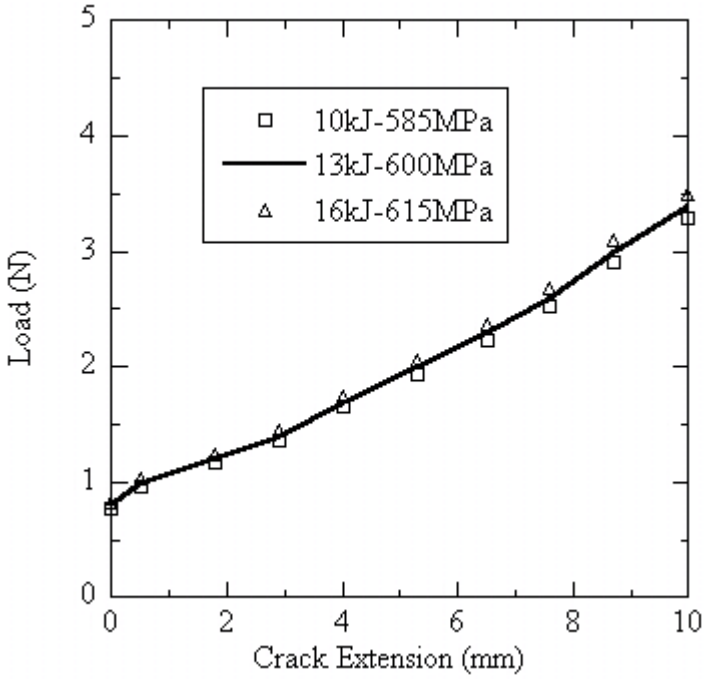

Figure 3.7a NTOD - surface crack extension for Kahn specimen of 1.0 mm predicted by CZM with different cohesive values of 10kJ/m^2 with 585 MPa, 13kJ/m^2 with 600 MPa and 16kJ/m^2 with 615 MPa. The model uncertainty is insignificant.

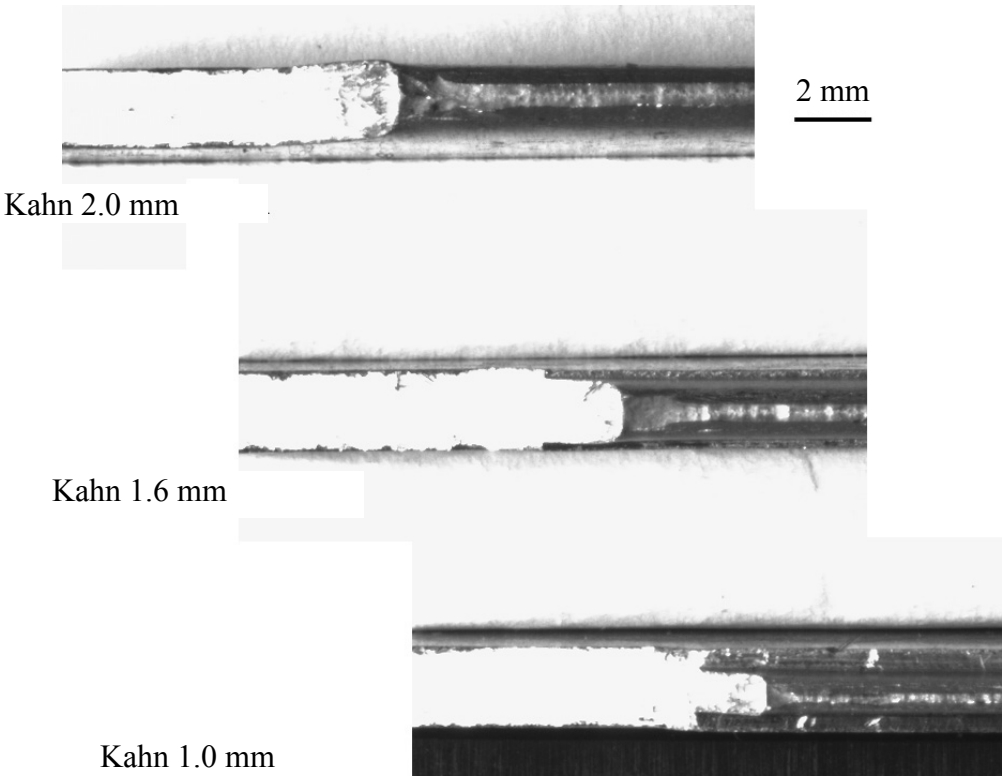

Figure 3.8 Experimental necking profiles for Kahn specimens of three thicknesses.

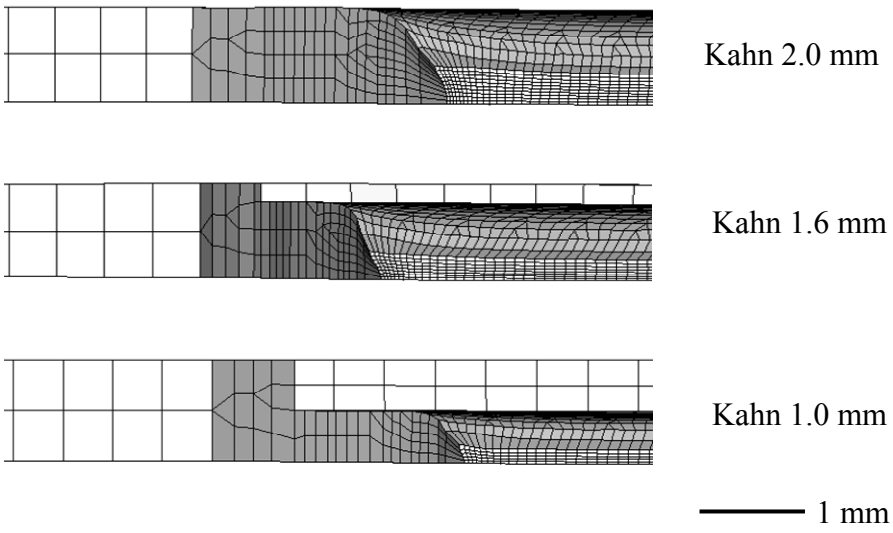

Figure 3.9 Simulated necking profiles for Kahn specimens of three thicknesses.

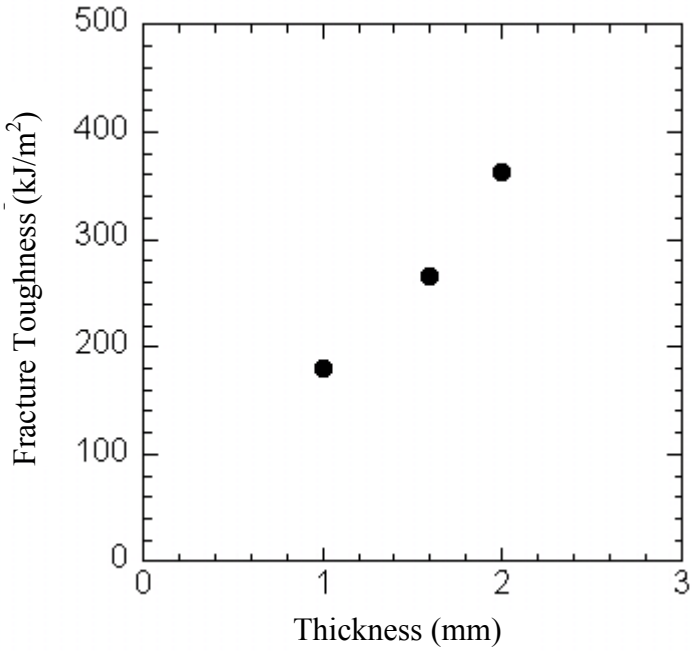

Figure 3.10 Fracture toughness versus material thickness for Kahn specimens. The fracture toughness predicted by the model at steady state includes the contribution from the necking. The specific work of separation of 13 kJ/m^2 is relatively small.

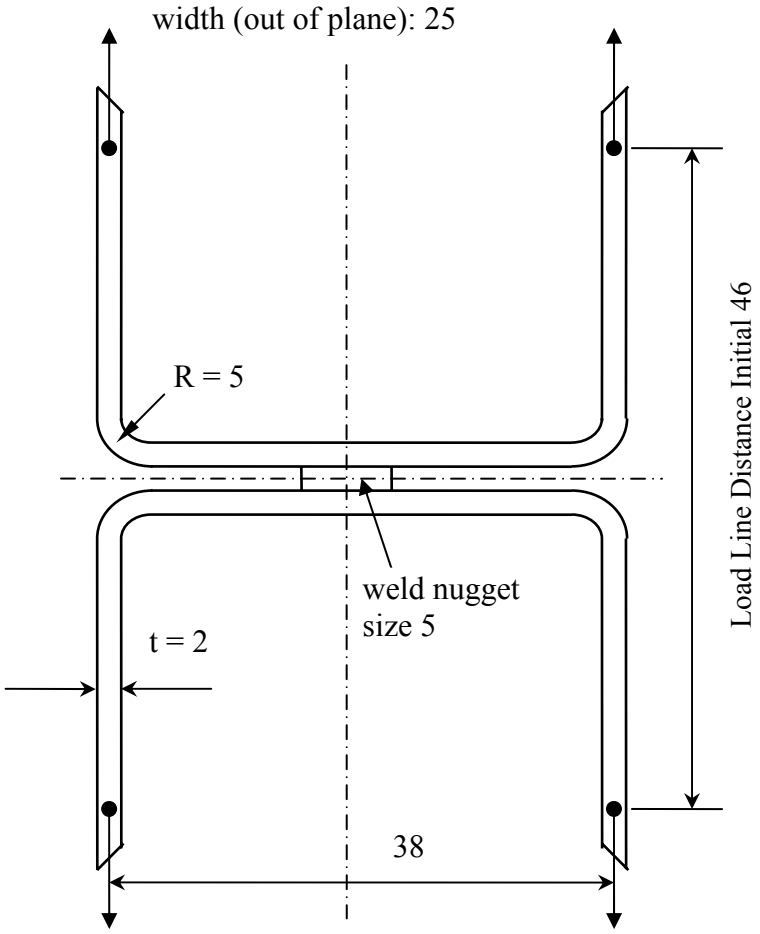

Figure 3.11 Coach-peel spot-weld geometry.
All units are in mm. Picture dimensions are from Cavalli [9].

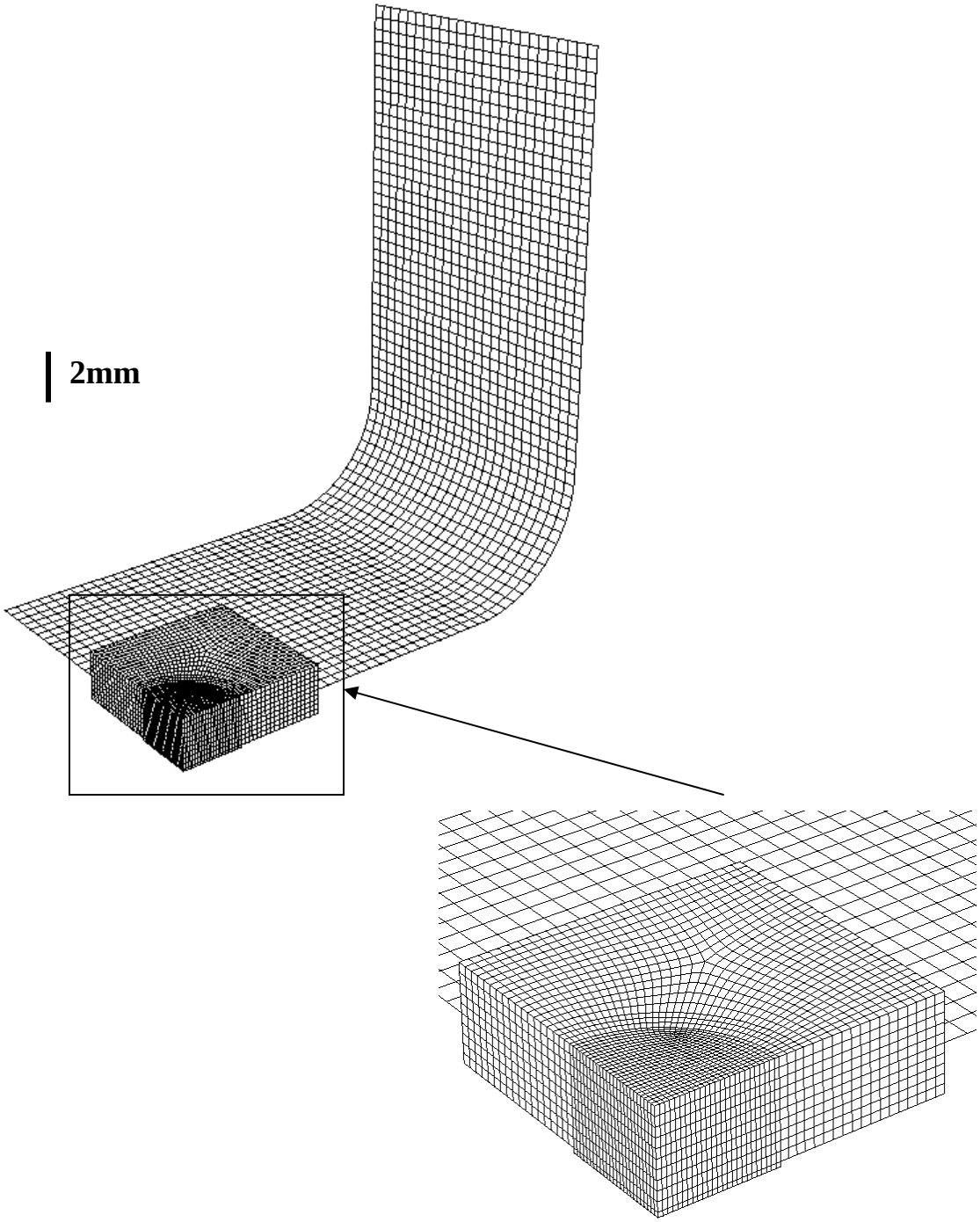

Figure 3.12 Coupled 2-D and 3-D mesh for mode-I coach-peel specimen.
Only one-eighth is modeled due to symmetry. The base material is 2 mm thick. The mesh size is 0.1 mm for cohesive elements.

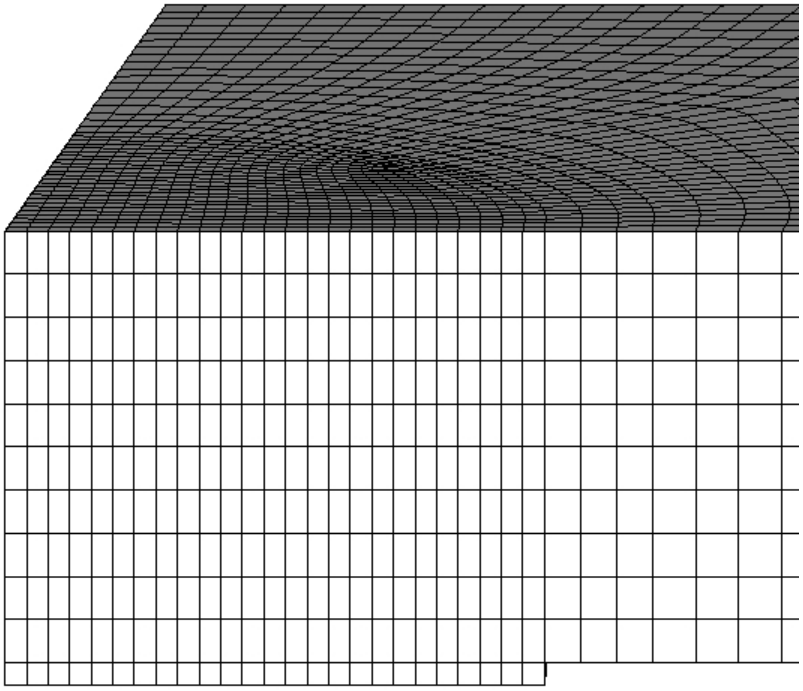

Figure 3.13 Nugget root as a notch.
It is not treated as a sharp crack.

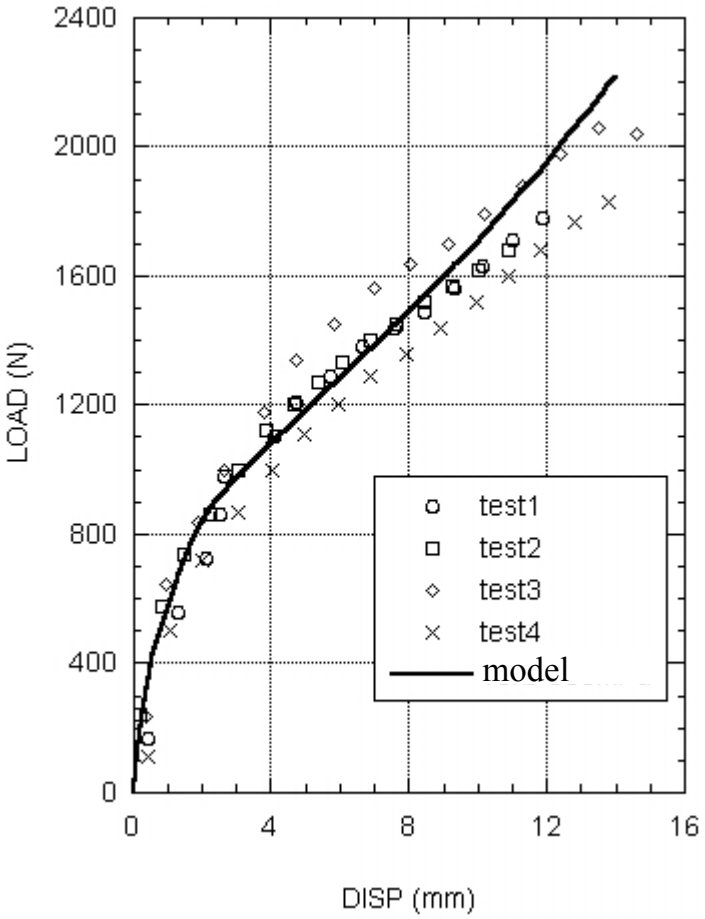

Figure 3.14 Load-displacement curves for mode-I coach-peel: model vs. test. The base material is 2 mm thick and the spot-weld nugget is 5 mm in diameter. The nugget fracture is mode-I. Test data courtesy of Cavalli [9].

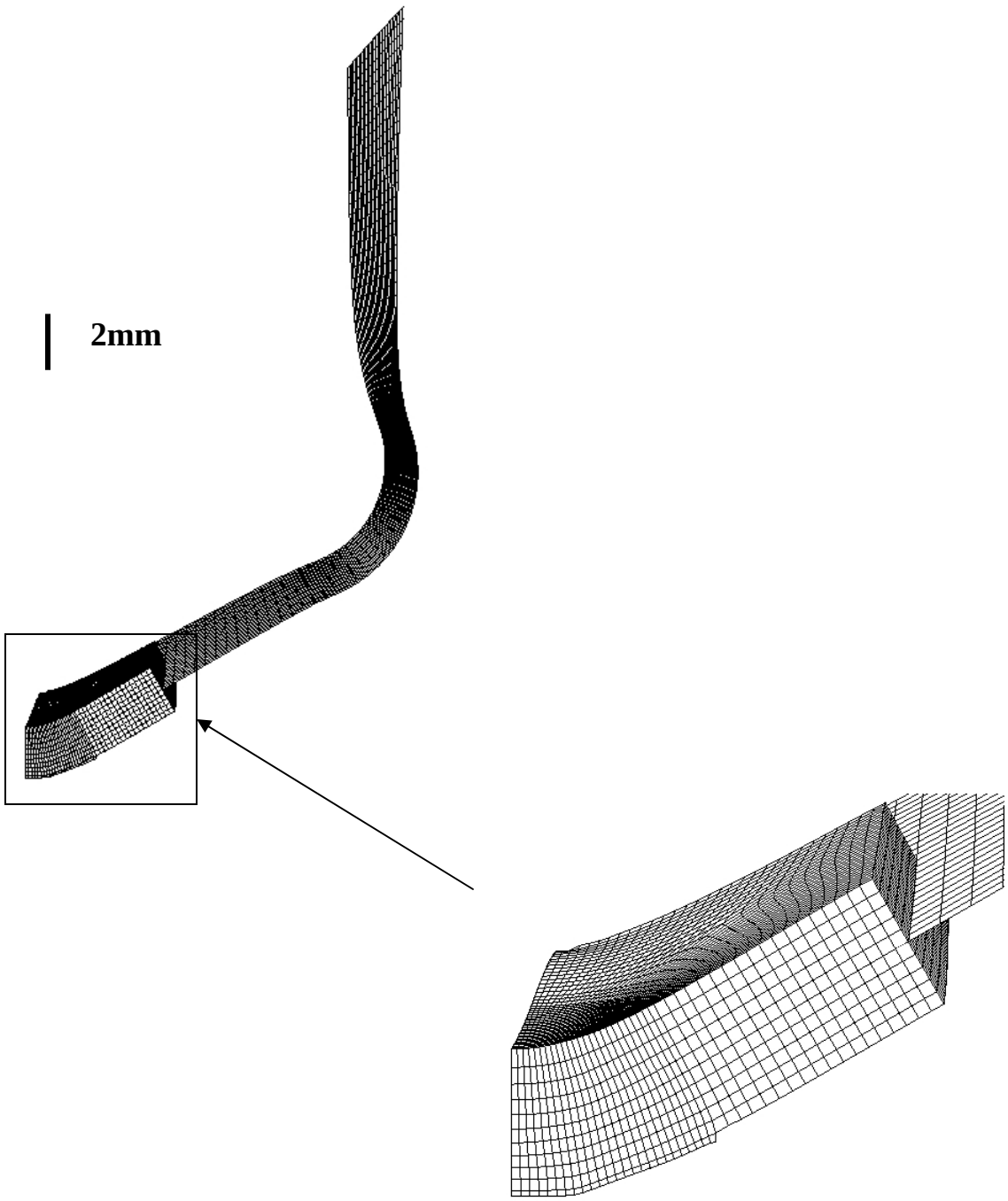

Figure 3.15 Deformed shape prior to final unstable fracture for mode-I coach-peel. The spot-weld nugget fracture is mode-I.

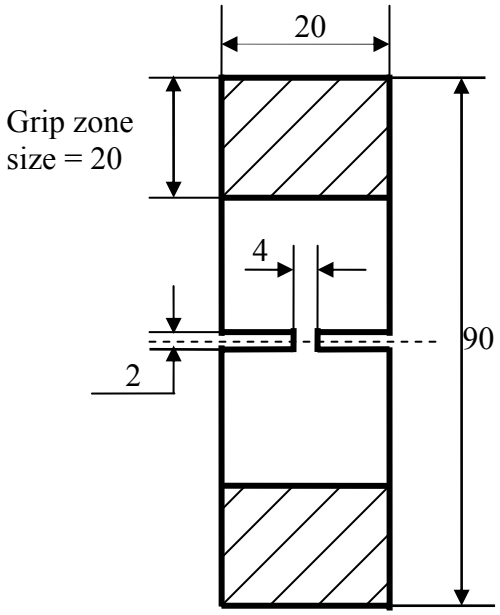

Figure 3.16 Deep double-notch specimen with thickness of 2 (all units in mm).

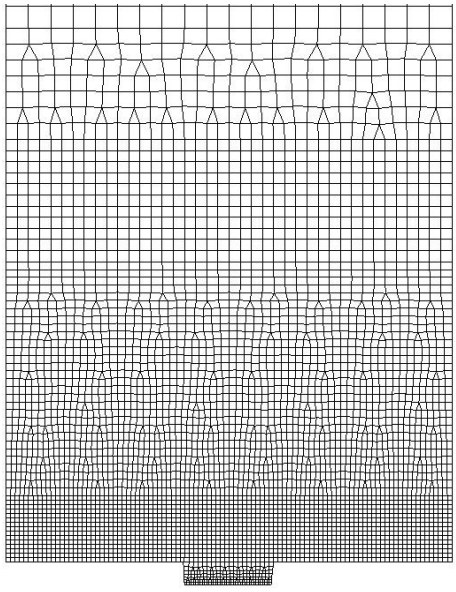

Figure 3.17 Deep double-notch model with cohesive-zone elements of 0.1 mm.

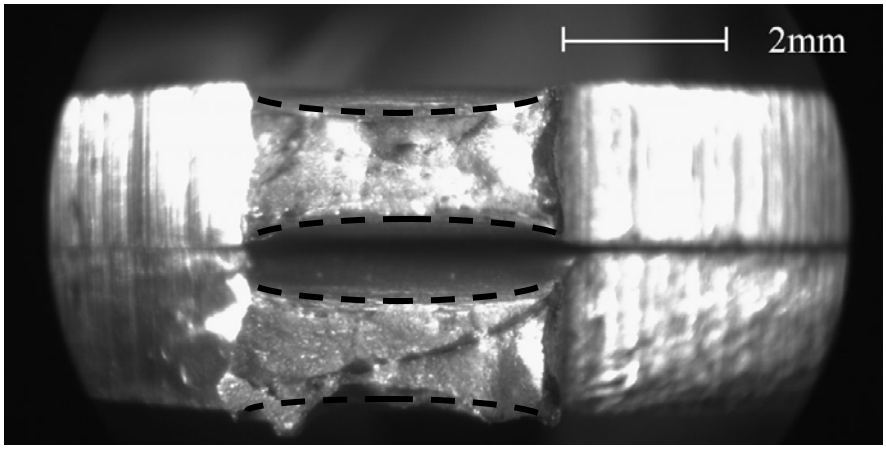

Figure 3.18 Experimental necking profile for deep double-notch specimen. The fractured upper half is paired with lower half. There is some mixed-mode fracture. The doted lines delimit the fracture profile of the ligament.

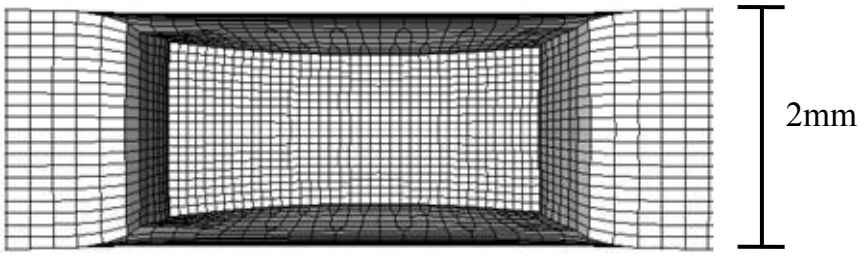

Figure 3.19 Simulated necking profile for deep double-notch specimen.

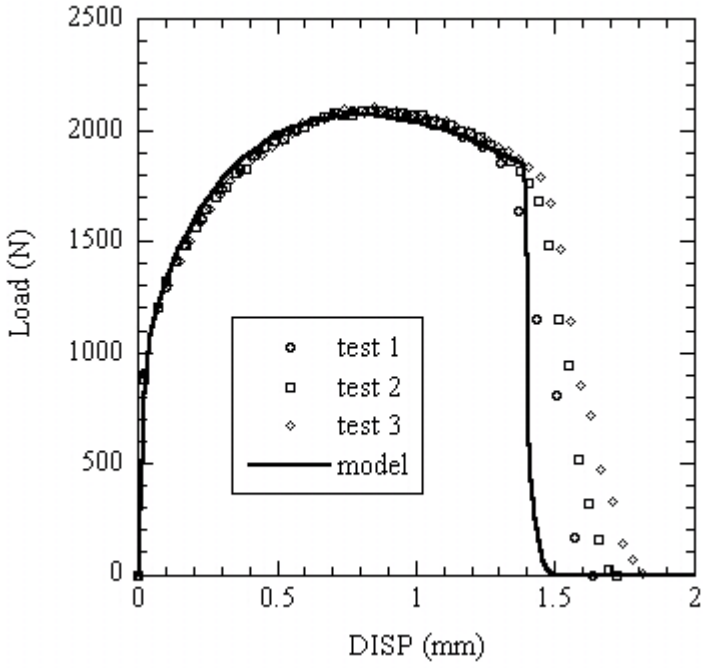

Figure 3.20 Load-displacement for deep double-notch specimen: model versus tests.

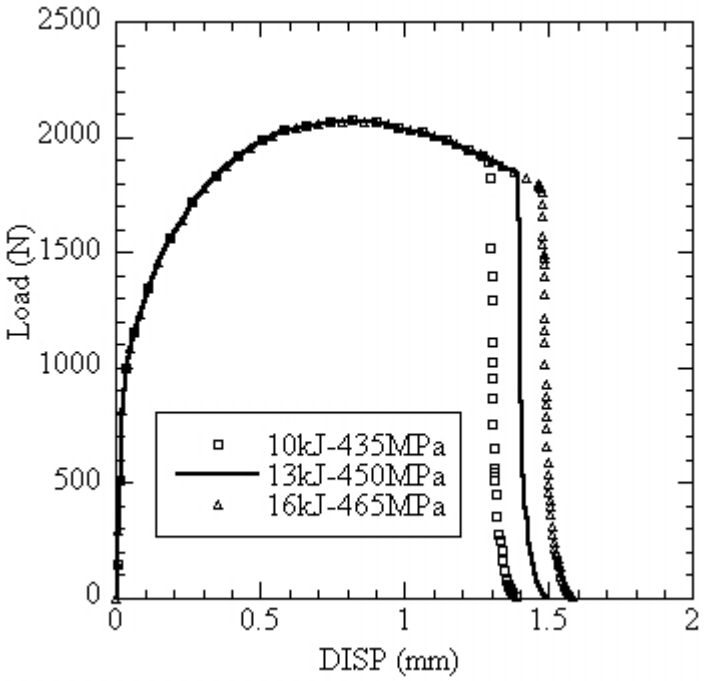

Figure 3.20a Load-DISP curves for double-notch specimen predicted by CZM with different cohesive values of 10kJ/m^2 with 435 MPa, 13kJ/m^2 with 450 MPa and 16kJ/m^2 with 465 MPa. For same load during crack growth, the model uncertainty is ± 0.1 mm.

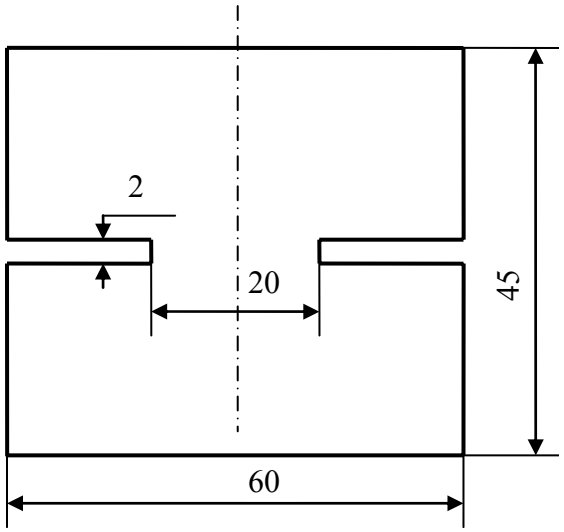

Figure 3.21 DENT specimen.
All units are in mm. The gauge length is 45 mm.

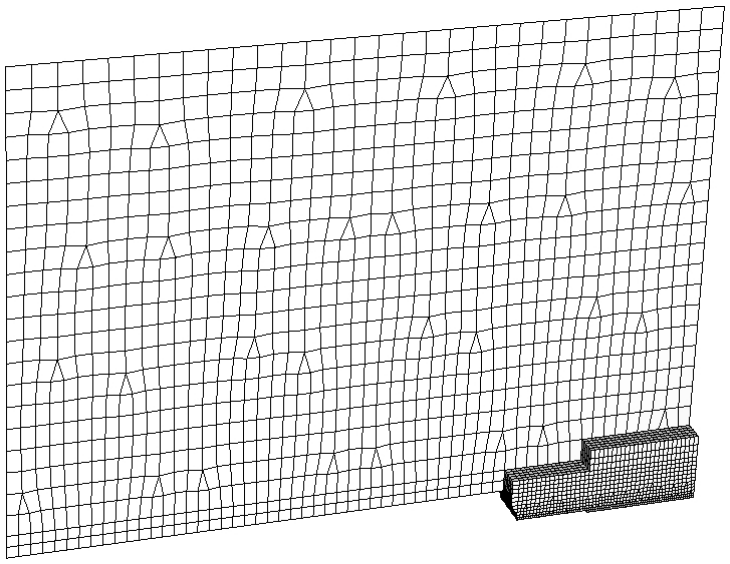

Figure 3.22 Coupled 2-D and 3-D mesh for DENT specimen.

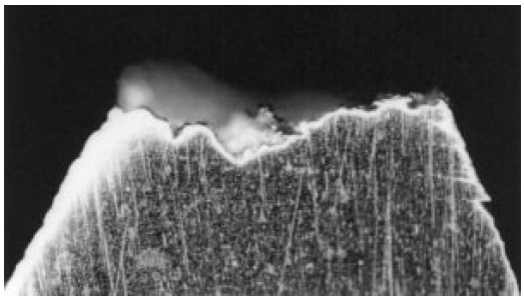

(a) Fracture profile from test. Courtesy of Pardoen etc. [5].

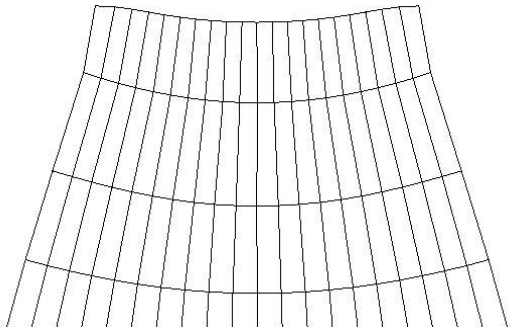

(b) Fracture profile from model simulation.

Figure 3.23 Fracture profiles: (a) test versus (b) model.

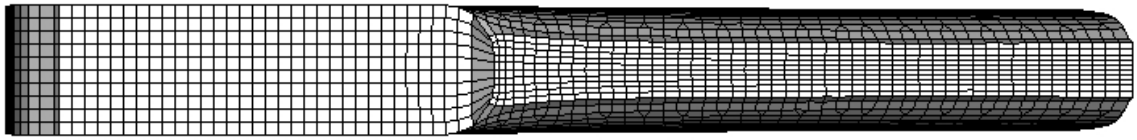

(a) 1 mm DENT

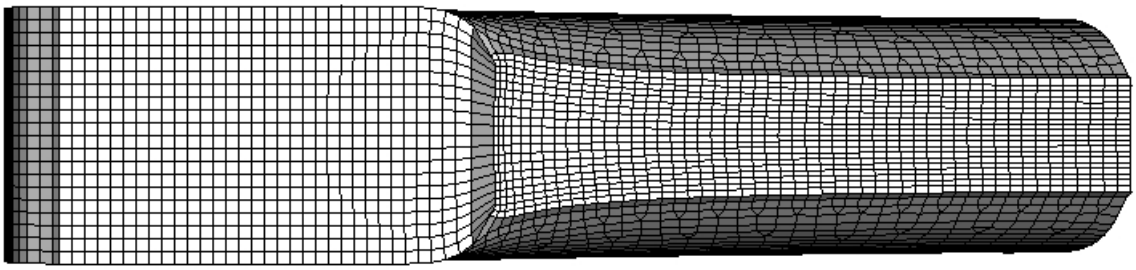

(b) 2 mm DENT

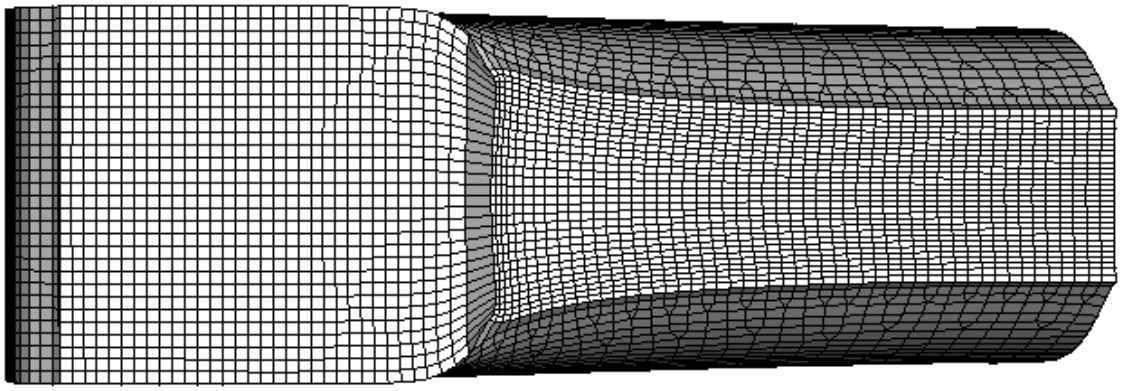

(c) 3 mm DENT

Figure 3.24 Simulated necking profiles for DENT specimens of three thicknesses.

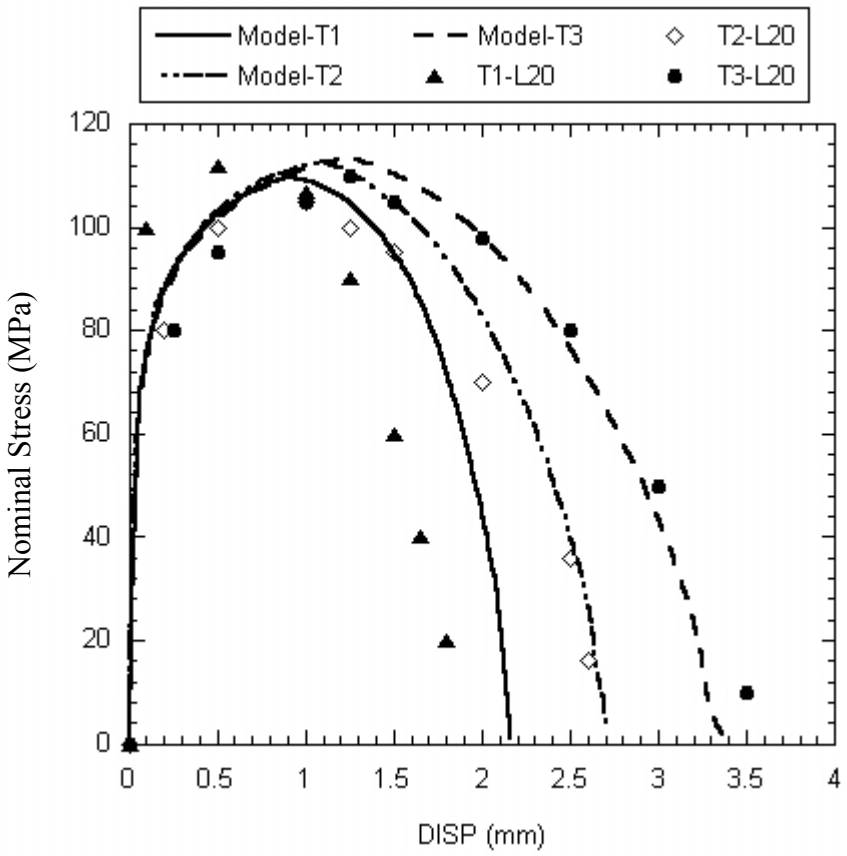

Figure 3.25 Stress-Displacement curves for DENT specimens: test versus model. Test data are from Cotterell etc. [12].

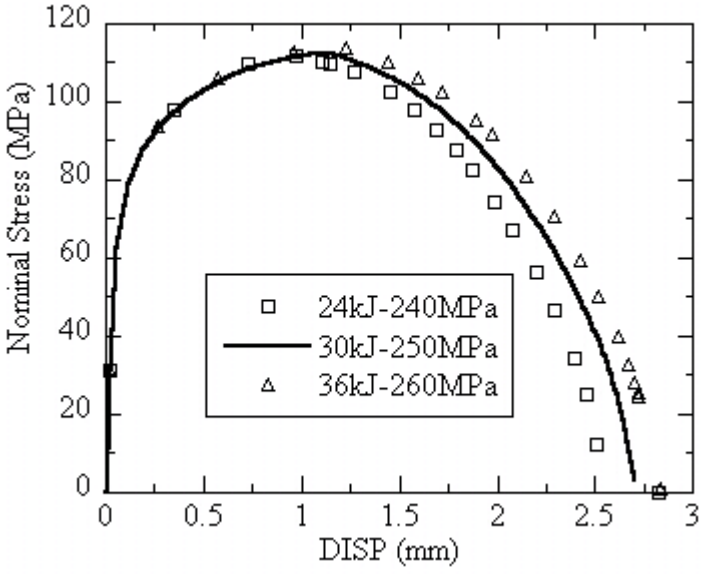

Figure 3.25a Stress-Displacement curves for T2 specimen predicted by CZM with different cohesive values of 24kJ/m^2 with 240 MPa, 30kJ/m^2 with 250 MPa and 36kJ/m^2 with 260 MPa. For same load during crack growth, the model uncertainty is ± 0.1 mm.

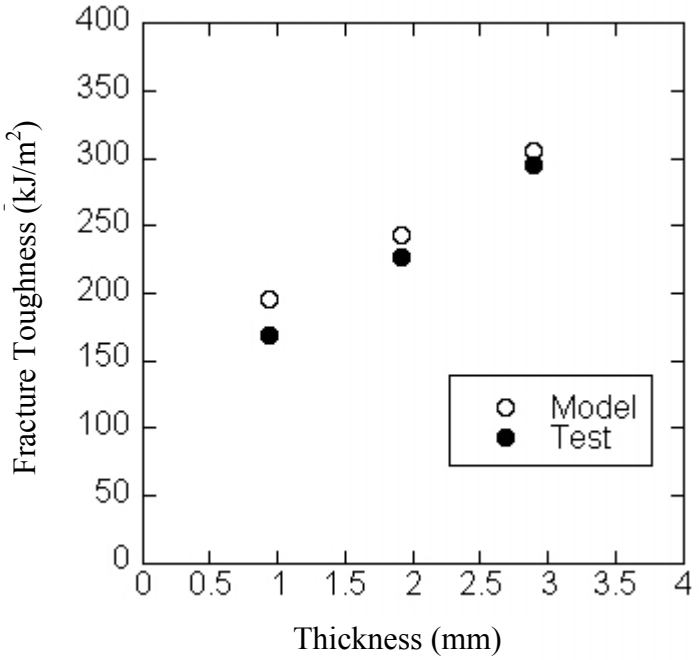

Figure 3.26 Fracture toughness versus thickness for DENT specimens. Experimental results are compared to model predictions using cohesive values of 30 kJ/m^2 and 250 MPa. The fracture toughness included the necking contribution. The specific work of separation of 30 kJ/m^2 is relatively small. Test data are from Pardoen etc. [5].

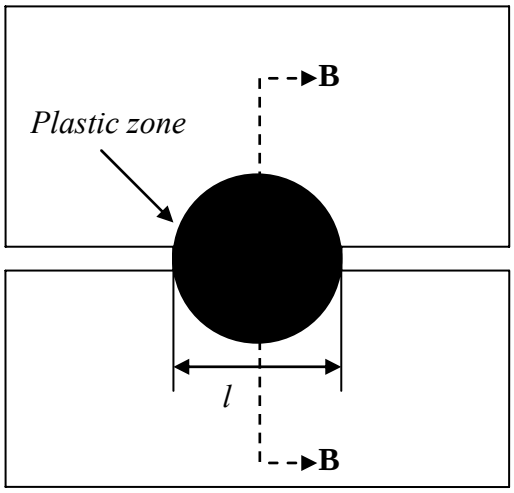

Figure 3.27 Circular plastic zone by ligament size *l* in DENT specimen.

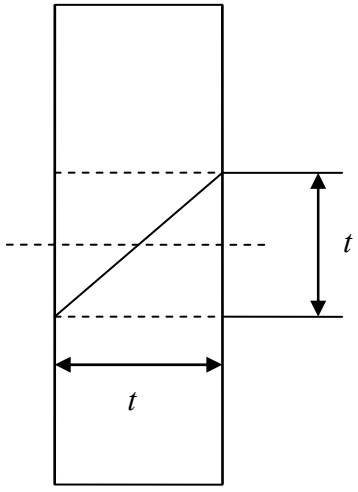

Section B-B

Figure 3.28 Square plastic region by thickness *t* in DENT specimen.

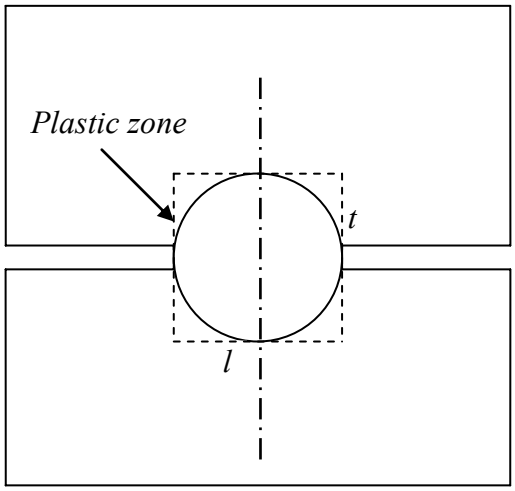

Figure 3.29 Plastic zones described by ligament *l* and thickness *t* when *l* = *t*.

References

1. J. I. Bluhm, "A model for the effect of thickness on fracture toughness", ASTM Proceedings, **61**, 1324-1331 (1961).

2. J.F. Knott, *Fundamentals of Fracture Mechanics*, Butterworth, London (1973).

3. J. M. Barsom S.T. Rolfe, *Fracture and Fatigue Control in Structures: Applications of Fracture Mechanics*, Third Edition, Butterworth-Heinemann, Woburn, MA (1999).

4. B. Cotterell, J. K. Reddel, "The essential work of plane stress ductile fracture", *International Journal of Fracture*, **13**, 267-277 (1977).

5. T. Pardoen, Y. Marchal, F. Delannay, "Thickness dependence of cracking resistance in thin aluminum plates", *Journal of the Mechanics and Physics of Solids*, **47**, 2093-2123 (1999).

6. G. T. Hahn, A. R. Rosenfield**, "**Local yielding and extension of a crack under plane stress", Acta Metallurgica, **13**, 293-306 (1965).

7. G. I. Barenblatt, "Equilibrium cracks formed during brittle fracture", *Journal of Applied Mathematics and Mechanics*, **23**, 1273-1282 (1959).

8. D. S. Dugdale, "Yielding of steel sheets containing slits", *Journal of the Mechanics and Physics of Solids*, **8**, 100–104 (1960).

9. M. N. Cavalli, *Cohesive Zone Modeling of Structural Joint Failure*, Ph.D.Thesis, University of Michigan, 2003.

10. S. D. Sheppard and N. Pan, "A Look at Fatigue in Resistance Spot Welds—Notch or Crack? ", SAE 2001-01-0433 (2001).

11. T. Pardoen, Y. Marchal, F. Delannay, "Essential work of fracture compared to fracture mechanics-towards a thickness independent plane stress toughness", *Engineering Fracture Mechanics*, **69**, 617-631 (2002).

12. B. Cotterell, T. Pardoen, A. G. Atkins, "Measuring toughness and the cohesive stress-displacement relationship by the essential work of fracture concept", *Engineering Fracture Mechanics*, **72**, 827-848 (2005).

13. Private Communication with T. Pardoen, 2006.

14. W. F. Hosford and A. G. Atkins, "On Fracture Toughness in Tearing of Sheet Metal", *Journal of Material Shaping Technology*, **8**, 107-110 (1990).

Chapter 4

Mode-III Fracture of Al5754-O Sheet

Introduction

This chapter aims to investigate mode-III fracture of Al5754-O sheet, in addition to mode-I work done in chapters 2-3. The trouser specimen was first developed by Rivlin and Thomas [1] to determine the mode-III fracture toughness for sheet rubber (Figure 4.1). Where deformation is elastic and reversed upon unloading, the fracture toughness, Γ, is estimated [2]:

$$\Gamma = \frac{2P}{t} \tag{1}$$

where P is the tearing force and t is the thickness of trouser specimen. In the presence of plastic deformation, Mai and Cotterell [3] found there is a linear relationship between the tearing force per unit thickness and the specimen leg width, assuming no contribution from the elasticity and the bend radius is constant. The fracture toughness could then be obtained by extrapolating the specimen leg width to zero. Later Muscat-Fenech and Atkins [4] re-examined the assumptions and concluded the relationship is nonlinear,

$$\frac{P}{t} = \frac{1}{2}\Gamma + B\left\{C_1 \frac{\sigma_y^3 \rho}{\mathrm{E}^2 t} - C_2 \frac{\sigma_y^2}{\mathrm{E}} + C_3 \frac{\sigma_y}{\rho} t + C_4 \frac{\mathrm{E}t^2}{\rho^2}\right\} \tag{2}$$

where B is the trouser leg width, σ_y is the yield strength, ρ is the bend radius that increases with the leg width, C_1, C_2, C_3, and C_4 are coefficients related to Young's modulus E and the strain hardening modulus E_p as follows:

$$C_1 = \frac{1}{3}\left[10 - 14\left(\frac{\mathrm{E}_p}{\mathrm{E}}\right) + 6\left(\frac{\mathrm{E}_p}{\mathrm{E}}\right)^2 - \left(\frac{\mathrm{E}_p}{\mathrm{E}}\right)^3\right] \tag{3}$$

$$C_2 = \frac{1}{2}\left[5 - 9\left(\frac{E_p}{E}\right) + 5\left(\frac{E_p}{E}\right)^2 - \left(\frac{E_p}{E}\right)^3\right] \quad (4)$$

$$C_3 = \frac{1}{4}\left[2 - 5\left(\frac{E_p}{E}\right) + 4\left(\frac{E_p}{E}\right)^2 - \left(\frac{E_p}{E}\right)^3\right] \quad (5)$$

$$C_4 = \frac{1}{24}\left(\frac{E_p}{E}\right)\left[2 - 3\left(\frac{E_p}{E}\right) + \left(\frac{E_p}{E}\right)^2\right] \quad (6)$$

The CZM, first proposed by G. I. Barrenblatt [5] and D. S. Dugdale [6], will be represented by the traction-separation law [7] shown in Figure 1.3 and applied to simulate the mode-III fracture of Al5754-O sheet. The first step will be to determine the mode-III cohesive values for Al5754-O sheets using the trouser specimen. Then the calibrated model will be used to predict the crack growth of trouser specimens at different leg width, in order to examine whether the control parameters of the CZM including the cohesive peak stress and the specific work of separation are geometry-dependent. Finally, the CZM will be applied to model the nugget pull-out of Al5754-O spot weld, which is a mixed-mode fracture of mode-I and mode-III.

Determination of Cohesive Parameters

The true stress-strain relationship has been determined in chapter 2 as,

$$\sigma = 393\varepsilon^{0.2} \text{ MPa} \quad (7)$$

Three trouser specimens, 2 mm thick, with leg width B = 8 mm (Figure 4.1) were prepared from Al5754-O sheet of 2mm thick. The preparing steps are: a flat specimen was first machined to an in-plane dimension of 100 mm x 16 mm; a slot 0.05 inch wide was cut to split the flat specimen into two legs, leaving an over-hang of L = 35 mm; at last, to reduce the total displacement and reach the steady crack propagation sooner, the two legs were pre-bent 90-degree in a fixture, resulting in a gauge distance of H = 50 mm. In addition, to help achieve a smoother crack initiation, the initial crack front was sawed to have a ramp (Figure 4.2).

The trouser tests were conducted in a screw-driven tensile test machine with a crosshead speed of 2 mm/minute. The loads and the crosshead displacements were monitored through a machine-equipped load cell and a gage, respectively. The experimental load-displacement curves exhibit a plateau that shows a steady crack growth (Figure 4.3). The portion before the plateau indicates the time for the crack to reach steady-state growth and it does not affect the magnitude of the plateau. The model will not try to match the ramp up and the plateau will be the focus of our study.

The specific work of separation was first estimated. The tearing force measured from Figure 4.3 is approximately 730 N and the bend radius was measured from experiment to be 8 mm. With the yield strength of 100 MPa and the true stress of 285 MPa at a true strain of 0.2, the strain hardening modulus is approximated to be (285 – 100) / 0.2 = 925 MPa. Then coefficients C_1, C_2, C_3, and C_4 were computed from equations 3-6 as 3.2711, 2.4401, 0.4834, and 0.0011, respectively. Then the fracture toughness, Γ, was calculated from

$$\Gamma = 2\left[\frac{P}{t} - B\left(C_1\frac{\sigma_y^3\rho}{\mathrm{E}^2 t} - C_2\frac{\sigma_y^2}{\mathrm{E}} + C_3\frac{\sigma_y}{\rho}t + C_4\frac{\mathrm{E}t^2}{\rho^2}\right)\right] \tag{8}$$

$$= 2\left[\frac{730}{2} - 8\left(3.2711\frac{100^3(8)}{69000^2(2)} - 2.4401\frac{100^2}{69000} + 0.4834\frac{100}{8}2 + 0.0011\frac{69000(2)^2}{8^2}\right)\right]$$

$$= 435 \text{ kJ/m}^2$$

Both the specific work of separation, w_e (i.e., Γ_0), and the work of shear zone plastic deformation per unit area, w_{ps} (i.e., Γ_p),, contribute to the fracture toughness and the ratio of their contributions is estimated [3],

$$\frac{w_{ps}}{w_e} = \frac{4\gamma}{(1+n)}\left(\frac{2s}{t}\right) \tag{9}$$

where γ is the shear strain, *2s* is the size of the shear zone, *t* is the current thickness and *n* is the strain hardening exponent (n = 0.2 for Al5754-O). Shown in Figure 4.4, the shear zone length s = 4 mm, the shear strain γ = 0.5, and the necked thickness t = 1.3mm. Therefore,

$$\frac{w_{ps}}{w_e} = \frac{4\gamma}{(1+n)}\left(\frac{2s}{t}\right) = \frac{4(0.5)}{1.2}\left(\frac{8}{1.3}\right) = 10.3 \qquad (10)$$

The specific work of separation was then computed as 435 / (1 + 10.3) = 38 kJ/m^2.

Because the cohesive strength for mode-I is lower-bounded by the true stress of 285 MPa at the onset of necking, the lower-bound cohesive strength for mode-III is calculated as 285 / √3 = 165 MPa, based on von-Mises yield theory. The ratio between the mode-I and mode-III cohesive strength is consistent with published data for 5454 aluminum that give a range of shear strengths of 59-64% of the tensile strength for various amounts of strain hardening [8-9]. To further determine the cohesive peak stress, a FE model for the trouser specimen was constructed (Figure 4.5). To reduce the size of the model, the far-side 2-D mesh was coupled with the 3-D mesh of cohesive elements and surrounding continuum. The ramp in the initial crack front was also modeled. It was found that the CZM, with a specific work of separation of 38 kJ/m^2 and a peak stress of 280 MPa, simulated the force level of 730 N (Figure 4.6). Results from the full 3-D model showed little difference. To examine the sensitivity of the identified cohesive values, ±8 kJ/m^2 for the specific work of separation and ±10 MPa for the peak stress were applied in the model and the effect is shown in Figure 4.6b.

The fractured surface simulated by the model compares well to the experiment (Figure 4.7). The thickness after final tearing was measured at 1.2 mm from the model and 1.3 mm from the experiment. A couple of assumptions in the model may have made the difference. Firstly, the model assumes a pure mode-III fracture. In the experiments some mode-I may exist. Secondly, the fixtures are assumed to be rigid in the model. However, during the test, the trouser specimen legs moved slightly toward each other because the fixtures have some compliance. This led to some bulging effect due to compression.

Geometry Effect on Peak Stress

Are the calibrated mode-III cohesive values geometry-dependent? Because the trouser test tears through the specimen thickness, changing the specimen thickness does not

really give a distinguishing geometry if the leg width remains the same. Therefore, three trouser specimens were prepared from 2 mm plate to have L = 60 mm and B = 14 mm (Figure 4.1). And the rest of the geometrical dimensions remain the same as those of 8 mm trouser specimens. The three trouser specimens with leg width of 14 mm were tested in a screw-driven tensile test machine with a crosshead speed of 2 mm/minute. The load-displacement curves from experiment are shown with a force plateau of 820 N in Figure 4.8. The bend radius was measured from the test to be 11 mm. The section profile of the shear zone is shown in Figure 4.9. The thickness after final tearing was measured to be 1.5 mm compared to 1.3 mm for leg width 8 mm, shown in Figure 4.10.

The FE model for the specimen with leg width 14 mm was constructed by extending the 2-D mesh to include additional continuum material while keeping the 3-D mesh (Figure 4.11). However, the model with cohesive values of 38 kJ/m^2 and 280 MPa predicted the force plateau at 890 N compared to 820 N measured from the experiment. And the thickness after final tearing was predicted to be 1.2 mm compared to 1.5 mm from the experiment. To further examine the issue of over prediction, a trouser specimen with leg width of 25 mm was examined. Since the bending radius was measured to be 8 mm and 11 mm for leg widths of 8 mm and 14 mm, respectively, for a leg width of 25 mm it was estimated to be 16.5 mm using a linear extrapolation [4]. Then according to equation 2, the force plateau was computed to be 800 N. However, with cohesive values of 38 kJ/m^2 and 280 MPa, the FE model for a leg width of 25 mm predicted a force of 1050 N.

What caused the FE model with the CZM to over predict the force? Jin and Sun studied the stress distributions ahead of crack tip with and without the CZM for a mode-III crack [10]. They concluded that under small-scale yielding the distributions were significantly different if the peak stress for the CZM is less than two times the yield stress. This implies that the peak stress should be greater than 2.5 times yield stress for medium and large scale yielding so that the stress distribution will not be altered significantly with the CZM. Since different scales of yielding are observed in the trouser tests of different leg width, the peak stress for the CZM needs to be recalibrated. For the trouser leg width of 14 mm, the FE model with cohesive values of 38 kJ/m^2 and 250 MPa simulated the force

plateau of 820 N (Figure 4.12). The necked thickness of 1.5 mm and the bending radius of 11 mm were simulated by the FE model as well. The effect of model uncertainty is insignificant (Figure 4.12b). Then for the trouser leg width of 25 mm, the CZM with cohesive values of 38 kJ/m^2 and 180 MPa modeled the analytical force plateau of 800 N and the analytical bending radius of 16.5 mm. The leg width of the trouser specimen determines the degree of plastic deformation and therefore the cohesive peak stress. In conclusion, the cohesive peak stress is found to be geometry-dependent when the specific work of separation for mode-III fracture is assumed a material constant.

Mixed-mode Fracture of Nugget Pull-out

Unlike the mode-I fracture of a spot-weld nugget, the nugget pull-out is a mixed mode-I and mode-III fracture. It is represented by [11],

$$\left(\frac{\gamma_I}{\Gamma_I}\right)^2 + \left(\frac{\gamma_{II}}{\Gamma_{II}}\right)^2 + \left(\frac{\gamma_{III}}{\Gamma_{III}}\right)^2 = 1 \qquad (11)$$

where γ_I, γ_{II}, and γ_{III} are mode-I, mode-II and mode-III separation work per unit area consumed in a cohesive element, Γ_I, Γ_{II}, and Γ_{III} represent the material's characteristic work of separation per unit area for mode-I, mode-II and mode-III, respectively. For Al5754-O, Γ_I = 13 kJ/m^2, Γ_{III} = 38 kJ/m^2. The coach-peel specimen of 1mm thick with a 5 mm nugget was used (Figure 3.11). Only one eighth of the geometry was modeled due to symmetry (Figure 4.13). Once again the 2-D mesh was coupled with 3-D mesh to reduce the size of the model and the computation time.

The pulling force on the coach-peel specimen (Figure 4.13) causes bending moment near the nugget and the bending moment limits necking through specimen thickness. Also the size of nugget (5 mm in diameter) is small compared to the width of the specimen (25 mm) and the distance between the legs (38 mm) (Figure 3.11). Additionally the thickness of the nugget (2 mm) is twice the thickness of the specimen (1 mm). Considering all these geometrical constraints, it is concluded that the necking is unlikely to develop around the nugget. The lower-bound cohesive peak stresses of 285 MPa for mode-I and 165 MPa for mode-III were then applied and the FE model with the CZM gave a good

prediction compared to test results (Figure 4.14). Please refer to a previous work for the study of parameter uncertainty [12]. During nugget pull-out, the crack propagates around the perimeter of the nugget (Figure 4.15). At the initial stage of the crack propagation, the mode-I fracture dominates. During crack growth, the mode-III contribution increases. Despite the geometry symmetry, the nugget pull-out can not always propagate in a manner assumed here. Meshing one eighth of the geometry implies that the weld nugget has to pull out simultaneously from the top and the bottom base material. Practically, any unbalanced loading or imperfections in the test specimens will cause the nugget to pull out asymmetrically. Future investigation is needed.

Conclusions

Using trouser specimens with 8 mm leg width, the mode-III cohesive values for Al5754-O thin plates were first calibrated. The specific work of separation was determined to be 38 kJ/m^2 and the peak stress 280 MPa. The CZM was then applied to predict the crack growth in the trouser specimens with leg width 14 mm and 25 mm, and the cohesive peak stress was determined to be 250 MPa and 180 MPa, respectively, while the specific work of separation was kept a constant of 38 kJ/m^2. Finally, the lower-bound peak stresses for mode-I and mode-III (i.e., 285 MPa and 165 MPa) were used in the FE model with the CZM and the model successfully simulated the nugget pull-out for Al5754-O spot-weld. It is shown that the cohesive peak stress is geometry-dependent if the specific work of separation is a material constant.

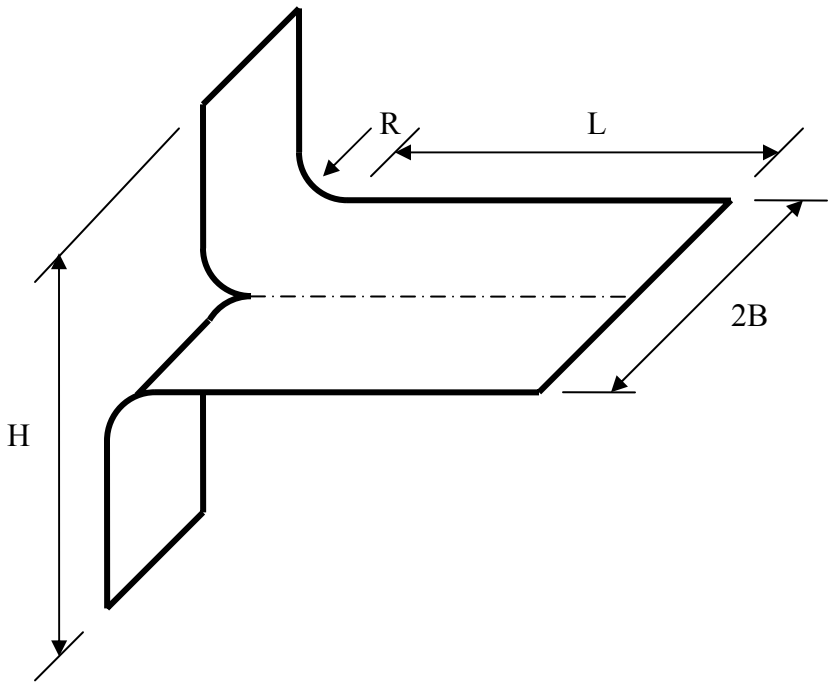

Figure 4.1 Sketch of two-leg trouser geometry.
The specimen thickness t = 2 mm.

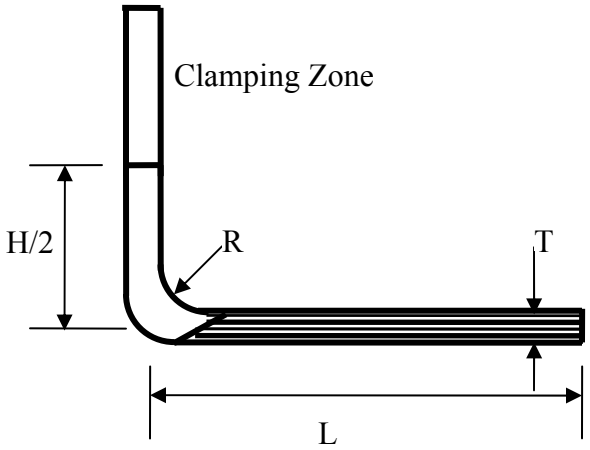

Figure 4.2 Section profile of two-leg trouser specimen.
The initial crack front was sawed to have a ramp.

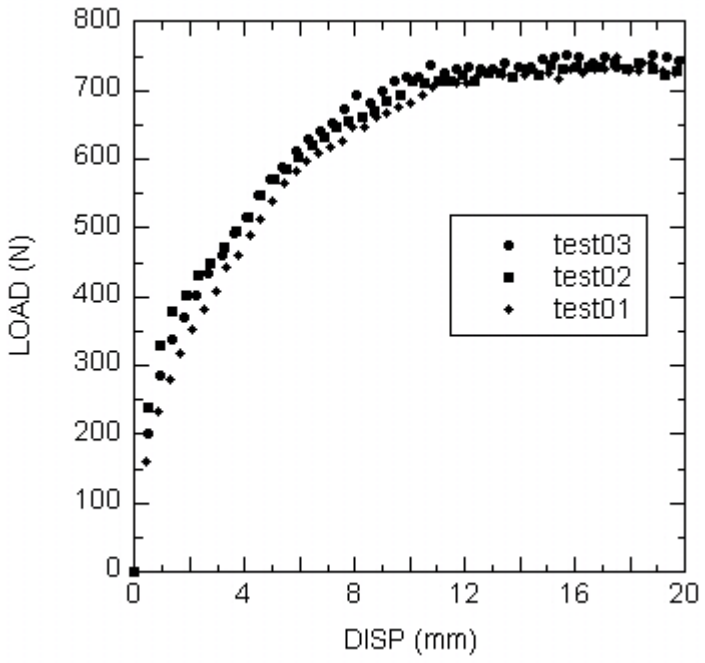

Figure 4.3 Experimental load-displacement curves for B = 8 mm trouser.

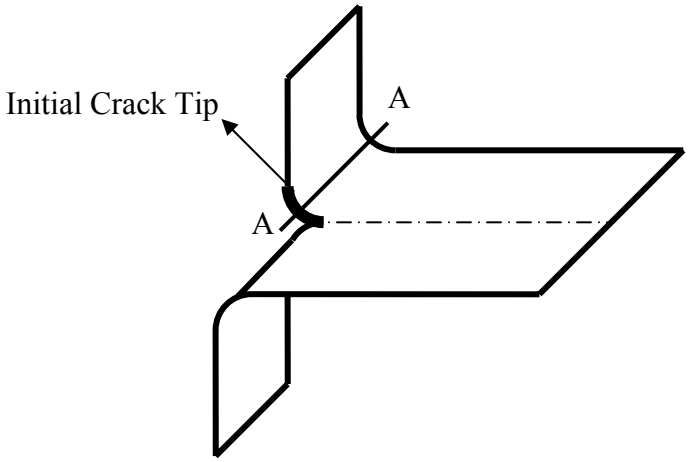

A-A section cut

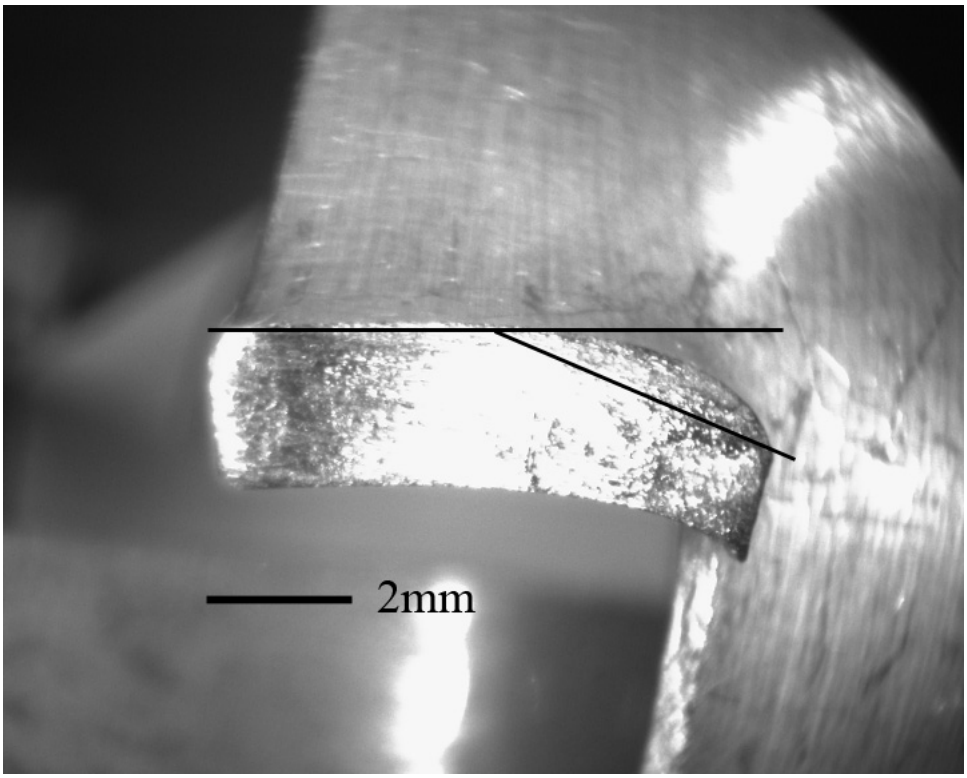

Figure 4.4 Shear zone size for B = 8 mm trouser.
Section A-A was cut after tearing has propagated through the section.

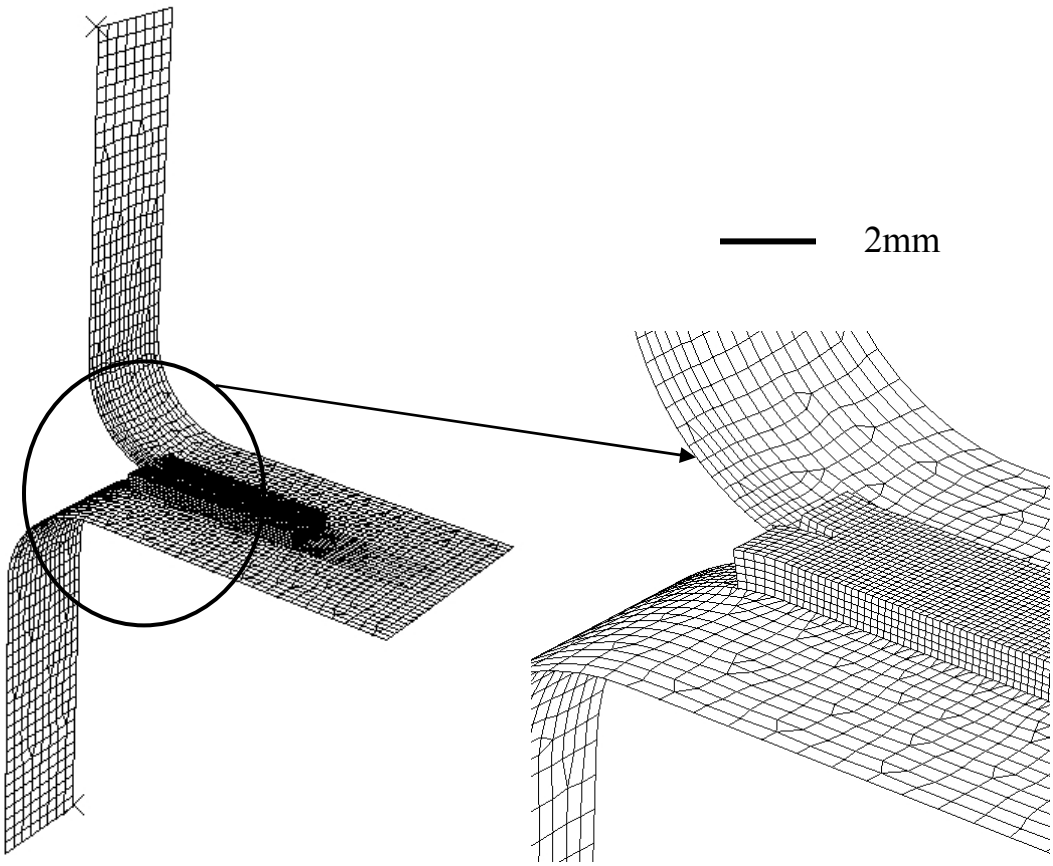

Figure 4.5 Coupled 2-D and 3-D mesh for B = 8 mm trouser specimen.

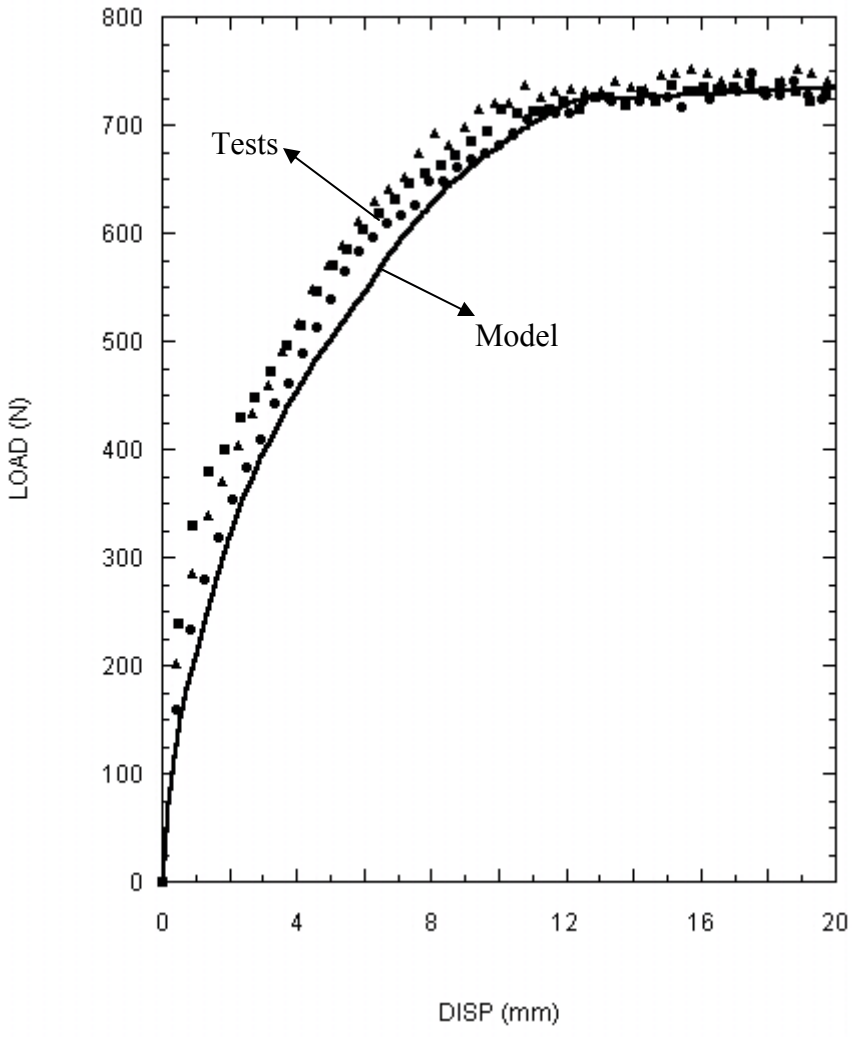

Figure 4.6 Load-displacement curves for B = 8 mm trouser: tests vs. model.

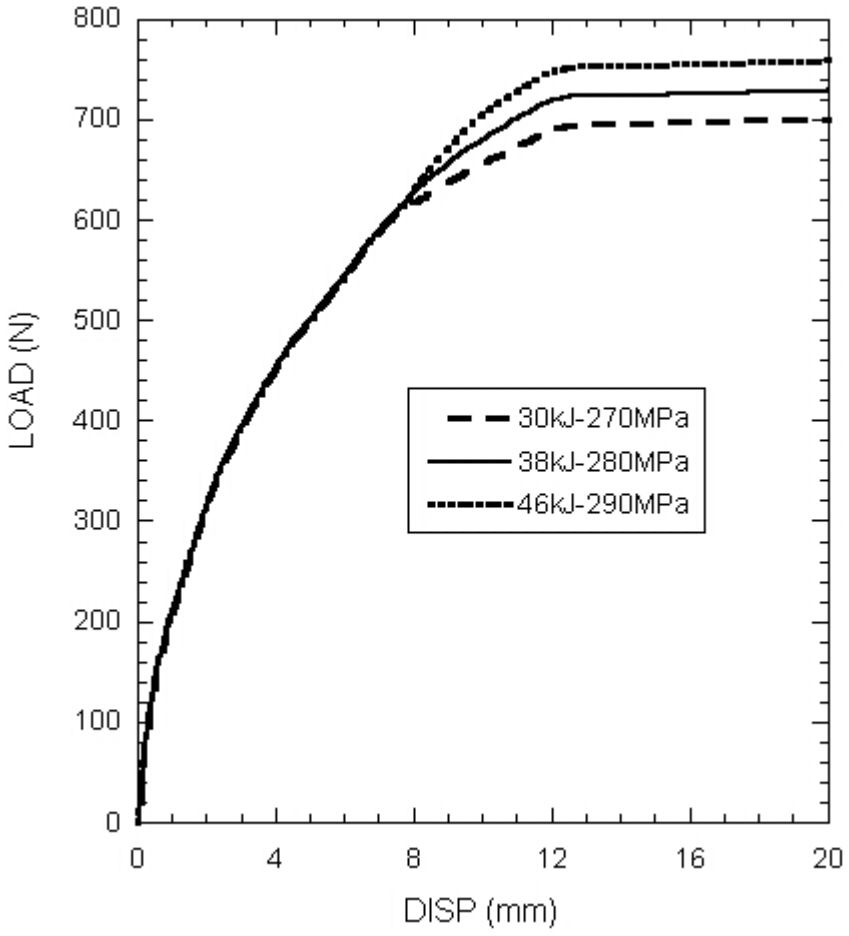

Figure 4.6b Load-displacement curves for B = 8 mm trouser. CZM predictions with different cohesive values of 30 kJ/m^2 with 270 MPa, 38 kJ/m^2 with 280 MPa and 46 kJ/m^2 with 290 MPa. The predicted load has an uncertainty of ± 4%.

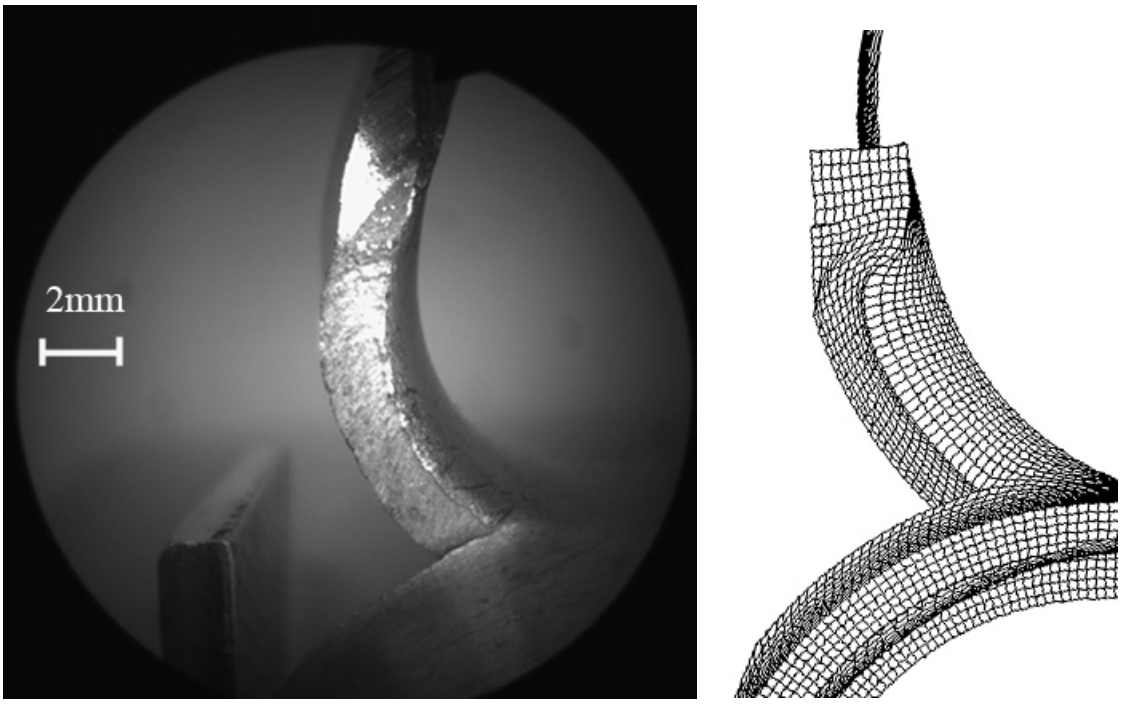

Figure 4.7 Tearing of trouser specimen: model vs. test.

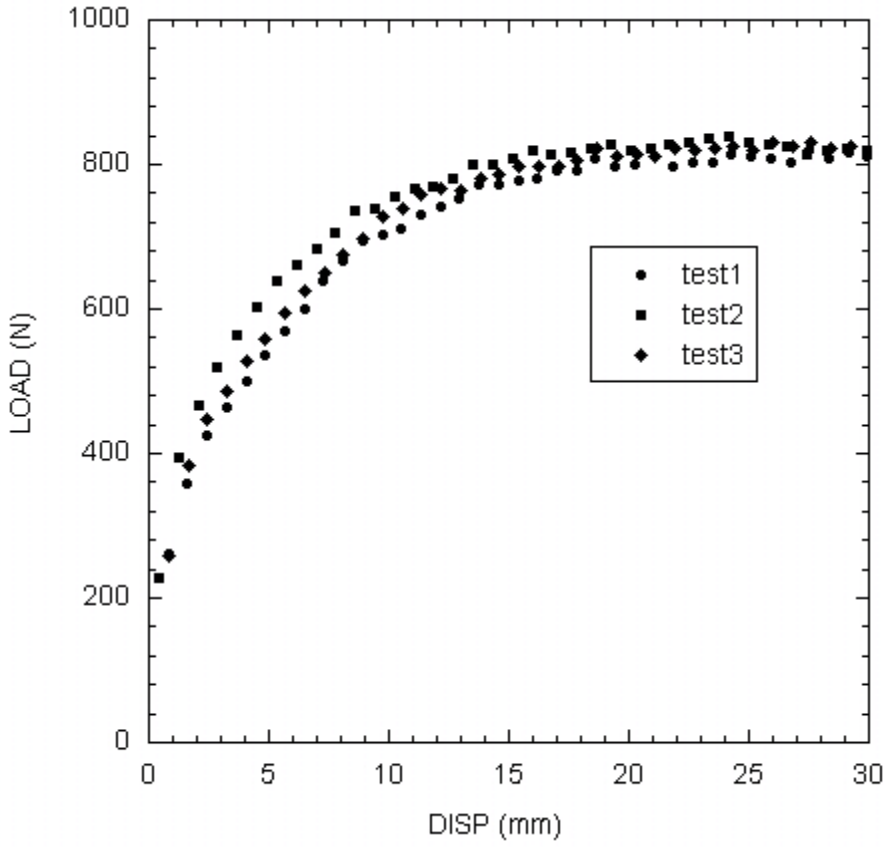

Figure 4.8 Experimental load-displacement curves for B = 14 mm trouser.

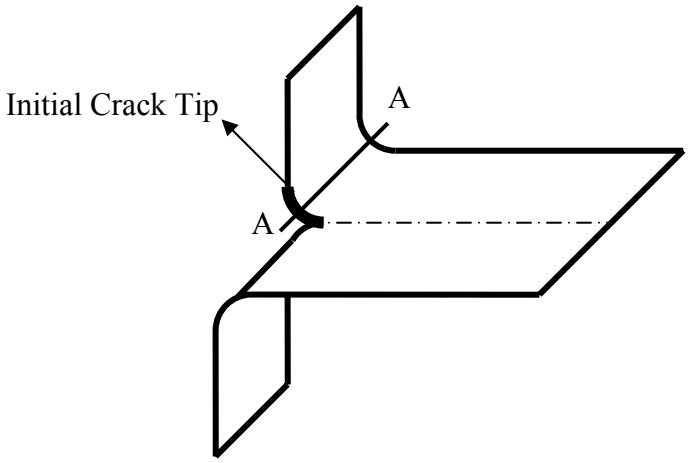

A-A section cut

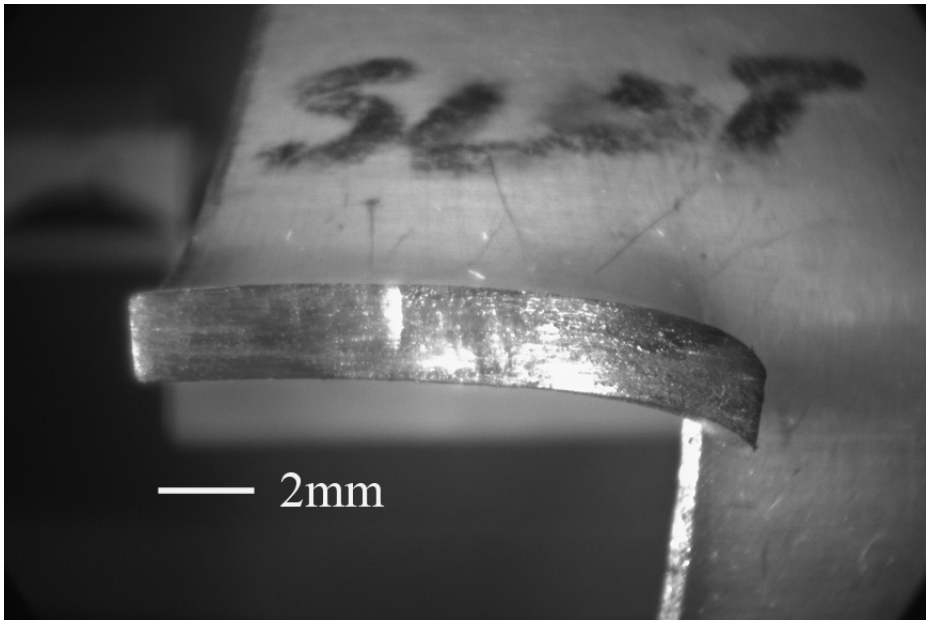

Figure 4.9 Shear zone size for B = 14 mm trouser.
Section A-A was cut after tearing has propagated through the section.

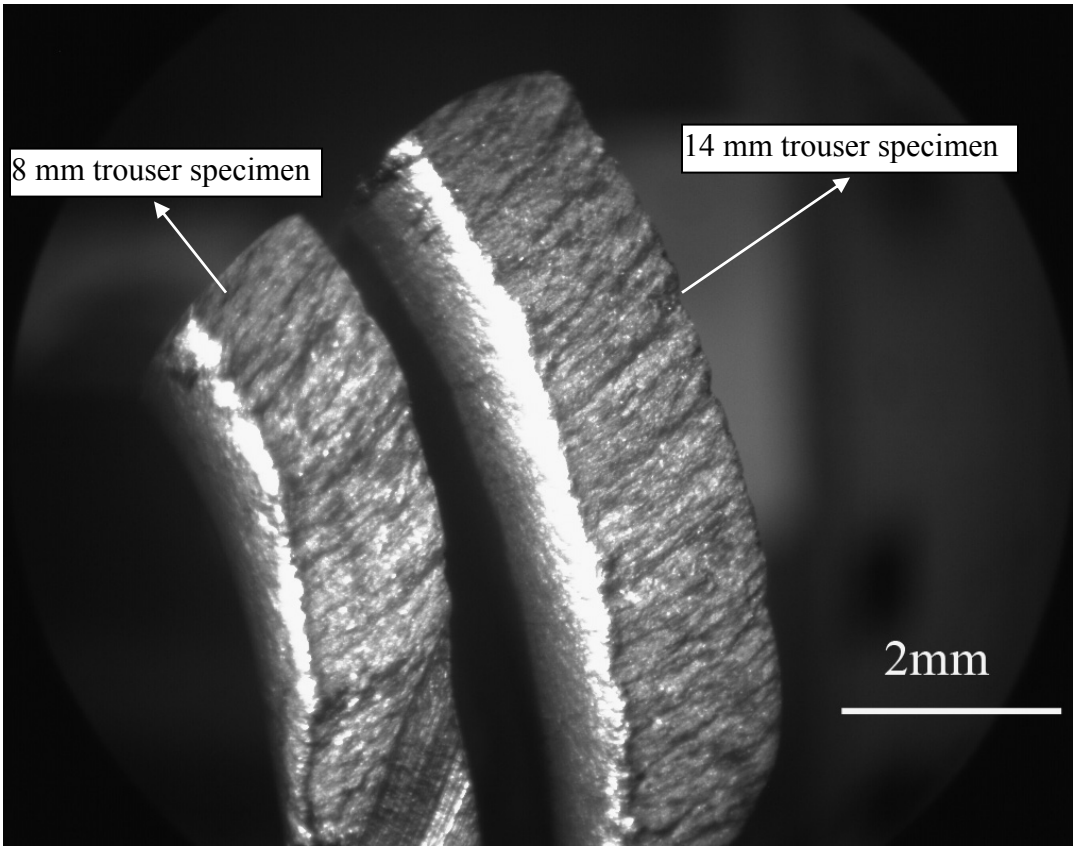

Figure 4.10 Fractured surfaces of trouser specimens at two different leg widths. The final thickness for the 8 mm trouser specimen was measured to be 1.3 mm. For 14 mm trouser specimen the necking is less and the final thickness is 1.5 mm. The initial material thickness is 2 mm for both specimens.

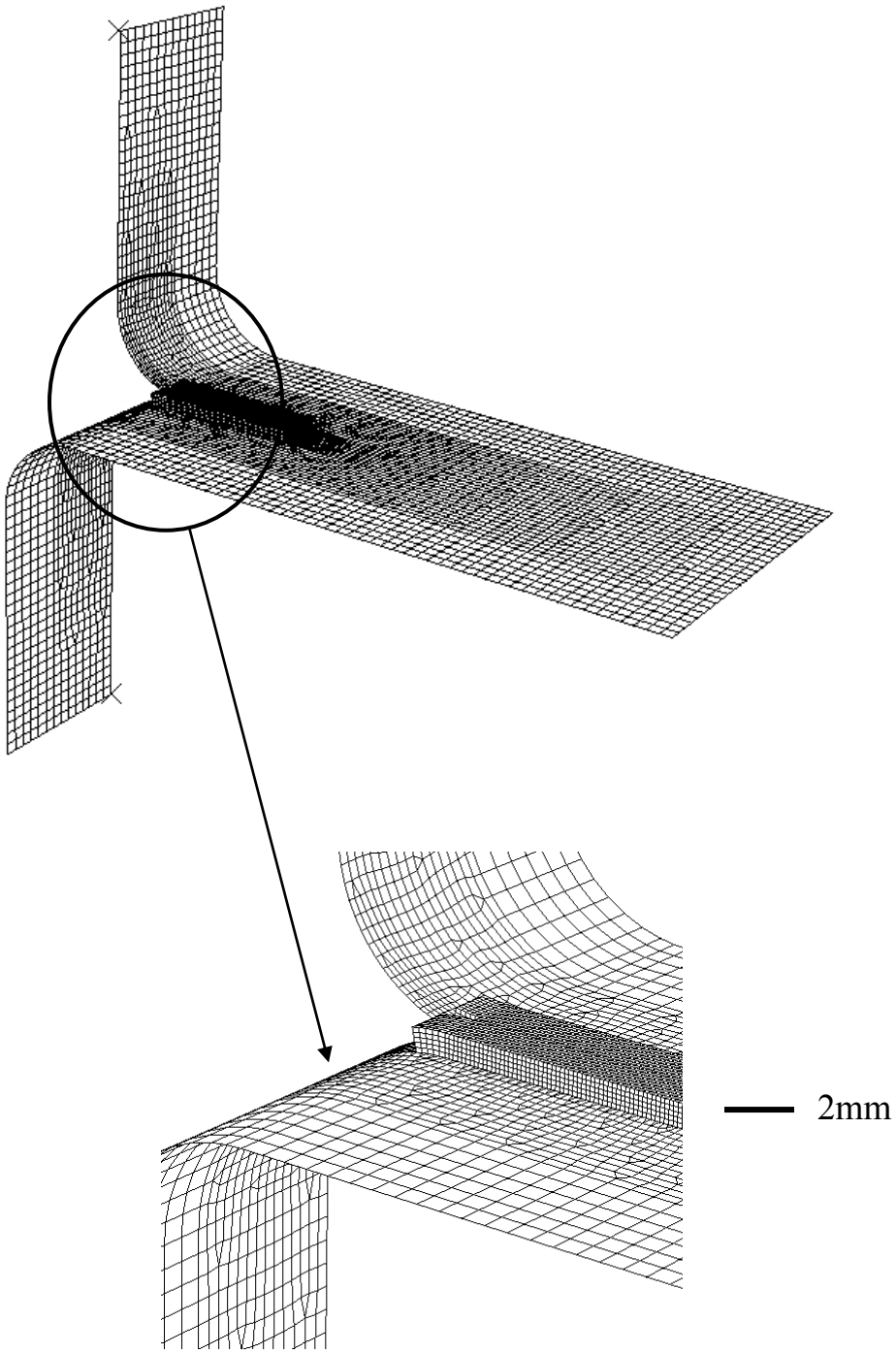

Figure 4.11 Coupled mesh for B = 14 mm trouser specimen.

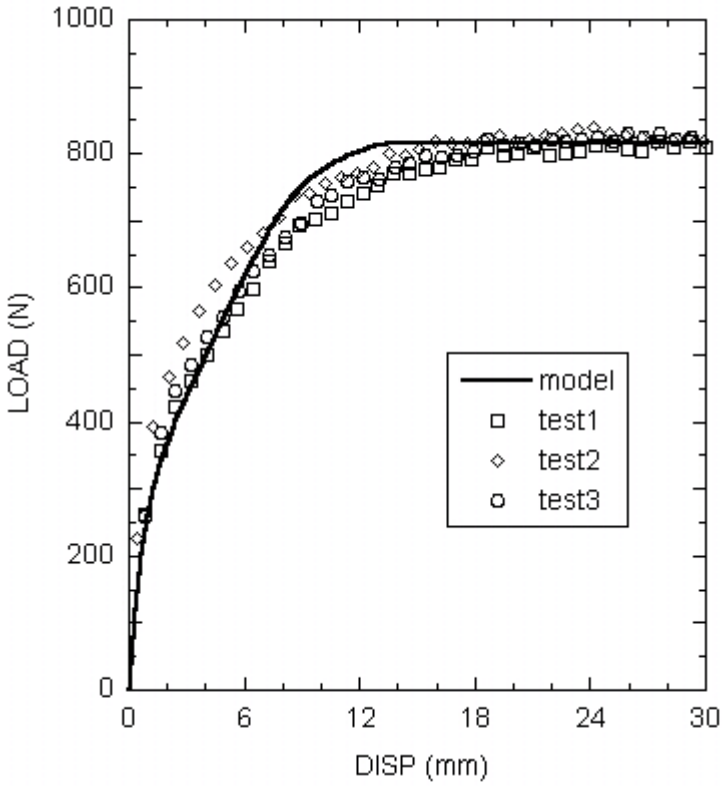

Figure 4.12 Load-displacement curves for B = 14 mm trouser: model vs. tests

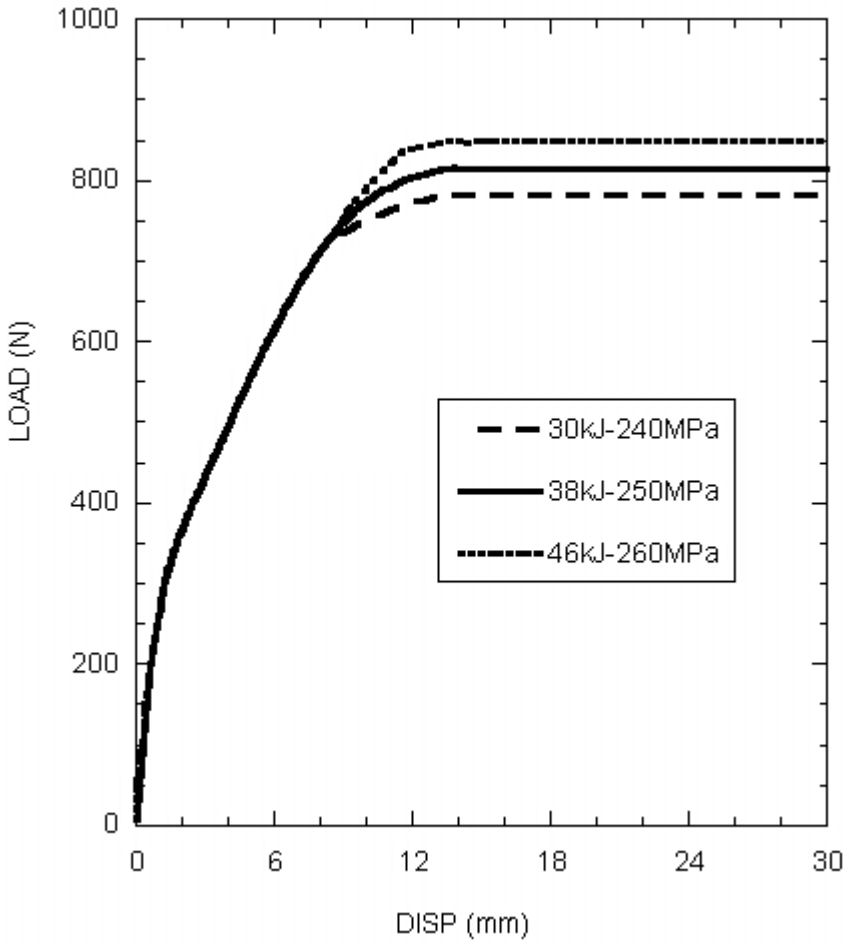

Figure 4.12b Load-displacement curves for B = 14 mm trouser. CZM predictions with different cohesive values of 30 kJ/m^2 with 240 MPa, 38 kJ/m^2 with 250 MPa and 46 kJ/m^2 with 260 MPa. The predicted load has an uncertainty of ± 4%.

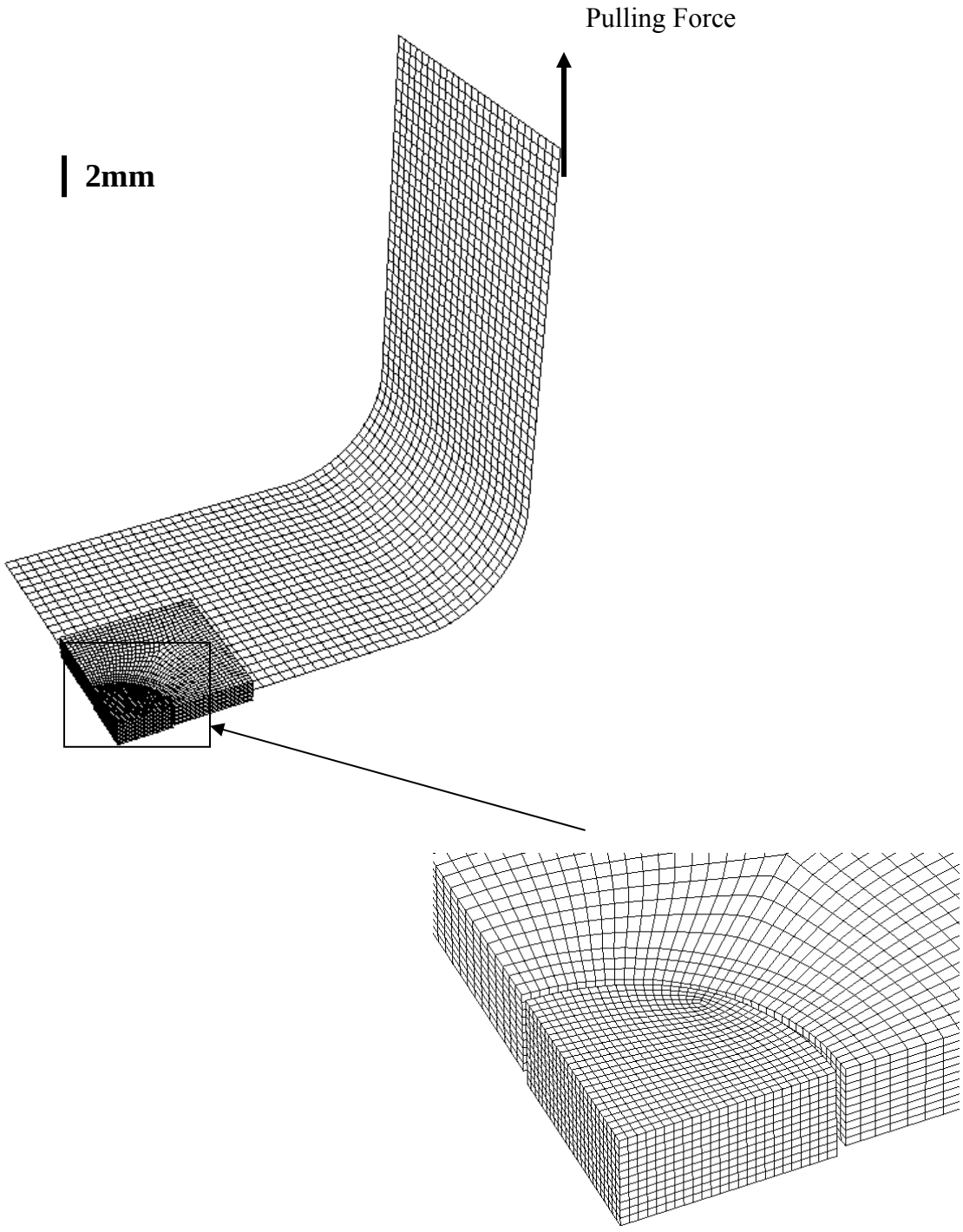

Figure 4.13 Coupled 2-D and 3-D mesh for nugget pull-out in a coach-peel specimen. Only one-eighth was modeled due to symmetry. The base material is 1 mm thick and the nugget diameter is 5 mm. The nugget pull-out is a mixed-mode fracture.

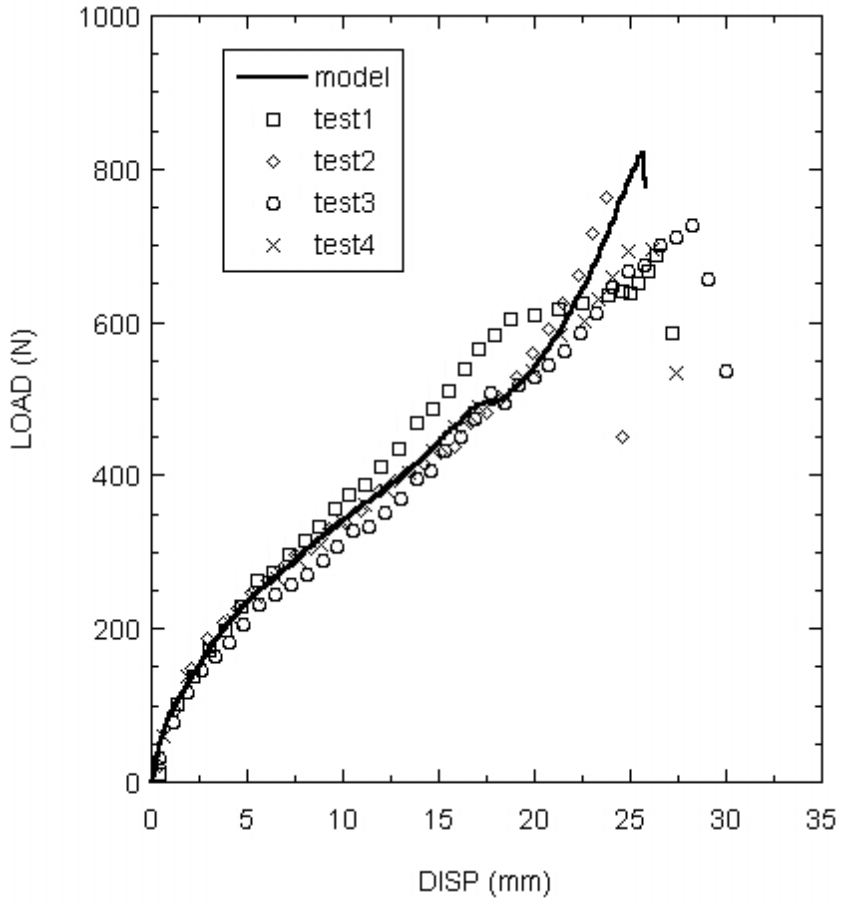

Figure 4.14 Load-displacement curves for nugget pull-out in coach-peel specimen. The model prediction is compared to tests. Test data are courtesy of M. N. Cavalli [12].

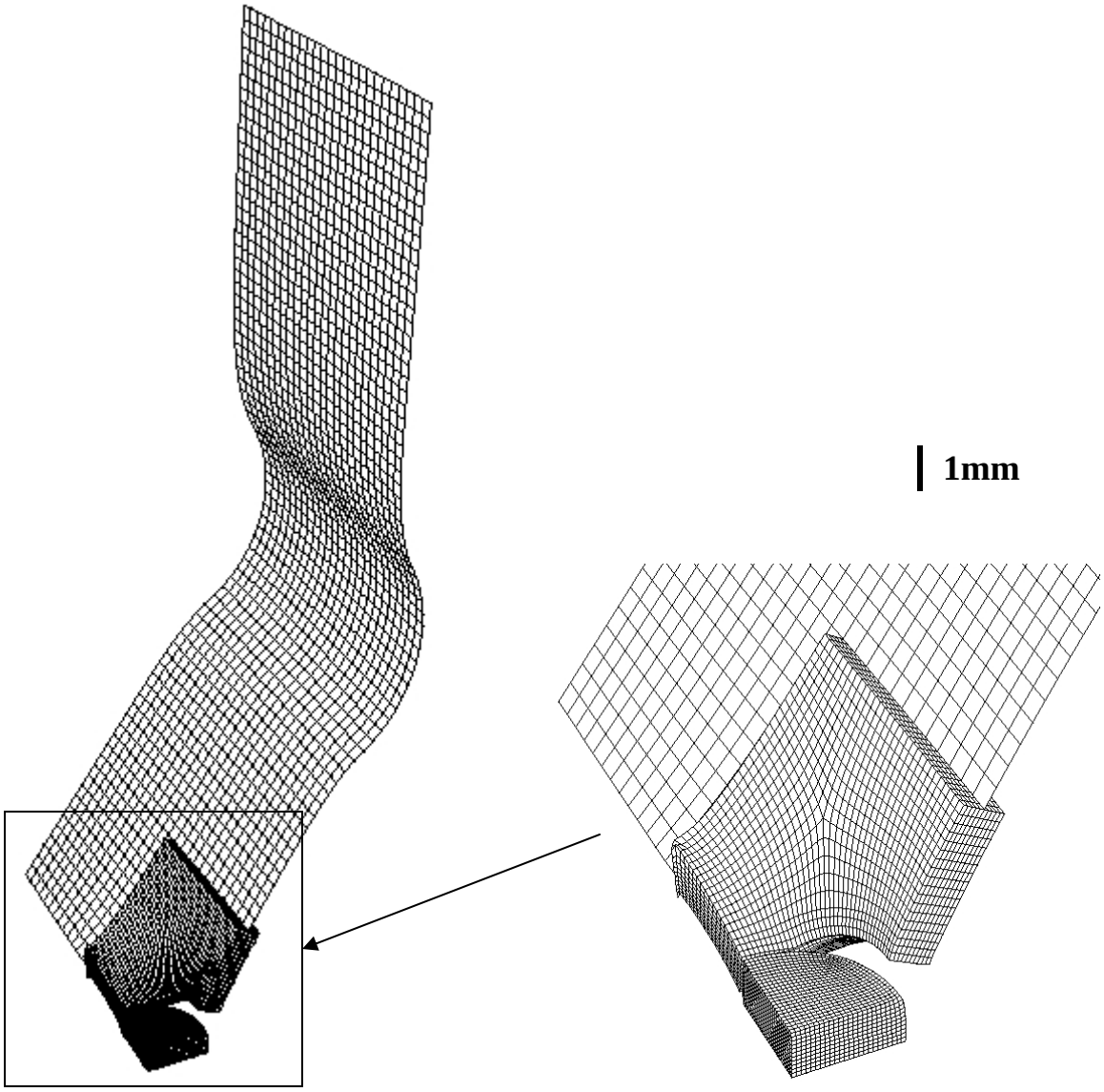

Figure 4.15 Deformed shape prior to final unstable fracture for nugget pull-out. The nugget pull-out is a mixed-mode of mode-I and mode-III.

References

1. R. S. Rivlin, A. G. Thomas, *Journal of Polymer Science*, **10**, 291-318 (1953).

2. A. F. Atkins, Y. W. Mai, *Elastic & Plastic Fracture – Metals, Polymers, Ceramics, Biological Materials*, Ellis Horwood Ltd., 1985.

3. Y. W. Mai, B. Cotterell, "The essential work of fracture for tearing of ductile metals", *International Journal of Fracture* , **24**, 229-236 (1984).

4. C. M. Muscat-Fenech, A. G. Atkins, "Elastoplastic trouser tear testing of sheet materials", *International Journal of Fracture*, **67**, 69-80 (1994).

5. G. I. Barenblatt, "Equilibrium cracks formed during brittle fracture", *Journal of Applied Mathematics and Mechanics*, **23**, 1273-1282 (1959).

6. D. S. Dugdale, "Yielding of steel sheets containing slits", *Journal of the Mechanics and Physics of Solids*, **8**, 100–104 (1960).

7. V. Tvergaard, J. W. Hutchinson, "The relation between crack growth resistance and fracture process parameters in elastic-plastic solids", *Journal of the Mechanics and Physics of Solids*, **40**, 1277-1397 (1992).

8. J. R. Davis, *ASM Specialty Handbook: Aluminum and Aluminum Alloys*, ASM International, Material Park, OH, 680 (1994).

9. J. M. Holt, H. Mindlin, C. Y. Ho, *Structural Alloys Handbook: Wrought Aluminum and Aluminum Alloys*, CINDAS/Purdue University, West Lafayette, IN, 14 (1994).

10. Z. H. Jin, C. T. Sun, "A comparison of cohesive zone modeling and classical fracture mechanics based on near tip stress filed", *International Journal of Solids and Structures*, **43**, 1047-1060 (2006).

11. N. E. Dowling, *Mechanical Behavior of Materials*, Second Edition, Prentice Hall, Upper Saddle River, NJ, 327 (1999).

12. M. N. Cavalli, *Cohesive Zone Modeling of Structural Joint Failure*, Ph.D.Thesis, University of Michigan, 2003.

Chapter 5

Summary and Future Work

The concept of cohesive zone model (CZM) underlines the fracture process and it is convenient to implement the CZM with two control parameters (the specific work of separation, defined as the work of separation per unit crack area, and the peak stress) into a FE code. Therefore, the CZM has been applied to simulate sheet metal fracture in this work. The stress–strain curve for Al5754-O has been obtained from tensile tests and the material is approximately isotropic based on experiments. Mode-I fracture has been examined for both Al5754-O (selected due to its insensitivity to heat treatment) and Al6082-O thin plates. The cohesive values have been calibrated and the geometry and thickness effects on the cohesive parameters have also been investigated. For Al5754-O, given the specific work of separation of 13 kJ/m^2, the cohesive peak stress has been calibrated as 600 MPa in this study using 2 mm Kahn specimens. For thin sheets under large-scale deformation, these values have been concluded to be geometry-insensitive, using single-notch specimens, and thickness-insensitive, using 1 mm, 1.6 mm and 2 mm Kahn specimens. The thickness-insensitivity of the cohesive parameters is also concluded from Al6082-O using 1 mm, 2 mm, 3 mm DENT specimens. Experimentally and analytically, the fracture toughness has also been shown to scale with material thickness due to the necking. However, for thick specimens or small-scale yielding where the necking is absent, the peak stress has been determined to be 285 MPa while the specific work of separation is kept a constant for Al5754-O. The lower-bound peak stress of 285 MPa (close to three times of the yield stress) is identified with the true stress at the onset of necking from tensile tests. And for a deep double-notch specimen, with a necking ratio (the ratio of final to initial thickness) of 0.6, the cohesive peak stress has been determined to be 450 MPa (four and half times of yield stress), compared to 600 MPa (six times of

the yield stress) for a necking ratio of 0.3 observed in Kahn specimens at small thickness.

Similarly, mode-III study of Al5754-O has been conducted. Using trouser specimens with 8 mm leg width, the specific work of separation has been estimated to be 38 kJ/m^2 and the peak stress calibrated to be 280 MPa. However, the cohesive peak stress has been shown to decrease with increase of the trouser leg width because the degree of plastic deformation determines the peak stress. The mode-III lower-bound peak stress has been determined to be 165 MPa from the mode-I lower-bound peak stress of 285 MPa, based on von-Mises theory. Finally, the mode-I properties (13 kJ/m^2 and 285 MPa) and the mode-III properties (38 kJ/m^2 and 165 MPa) have been applied to successfully simulate the mix-mode fracture of nugget pull-out for Al5754-O coach-peel spot-weld.

In summary, the original contributions of this work include the following:

While the CZM has been previously used to model ductile fracture of sheet metal, for the first time it is shown that the CZM is capable of simulating the necking during crack propagation in both mode-I and mode-III;

While the fracture toughness has been previously shown to scale with the material thickness in experiment or analysis, for the first time it is confirmed by the CZM in mode-I fracture of both Al5754-O and Al6082-O;

While the CZM has been previously applied to different fracture geometries, for the first time it is demonstrated that the calibrated cohesive parameters have good transferability for thin specimens when the degree of plastic deformation is similar in a mode-I fracture;

While the sheet metal fracture and the failure of spot-welds have been previously examined by many, it is the first attempt to study mode-I and mode-III fracture of sheet metal and then apply them to the failure of spot-welds;

While different procedures have been previously proposed to determine the two control parameters for CZM, for the first time it is shown that if the specific work of separation is assumed a material constant, the cohesive peak stress changes with the degree of plastic deformation and is therefore geometry-dependent.

One future work is to apply the developed method in vehicle crash simulation in automotive design. In a typical application, after the material properties are obtained using tensile tests, the true ultimate tensile stress can be used as the lower-bound peak stress and the specific work of separation has to be determined through common fracture tests. Also the future challenge is to theoretically predict the geometry effect on the peak stress. In addition, the presented approach may be extended to investigate the fracture of sheet metal under dynamic loading and the effects of the heat-affected zone may also be considered for spot welds in steel or other aluminum alloys.